2014

Bio-Compatible Materials for Advanced Energy Storage Devices Towards Biomedical Implantation

Sha Li
University of Wollongong

UNIVERSITY OF WOLLONGONG

Australian Research Council Centre of Excellence for Electromaterials Science

Institute for Superconducting & Electronic Materials (ISEM)

BIO-COMPATIBLE MATERIALS FOR ADVANCED ENERGY STORAGE DEVICES TOWARDS BIO-MEDICAL IMPLANTATION

Sha Li

This thesis is presented as part of the requirement for the

Award of the Degree of

Doctor of Philosophy

The University of Wollongong

March 2014

CERTIFICATE OF ORIGINALITY

I certify that this thesis is the result of my own work, expect where explicit reference is made to the work of others, and has not been submitted for another qualification to this or any other university.

I further certify that all material used to aid my research has been referenced in this thesis and, to the best of my knowledge, all work claimed as my own has not been previously published by any other person.

Sha Li

March, 2014

(Singed)……..

PUBLICATIONS

The following publications and manuscripts-under-review have been written during the course of this work:

1. **Li, S**., Sultana, I., Guo, Z., Wang, C., Wallace, G. G., & Liu, H. K. (2013), *Electrochimica Acta*, *95*, 212-217.
2. **Li, S.,** Guo, Z. P., Wang, C. Y., Wallace, G. G., & Liu, H. K. (2013). Journal of Materials Chemistry A, 1(45), 14300-14305.
3. **Li, S**., Zhao, C., Shu, K., Wang, C., Ping Guo, Z., Wallace, G. G., & Liu, H. (2014). Mechanically strong high performance layered polypyrrole nano fibre/graphene film for flexible solid state supercapacitor. *Carbon* (2014).
4. **Li, S**., Shu, K., Zhao, C., Wang, C., Guo, Z., Wallace, G. G., & Liu, H. K. (2014). One-step synthesis of graphene/polypyrrole nanofibre composites as cathode material for biocompatible zinc/polymer battery. *ACS Applied Materials & Interfaces* (2014).
5. Sultana, I., Rahman, M. M., **Li, S**., Wang, J., Wang, C., Wallace, G. G., & Liu, H. K. (2012).Electrochimica Acta, 60, 201-205.
6. Wang, H., **Li, S.**, Li, D., Chen, Z., Liu, H. K., & Guo, Z. (2014). TiO< sub> 2</sub> coated three-dimensional hierarchically ordered porous sulfur electrode for the lithium/sulfur rechargeable batteries. *Energy* (2014).

ABSTRACT

This PhD research project is dedicated in developing high performance, non-toxic electrode materials for energy storage devices that can provide power supply for the bio-medical implantable devices. This research direction is of high novelty and very challenging due to the lack of relative studies in the past. However, it is highly demanded by the rapid development of implantable bio-medical devices (IMDs). In chapter 1, a comprehensive review about the current research progress, trends, and challenges in the relevant fields is given.

The goal for this study is to give a systemic discussion on mechanism, optimizing solutions and propose the prospects of the energy devices for IMDs. This thesis contains four studies about various materials applied for both the bio-galvanic cells and solid state supercapacitors. These two types of energy devices has been prospected by authoritative researchers as promising power sources for IMDs.

Firstly, the electrochemical synthesis method was applied for preparing thin layers of *p*-toluenesulfonic acid sodium doped polypyrrole on the stainless steel mesh substrates. Three types of non-toxic aqueous electrolytes including 0.1M sodium chloride solution, Phosphate buffered saline (PBS) solution, simulated body fluids were used for constructing the zinc/aqueous electrolyte/polypyrrole batteries. The role of polypyrrole as the cathode material for such battery system is discussed based on the electrochemical studies and chemical characterization of polypyrrole before and after discharge.

To further improve the electrochemical property of the cathode material and therefore achieve better battery performances, in the following work, carbon nano tubes were chosen for incorporating with the polypyrrole. A three dimensional nano structure with polypyrrole coated on the carbon nanotube frameworks were produced with large specific surface area and high electric conductivity. Such composites were used as the cathode material for constructing the zinc battery with simulated body fluid as electrolyte. Detailed discussion about the effects of the coating amount of polypyrrole on the battery discharge performance was given to select the optimized cathode material. The battery testing was carried out in both the simulated body fluid with and without bovine serum albumin to test the feasibility of the battery for dry implantation.

In consideration of further improving the bio-compatibility of the cathode material, in chapter 5, reduced graphene oxide (RGO) was selected as the doping material to incorporate with the polypyrrole nano fibers. In addition, adding RGO nano sheets is also aimed to take full advantages of its various predominant properties including low charge carrier resistance and high specific surface area. The RGO/PPy fiber composite was synthesized via a simple one-step chemical polymerization method from the graphene oxide and pyrrole monomer mixture as precursor. Such composite was also utilized as the cathode material for the zinc/bio-fluids/polymer composite battery. The synergism effect of RGO was discussed based on the electrochemical testing data.

In the final work, we focused on developing the high performance flexible solid supercapacitors, which also has the prospects of powering the implantable bio-medical

devices. The free standing RGO/PPy paper was produced by vacuum filtration which is a simple and economy method. Flexible solid state capacitors were fabricated by the RGO/PPy paper electrodes and phosphate acid (H_3PO_4) infused polyvinyl alcohol (PVA) gel electrolyte. Such supercapacitor possess both good cycling stability and high specific capacitance. Its galvanostatic discharge specific capacitance is up to 345 F g^{-1}.

In the conclusion part, the recommendation about the future research directions and the elucidation of key issues is given which can be helpful for researchers who also have interest in the similar fields.

ACKNOWLEDGEMENTS

Completing a Ph.D. is definitely a vital event in my life, and I would not have been able to complete this long journey without the generous aids and supports from countless people over the past three years.

First of all I want to give my huge thanks to my supervisor prof. Hua Kun Liu, who takes care of me as her academic child throughout my 3.5 years PhD study. She is the most caring supervisor with great wisdom, from whom I learned a lot, not only about how to do research but also how to be a better person. I am extremely grateful to my co-supervisors Prof. Gordon.G.Wallace, Dr CaiYun Wang, and Prof. ZaiPing Guo for their generous help to my research work.

Thanks to the staffs of ISEM and ACEs, including Dr Darren Attard, Mr Tony Romeo, Dr Dong Qi Shi, Dr Patricia Hayes, Dr Zhixin Chen, Prof. ChongJun Zhao and Dr Yi Du for their kind help on my microscope and instrumental analysis work. I also want to give special thanks to my friend Mr Chen Zhao and Mr Kewei Shu for being good buddies and collaborators all the time.

I enjoy the time of studying at UOW with all my friends Ms Xuan Wen Gao, Ms Li Ya Feng, Ms Li Li, Ms YunXiao Wang, Mr HongQiang Wang, Mr RuiXiang Yu and Mr Chao Zhong ect. Thanks to all your guys for standing by my side.

I want to give the huge thanks to my parents. You are the most important people in my life who encouraged me not to give up at any time of my life. This is a tough research project, during which I personally encountered lots of frustrations, distractions and pressure. However, it is a great feeling that I can finally overcome all the negative things and accomplish my study proudly with all the support that I have been given.

Finally I would like to give my thanks to my family members here in Australia. I feel really lucky to have my husband Dr. Wei Li, who accompanies me all the time with ultimate understanding, support and Love. My uncle, aunt and cousin, you make me feel that family is always around me and you are also the motivation of my hard work to achieve better research outcomes. My two rabbits, Sheldon and Penny, thank for your two little creatures to sitting around me throughout the tough thesis writing time.

ABBREVIATIONS

IMDs	Implantable bio-medical devices
MFCs	Microbial fuel cells
EFCs	Enzymatic fuel cells
CPs	Conducing polymers
HER	Hydrogen evolution reaction
ORR	Oxygen reduction reaction
CNT	Carbon nano tubes
GO	Graphene oxide
RGO	Reduced graphene oxide
TC	Thionyl chloride
CF_x	carbon monofluoride
SVO	Silver vanadium oxide
PVP	Poly 2-vinyl pyridine
SBF	Simulated body fluid
PBS	Phosphate buffered saline
Py	Pyrrole

PPy	Polypyrrole
*p*TS	p-toluenesulfonate
PANi	Polyaniline
PT	Polythiophene
PEDOT	Poly(3,4-ethylenedioxythiophene)
PA	Polyacetylene
MO	Methyl orange
SBDS	Sodium dodecylbenzenesulfonate
HI	Hydriodic acid
BSA	Bovine serum albumin
Py	Pyrrole
DC	Direct current
EIS	Electrochemistry impedance spectroscopy
CV	Cyclic voltammetry
SEM	Scanning electron microscopy
TEM	Transmission electron microscope
EQCM	Electrochemistry Quartz crystal microbalance
AFM	Atom force microscope
S	Siemens

F	Faraday
mW	Miliwatt
g	Gram
mins	Minutes
hrs	Hours
M	Moles per litre
nm	Nanometre
V	Volts
A	ampere

Contents

Table of Figures

List of Tables

Chapter 1

Introduction

1.1 Overview of biomedical power sources

High performance energy devices including, batteries[1], capacitors[2, 3], fuel cells[4], and mico electromechanical energy devices (MEMS)[5] are demanded to be designed for all kinds of biomedical applications. These power sources can be classified into two types which are implantable power sources for internal usage and others for external devices. Implantable power sources are generally considered to be the more challenging research topic as there are many restrictive conditions needs to be applied for implantation. In this section, an overview of current power sources for biomedical devices will be given in terms of their applications.

Power sources designed for implantable medical devices (IMDs) are currently one of the most demanding research trends. Electrical energy is required to operate electrodes for “in-vivo” measurements, for biological growth control[6], for stimulating muscles[7] and nerves[8, 9], cardiac therapy, diagnosis and imaging devices[10], and internal drug delivery[11] *et al*. Morden methods in clinical diagnosis and therapy require electrical energy capable of generating relatively low current pulse over long period inside the human bodies. For achieving the power request of such bio-medical devices, several

commercialized battery systems have been well established for actual clinic applications which mainly include zinc air batteries for hearing aid devices and lithium battery for cardiac pacemaker[12-14]. The general power requirements of the major implantable medical devices are illustrated in table 1.1.

Table 1.1 power requirements of various types of implantable medical devices[15]

IMDs	Power Requirement
Cardiac pacemaker	30-100 mW
Cardiac defibrillator	30-100 mW
Neurological stimulator	30 mW to several mW
Drug pump	100mW to 2mW
Cochlear implants	10mW

Generally, the implantable power sources have to be of high levels of safety and reliability, or long service lives. Traditional implantable batteries mainly include the lithium batteries and metal-air batteries. Inevitably, both of the zinc-air and lithium batteries contain toxic chemicals which request absolute encapsulation and thus confined their shapes, size and flexibility. However, battery size and flexibility now becomes a key factor for designing the power sources for advanced micro sized implantable medical devices. To overcome the disadvantages of these traditional implantable batteries, current research works have been focused on inventing the power sources that are functionalised by the non-toxic electrochemical conversion reactions and utilizing the inherent chemicals from the human bodies as reactants[16, 17]. This type

of battery can be easily made into micro-sized monolithic structures with significant reduce in volume. Lately, a series of such battery has been developed which include the gastric fluid activated battery for endoscope[18], urine activated battery for clinical diagnosis[19] and the wearable sweat activated batteries[20]. This type of battery can be classified as "bio-galvanic cells" which can generate relatively low but stable and continuous energy outputs[17]. In this part, a comprehensive review will be given about both the conventional and well developed implantable power sources and implantable batteries that are still in prototype test period.

1.1.1 Lithium batteries

Primary Lithium batteries are the most universally applied power sources for various types of implantable bio-medical devices. Their preliminary applications are for cardiac pacemakers. The nickel-cadmium batteries were initially used as power sources for cardiac pacemakers and then replaced by zinc-mercury battery[14, 21]. The shelf lives of these two type of batteries are generally less than 2 years which induced the pacemaker replacement much more frequently than today[22]. It was until 1972, the invention of lithium iodine battery brought the real impact on prolonging the shelf life of cardiac pacemakers[23]. The life expectancy of lithium iodine batteries is up to 10 years. Nowadays, more than 50% of the market share of batteries for cardiac pacemakers is occupied by Li/I_2-PVP (Poly 2-vinyl pyridine). Meanwhile, there are several types of lithium batteries used for other types of implantable bio-medical devices[14]. Li/ Thionyl chloride and Li/CFx are generally applied for neuro stimulators and drug delivery

devices as these two types of devices have medium power requirements (in milliwatt range)[24-26]. Devices such as cardiac defibrillators need to be powered by batteries with even higher rate capability such as Li/Silver-vanadium-oxide and Li/MnO_2[27, 28]. The average gravimetric and volumetric capacities of implantable lithium batteries with various types of cathode materials are listed in table 1.2 below.

Table 1.2 Capacities of implantable lithium batteries with various cathode materials[24]

Cathode materials	Gravimetric Capacity	Volumetric Capacities
Iodine (I_2)	211	1041
Thionyl chloride (TC)	451	746
Carbon monofluoride (CF_x)	860	2322
Silver vanadium oxide (S-VO)	315	1521
MnO2	308	1540

Primary lithium batteries are selected for implantable bio-medical application mainly due to several predominate advantages. Firstly and most importantly, the lithium batteries all process high energy densities that can match the power specifications of almost all types of bio-medical devices. Second, the lithium batteries are kinetically stable with no gas emission, which ensured their safety for implantation. Third, lithium batteries have low self-discharge rate and consequently long shelf lives[29].

However, on the other side, the disadvantage of current commercialized lithium batteries is obvious. Most of these Lithium batteries contains toxic components and

thus have to be encapsulated by hard shells[30]. One of the most representative examples is the lithium battery for cardiac pacemaker. Fig 1.1 shows both the schematic diagram and digital photograph of a pacemaker. The battery occupies almost half of the device volume and generally weighted between 12.5 grams to 15.5 grams[14]. For micro-sized devices such as drug delivery devices or neuron stimulator, reducing the battery size is even more critical. Therefore, the real challenge of developing future lithium batteries for bio-medical applications is to further increase the energy density and simultaneously reduce their weight/volume.

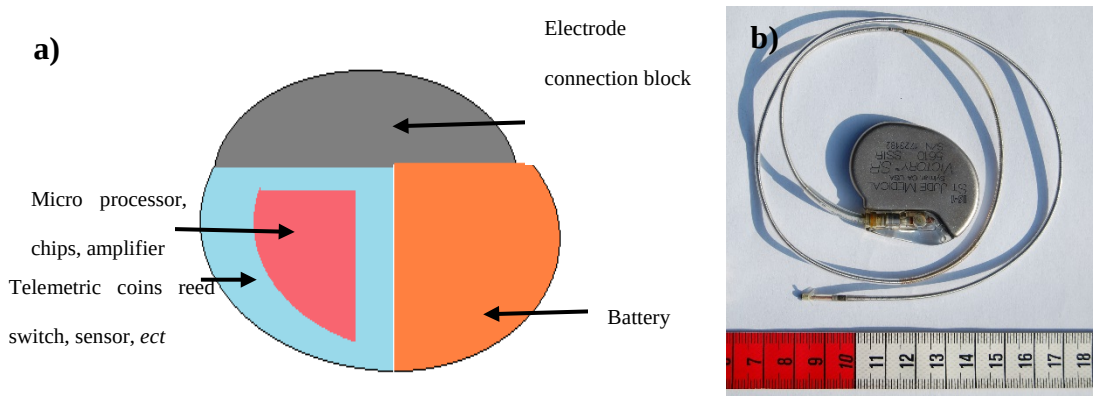

Figure 1.1 The schematic diagram (a) [14] and digital photograph (b)[31] of a cardiac pacemaker

Current research works mainly focus on two directions on developing next generation implantable lithium batteries, including inventing high performance electrode materials with large specific surface areas and designing flexible thin-film or solid state lithium batteries. Hybrid batteries such as Li/CF_x-SVO are also being investigated to create the

battery system possess both high energy density and high power density[32, 33]. Such battery system can provide large pulse current and simultaneously has longer shelf live.

Lithium battery has been the major research objects for powering the IMDs since 1970s, it is generally a type of battery acquiring energy from chemical conversion inside the battery. That is to say, the battery has no interaction with its working environments and it cannot utilize the biomass in vivo. Unlike lithium battery, there is a type of energy device that can generate electrical power from biomass or biofuel substrates, which are the bio fuel cells. In the following part, a brief introduction will be given about bio-fuel cells and their applications in the bio-medical field.

1.1.2 Bio-fuel cells

Bio-fuel cells can be defined as the systems capable of direct chemical to electrical energy conversion via biochemical pathways. The energy conversion is achieved by the electron flows generated by the redox reaction assisted by biocatalyst[34]. Traditionally, bio-fuel cells can be classified as two types according to the natural of biocatalyst. Systems using specific isolated enzymes for at least part of their operation are known as enzymatic fuel cells (EFCs), while those utilizing whole organisms are defined as microbial fuel cells (MFCs)[35, 36]. More recently, another type of bio-fuel cells are recently being recognized and under development which is biomimetic catalyzed fuel cells[37]. Some of the researchers still consider that biomimetic catalyzed fuel cells as a type of enzymatic fuel cells, expect that they use abiotic biomimetic catalyst to

accelerate the electron transfer process.

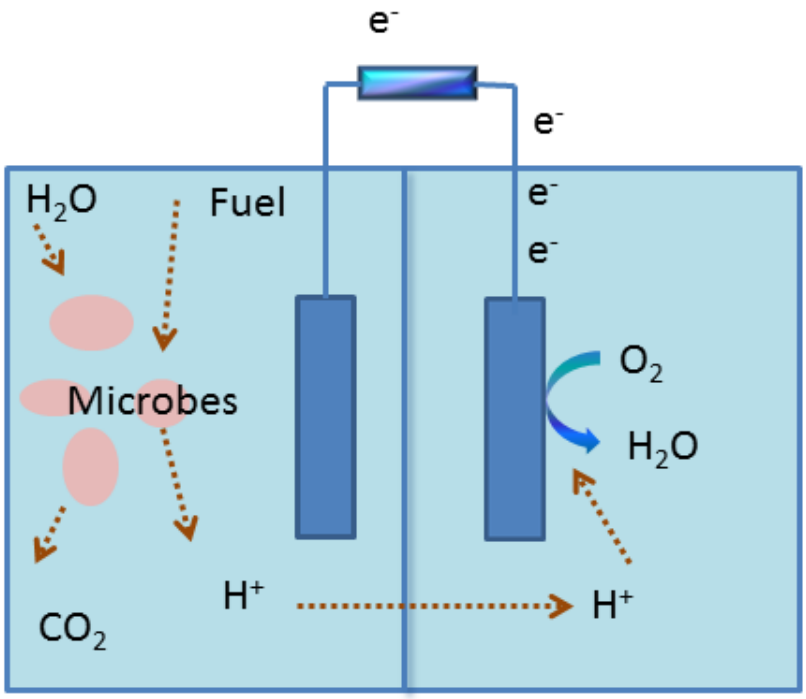

Figure 1.2 the schematic diagram of a microbial fuel cell[38]

MFCs generally use bacteria as catalysts to oxidize the organic or inorganic fuels such as Methanol and glucose. Currents can be produced by electron flows from oxidized substances to an insoluble acceptor (MFCs anode). It can be classified into two types, which are mediator and mediator-free microbial fuel cells[39]. The mediator-free cells generally use the electro-active metabolite to ferment the fuel substrate and therefore generate electrical flows[40]. The other type is the microbial fuel cells which use redox mediators to shuttle electrons via the metabolic pathways from the microorganism to the electrodes[41, 42]. A scheme shown in Fig 1.2 can explain its mechanism directly.

MFCs have operational and functional advantages over the technologies currently used for generating energy from organic matter. It can directly convert chemical energy to electricity with high conversion efficiency[38, 39, 43]. Meanwhile, it can be operated efficiently at ambient, and even at low, temperatures distinguishing them from all current bio-energy conversation processes[44]. MFCs do not need energy input for aeration when the cathode is passively aerated. However, MFCs are generally not considered as a suitable candidate for implantable power sources due to their evitable shortcomings including infective nature of most known micro-organisms and its low volumetric energy densities[45, 46].

Compare to microbial fuel cells, enzymatic bio-fuel cells (EFCs) are more profoundly studied as a substance for implantable power sources. This type of biological fuel cell offers a high bio-catalysis efficiency (compare to microbial fuel cells), the potential of miniaturisation or integration due to their simple construction[4, 35, 47, 48]. Enzymatic biofuel cells generally operated with the similar mechanism as other types of bio-fuel cells. What distinguish them from the other types are nature of the catalyst and the fuel they accept. Enzymatic fuel cells can be classified into two types according to the electron transfer mechanism, which are cells with medicated electron transfer process (MET) and cells with direct electron transfer process (DET). For MET, low molecular weight and highly redox active species are usually applied as the medications to shuttle electrons from enzyme active site and the electrodes, While the DET the electrons are transferred via a revisable enzyme catalysed redox reaction of the molecular substrates[49, 50]. Fig.1.3 is the schematic diagram showing the difference between these two mechanisms.

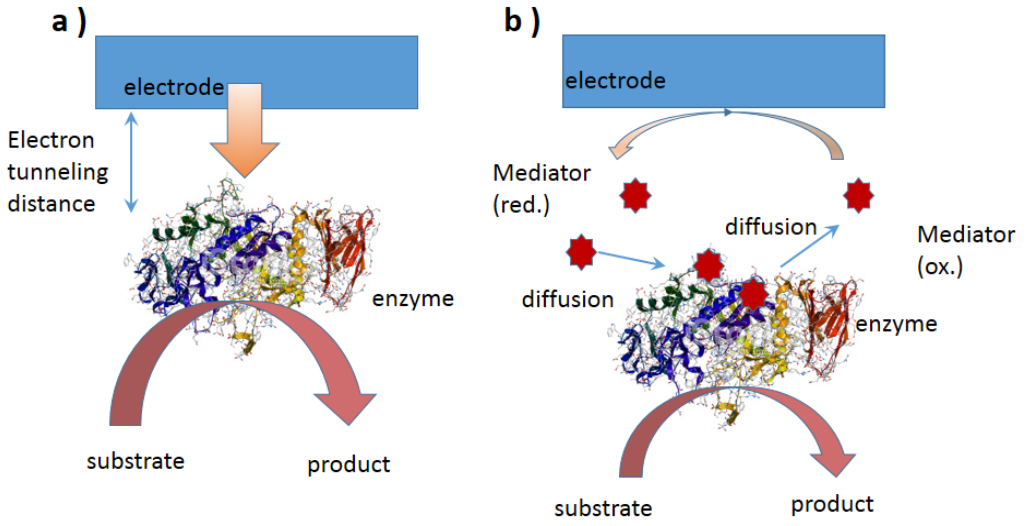

Figure 1.3 the schematic diagram of a microbial fuel cell with (a) direct electron transfer mechanism (b) mediated electron transfer mechanism (ox. Means the oxidised state, red. Means the reduced state)[4]

To date, the enzymatic fuel cells still have many disadvantages, including low power density and energy density (compare to the traditional fuel cells), low fuel utilization and short lifetime[35, 51]. The two key factors needs to be improved for enzymatic fuel cells are the catalytic rate and stability of the enzymes. Current research work put focus on generally two directions to improve the performance of an enzymatic bio-fuel cell. The first pathway is to increase the specific surface area of the electrodes, especially the anode, to support the mass transport of liquid fuel[52]. The second is to realize the immobilization of the enzymes and therefore enhance its catalytic efficiency[53, 54]. The other effort is to further optimize the anode material, including improving its electron

or proton conductivity without sacrificing the surface areas[55].

Innovations in developing enzymatic fuel cells for bio-medical application are ever going[56]. In Aug 2007, Sony™ announced the development of a "bio battery" that generates electricity from carbohydrates (sugar) utilizing enzymes as its catalyst. The cell applied the power generation principles found in living organisms which is a successful example of EFCs[57]. This battery is not targeted for implantable usage however it gives out an example that "bio-fuels" can be potentially used for power sources for real industry application.

1.1.3 "bio-galvanic" cells

The bio-galvanic cells usually contain the sacrificial anode and a cathode, and the anode will be used up during the course of electrochemical reactions. Thus, the theoretical life of a bio-galvanic cell is determined by the corrosion rate of the anode[17, 58]. The cathode usually plays a role as a catalyst which can motivate the reactions on the anode side. The reasons why such cells are called "bio-galvanic cells" are usually because the cell can be activated by the body fluids such as saliva, urine or blood plasma[59]. The term is proposed at late 60s in the last century[60].

The sizes of the battery are limited by the request of the medical devices. Above all, the materials for making such battery have to be bio-compatible and non-toxic for implantation. The design of such battery is another key factor to achieve the goal of

"in-vivo" implantation not only because the size limitation of the cell, also because it demands for the unique sealing methods. The research about inventing micro, non-toxic and implantable body fluid activated galvanic cells is quite challenging and by far there are not many successful examples. However, some researchers have achieved some inspiring results from which we can see through the bright future of this field. In the following part some of the examples will be illustrated in the following part.

1.1.3.1 Primary Metal battery with "bio-fluids" electrolyte

The configurations and working mechanism of a primary metal battery utilizing "bio-fluids" as electrolyte is relatively simple. It is simply a galvanic cell composed of two metallic electrodes with different electric potentials and usually separated by a porous membrane. Human fluids including urine and gastric fluids are generally electric conductive and contains various types of cations and anions, making them suitable for being electrolyte of various type of galvanic cells[61, 62]. There are a few examples belonging to this category that have been developed. Hikaru.J *et al* developed a micro battery system using gastric fluid as electrolyte for swallowable endoscope[18]. The battery composed of a Zinc anode and platinum as counter electrode. The actual mechanism of such battery is a zinc dissolution reaction in acidic environment and it was claimed by the author that the reaction had no obvious hydrogen release. Its maximum power outputs is 1.0mW at 0.42V undergoing an external load of 200 Ω. The author further tested the battery by using it as a power supply for a wireless telemetric device. The result showed that the battery was not only capable of transmitting data but

also driving a commercially available DC motor.

Another example is the urine activated paper battery designed by K.B.Lee for self-diagnosis device[63, 64]. The whole battery is simply a Mg-Cu battery with porous cellulose membrane as separator. The cellulose membrane was soaked by CuCl solution. The testing results showed that a maximum voltage of 1.47 V and a maximum power of 1.5 mW for the 1K Ω load resistor were achieved. The author claimed its possible application for home-based health test kit, for example, urine sugar test.

1.1.3.2 Metal-air "bio-galvanic" cells

Metal air batteries generate electricity through the redox reactions between the metal anode and oxygen. They are usually of the open cell structure to allow oxygen go through the cathode and consequently participate the electrochemical reactions. This feature makes them akin to a fuel cell, with the 'fuel' being a metal[65]. Metal air batteries have relatively high energy density than most types of the commercialized batteries as showed in Figure 1.4.

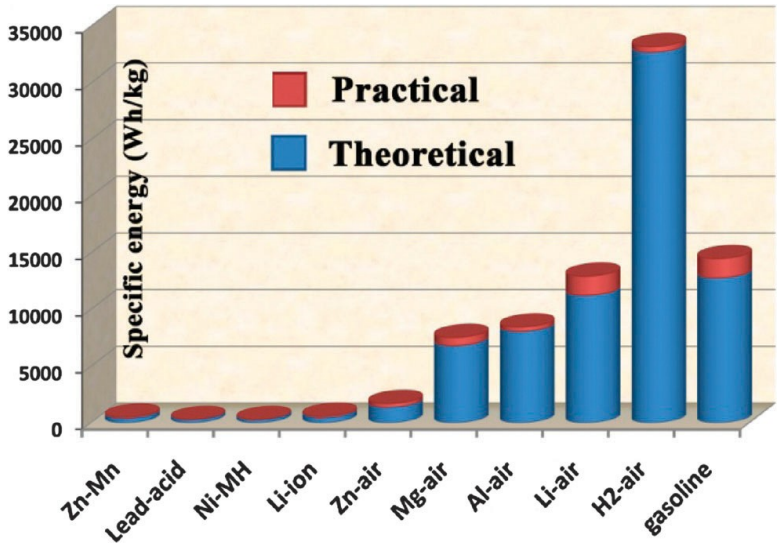

Figure 1.4 Comparison of the gravimetric energy density of some representative types of primary/rechargeable batteries, metal-air batteries, H_2-air fuel cell and gasoline[65].

The major applications of metal air batteries include zinc-air batteries for hearing aid device[66], the magnesium-air and aluminium-air[67] batteries for military usage (eg. underwater propulsion)[68]. Beside high energy density, metal-air batteries have many advantages including its environmental friendliness, high energy conversion efficiency, rapid start-up and shut-down, *etc*[69].

The prospects Zinc-air battery as power sources of implantable micro-medical devices have been proposed by Adam Heller early in 2006. The author pointed that a foreseen battery composed of zinc metal as well as the pH 7.3 physiological buffer electrolyte, are harmless enough to be considered for implantation[70]. The Magnesium is also a kind of bio-compatible metal that has been studied for various types of bio-engineering applications. However, the interface reaction of magnesium in neutral aqueous solution

(such as body fluids) is far more difficult to be controlled[71, 72]. This gives out more technical challenges for researchers focused on the magnesium-air bio galvanic cells.

The Metal-air bio galvanic cell is actually a derivate of mental-air battery. It generally contains a metal anode, the bio-compatible oxygen reduction catalyst, and the "bio-fluids" as electrolyte. Limited research work has been carried out about this type of cell, with most of the work focused on the Zinc-air or Magnesium-air system. In the following part, the mechanism, current research trends and technical challenges of these two battery systems will be reviewed.

1.1.3.2.1 Zinc-air system

Currently, the majority of modern hearing aids use zinc-air button cells as power supplies[73]. These batteries normally operated under 1.35 to 1.45 Volts. Typical battery life of commercialised Zinc-air battery for hearing aid devices runs between 1 to 14 days[74]. The working mechanism of such battery can be explained by the schematic diagram in Figure 1.5,

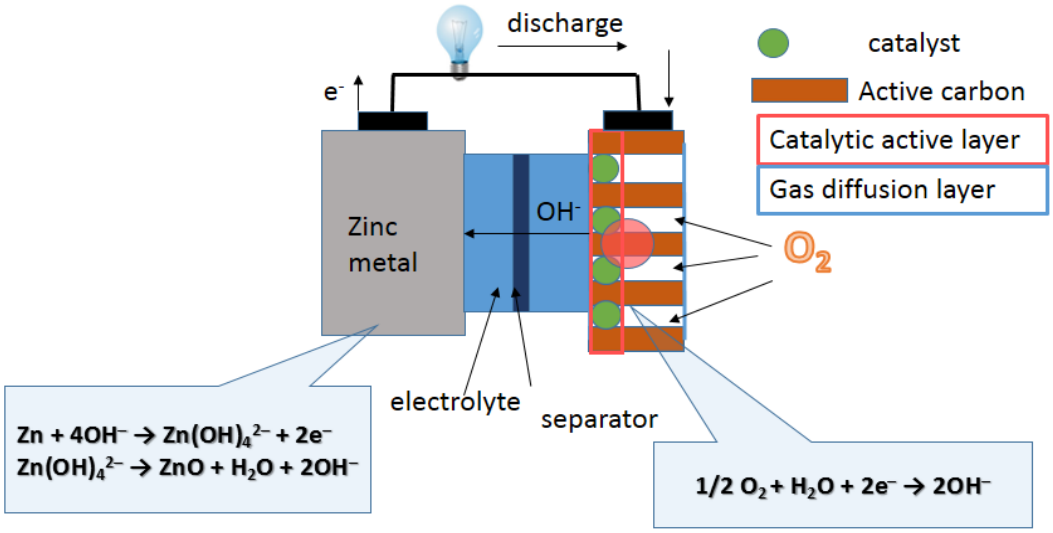

Figure 1.5 A schematic diagram of working principles of a typical zinc-air battery[75]

For the zinc-air battery system, the zinc particles form a porous anode, which is saturated with the electrolyte. Gas phase oxygen from the air reacts at the cathode and forms hydroxyl ions which migrate into the zinc paste and form zincate ($Zn(OH)_4^{2-}$), releasing electrons to travel to the cathode[76]. This is a three phase reaction, evolving gas phase, solid phase and liquid phase reactants. The zinc anode is simply the pure zinc metal with different morphologies, including zinc nano particles, zinc nano fibres or zinc dendrite[77]. Increase the zinc anode surface areas is the first issue needs to be addressed in order to improve the battery performance, since the larger surface areas can provide relatively large interface between the zinc particles and the liquid electrolyte[66, 78]. Zinc anode has the moderate dissolution rate in alkaline solutions; however, the hydrogen release reaction (HER) can occasionally occur on the zinc surface. Retard or eliminate the HER is necessary to achieve the complete energy

conversation of the “zinc fuel”[79, 80].

Compare to the research work about zinc anode, more efforts is putting on the research about oxygen catalyst on the cathode side. The oxygen reduction reaction (ORR) provides hydroxyl ions which are the key reactant for the liquid/solid interface reaction of the zinc anode. Therefore, the key issue of the air cathode side is to enhance the ORR efficiency[81]. The two pathways to improve the ORR include increase the oxygen gas flows and the catalyst efficiency. In a traditional Zinc-air alkaline battery there is always a porous structure existing in the cell to provide oxygen diffusion paths. This layer functions as a substrate for the catalyst as well. This layer in supposed to be thinned as possible without damaging the battery performance[81, 82]. Hence, the volume of the battery can be reduced. Zhu. et al developed a thin layer (<0.15nm) air electrode by placing carbon particles in a stinker locked network of metal fibres and suggested the thin layer air electrode is even more efficient than the traditional active carbon layer[83].

The mechanism of ORR for a zinc-air battery is complicated which involves multi-step electron-transfer resistance, and it can be sensitive to the genders of the catalyst. However, in the alkaline electrolyte the related cathode reactions can be briefly given as follows[84],

$$O_2 + 2H_2O + 4e^- \rightarrow 4OH^- \quad (E^0 = 0.40\ V) \tag{1.1}$$

$$O_2 + H_2O + 2e^- \rightarrow HO_2^- + OH^- \quad (E^0 = -0.07\ V) \tag{1.2}$$

$$HO_2^- + H_2O + 2e^- \rightarrow 3OH^- \quad (E0 = 0.87\ V) \tag{1.3}$$

$$2HO_2^- \rightarrow 2OH^- + O_2 \tag{1.4}$$

It is well documented that the ORR may proceed via either a four-electron pathway, in which the oxygen can be directly reduced to OH^- (1.1), or a 2 electron-pathway in which the oxygen is indirectly reduced to OH^- via HO_2^- (1.2-1.4). The two electron pathways are more common in the alkaline solutions and thus, the catalyst has to facilitate the decomposition of HO_2^-. In early stages studies about zinc-air batteries, noble metals such as platinum (Pt) or Pt-Ru were adopted as the ORR catalyst[82]. The fatal shortcoming of this type catalyst is their high cost. Significant progress has been achieved in recent years for less expensive yet efficient ORR catalysts[85, 86], such as perovskite (e.g$La_{1-x}Ca_xCoO_3$)[87, 88], spinels (e.g. Co_3O_4, $NiCo_2O_4$)[89] or carbon based complex materials[90] *etc*.

Designing a zinc-air battery with “bio-fluids” electrolyte proposed for dry implantation has some similarities to the traditional zinc-air alkaline battery since they share the similar working principle. There are few key factors needs to be improved just as the traditional zinc-air batteries including increasing the zinc surface area and enhancing the ORR catalyst efficiency. What distinguishes the Zinc-air “bio-galvanic” cell from a zinc-air alkaline cell is generally the working environment. The zinc-air alkaline cells are supposed to be exposed to air flows and the air diffusion layer is an essential component. The Zinc-air “bio galvanic” cells are targeted for dry implantation and the

main oxygen source comes from the blood oxygen or oxygen contained in other type of fluids. Hence, for a Zinc-air bio-galvanic cell, the porous air diffusion layer is not necessary, and the electrochemical reactions of the cell are two phase reactions which only involves liquid and solid phases. A schematic diagram showing the configuration of such cell is illustrated in Fig.1.6.

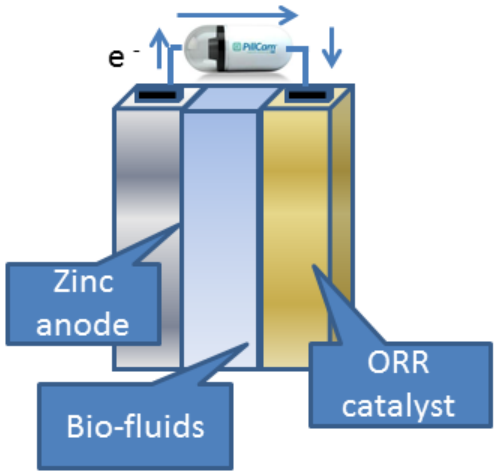

Figure 1.6 Configuration of a zinc-air bio galvanic cell

Besides, selection of the oxygen reduction catalysts should be of a different direction as the ORR catalysts for zinc-air alkaline batteries. First of all, since the battery is targeted for working in the ‘vivo” circumstance, the catalyst material should be completely bio-compatible and stable in the bio-fluids. Hence, most types of the ORR catalyst for zinc-alkaline batteries are not suitable. The ORR should be catalysed by a reversible redox reaction with high faradaic efficiency and excellent reversibility. Thus,

conductive polymers are obviously one of the most suitable candidates for the ORR catalyst of metal-air bio-galvanic cells. In previous work, some initial investigations have been carried out about the catalytic mechanism and effects on some conductive polymers such as polypyrrole and poly-aniline, which will be the main issue that will be reviewed and discussed in section 1.2.

1.1.3.2.2 Magnesium-air system

The magnesium-air system is less profoundly studied than the zinc-air system in the past mainly due to the difficulties in controlling its interfacial reactions[71, 72]. The working principles of a Mg-air battery can be explained by the equations below[84],

Anode,	$Mg \rightarrow Mg^{2+} + 2e^-$
Cathode	$O_2 + 2H_2O + 4e^- \rightarrow 4OH^-$
Total	$2Mg + O_2 + 2H_2O \rightarrow 2Mg(OH)_2$

The magnesium-air battery system has significant advantage including high theoretical energy density and high cell voltage. Its theoretical cell voltage (3.1V)[91] is comparable with Li-air battery (2.91V)[92] and its theoretical energy density (6.8 kW h Kg^{-1}) is much higher than the Zinc-air system (1.3 kW h Kg^{-1})[77]. Therefore, it is possible for Mg-air battery to be applied potentially for some bio-medical devices with higher energy requirement or current pulse requirement, such as cardiac defibrillator, neuron-simulator or even artificial organs in the future.

However, the technical issues of Mg-air system are obvious. Neither of its high theoretical cell voltage nor energy density can be achieved because of the high corrosion rate of the anode during discharge[93]. To improve the battery performance, the corrosion reaction of the Mg anode should be prohibited and the electrolyte needs to be stabilized. On the air cathode side, the ORR catalyst needs to be improved to prolong the battery life.

The magnesium corrosion is the main side reaction which usually accompanied by hydrogen release process (HER). The $Mg(OH)_2$ is only stable in the electrolyte with PH above 11[94]. In neutral and acidic solutions, the Mg anode will continuously and quickly be converted into Mg^{2+}. The dissolved Mg^{2+} can react with water through an electrochemical reaction, producing the magnesium hydroxide and hydrogen gas[95]. Such side reaction is absolutely undesirable for an implantable metal-air battery.

The major solutions to prohibit the HER include alloying the Mg anode and reformulation of the electrolyte. Alloying Mg with other elements with more positive standard potentials such as Al, Zn and Mn[96]. Currently, AZ31 (Mg-Zn)[97], AM50, AM60[98], MA8M06 (Mg-Al)[99] alloys are being investigated as anode materials for the Mg-air system. The alloying can prevent magnesium enriched phase from crack corrosion or pitting corrosion and therefore stabilise the interface reaction between the anode and aqueous electrolyte. To supress the HER, another effective way is adjusting the PH value of the electrolyte above 10[100]. According to recent research work, a saturated solution containing $MgCl_2$, LiCl or a mixture of the two is ideal to prohibit

the HER[101]. B. Winther-Jensen *et al* proved that a battery with mixed solutes of $MgCl_2$ and LiCl can maintain a stable cell voltage of 1.5V at the PH value of 11[72].

The potential of Mg-air using neutral bio-fluids as electrolyte is challenging. However, by choosing a proper Mg alloy, the corrosion rate can be decreased. Y.Kong *et al* tested a series of battery composed of AZ61 as anode material, polypyrrole as ORR catalyst and various types of electrolyte. The results showed that the batteries with neutral electrolytes including NaCl solution and PBS buffer solution all displayed very stable and high discharge plateaus (1.4V)[102].

Just as the Zinc-air system, for a Mg-air battery targeted for "in-vivo" implantations, conductive polymers are ideal choices for the ORR catalysts. The working principle of conductive polymers for catalysing the ORR is similar as that of the zinc-air system, as explained in section 1.2.1. Currently, researchers have tested PEDOT and polypyrrole, showing very promising performances.

1.1.3.3 Engineering of a "bio-galvanic" cell

The bio-galvanic cells are generally designed for 'in-vivo' implantation. Therefore, the design and fabricate a battery is as important as improving the discharge performances. There are a few key factors for designing an implantable "bio-galvanic" cell. First of all, the battery size and weight has to be strictly controlled. Second, the electrodes and encapsulation materials have to be bio-compatible. Third there should be pathways to

allow the bio-fluids permeate into the battery and therefore activate the battery[17, 37].

Many researchers considered to use the porous insulate membranes to make a paper like monolithic structure[103, 104]. Using a simple and cheap technology, the paper batteries (or cellulose-based devices) can potentially be applied for clinic diagnosis. Lee *et al* has developed human urine activated paper batteries as a power source to drive the on-board biosensors for healthcare screening of urine[64]. A.C. Baptista *et al* designed an ultrathin battery composed of a highly porous electro-spun cellulose acetate membrane with Al on one side and Ag on the other side[20]. Such design can allow the bio-fluids infiltrate into the battery more thoroughly and achieve better performance. Pushparaj and his research team demonstrated that electrode, separator, and electrolyte, can all be integrated into single contiguous nano-composite units to build blocks for a variety of thin mechanically flexible energy storage devices. The structure is very remarkable with cellulose fibre layer growing between electrodes. Such layer can work as the separator and absorb the "bio-fluid" through the cellulose matrix[105]. A research team of Uppsala University has made a flexible battery using two common ingredients: cellulose and salt, to power cheap medical diagnostics devices or sensors on packaging materials or embedded into fabric[103]. The work previously reported consists in the composite structures fabricated by laminating multiple stacks of individual layers. These are the most represented examples of making a paper like battery in which the separator and the electrodes are physically integrated into an ultrathin and flexible polymeric structure. Unlike biofuel cells, which need to deal with the instability of the enzymes, the structure of the ultrathin monolithic structure that can achieve good physical and chemical stability as a micro-power density energy source. In this way

thin and flexible batteries were developed envisaging their bio-medical applications.

Meanwhile, it is worth noting that most of the “bio-galvanic” cells are tested as open cells. Researchers like B. Winther-Jensen *et al* proposed that a metal-air bio galvanic cell should be encapsulated to prevent the emission of electrochemical reaction product[72]. However, by far, not much research work has been carried out about the encapsulation materials. The “skins” of an implantable bio-galvanic cell should satisfy two requirements. Firstly it has to be bio-compatible and secondly it has to be a water permeable membrane, which can transport the small sized ions and water and spontaneously prevent the leakage of precipitations inside the battery. This is one of the most challenging topics that need to be solved in the near future.

1.1.4 Supercapacitors and Battery/capacitor Hybrid structure

Supercapacitors are an energy device that obtained energy from paralleled movements of electrons via either an electrostatic absorption/desorption process or a faradic redox process and sometimes through the two pathways combined[106]. The supercapacitor has many advantages including high power density, stable cycling performance and low cost[107]. Fig 1.7 is a scheme showing the power density versus energy density for Fuel Cells, Batteries, capacitors and supercapacitors.

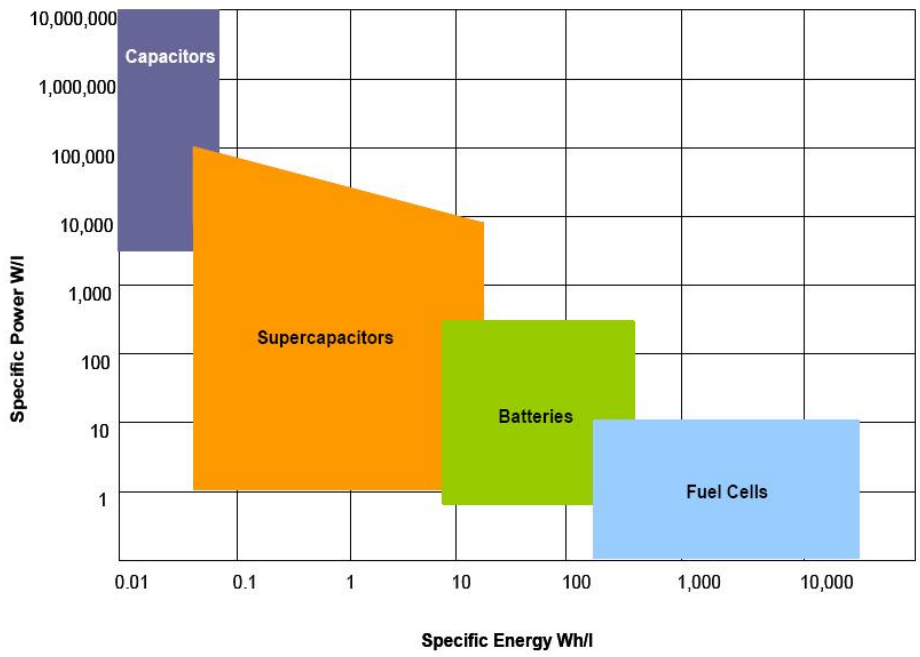

Figure 1.7 power densities versus energy density of fuel Cells, Batteries, capacitors and supercapacitors [108]

Clearly, when compared to batteries and fuel cells, supercapacitors generally possess lower energy density but higher power density. This feature decides that supercapacitors are suitable for certain types of biomedical devices such as implantable stimulators[109], pulse generator[110] or even wireless sensors[111].

Compared to the supercapacitors using aqueous electrolyte, solid states capacitors have obvious advantages of being applied as the power sources for the implantable micro-device[3]. The solid state capacitors are usually flexible and small sized which can easily be integrated into a micro devices. CZ. Meng *et al* used a solid state supercapacitor to power a micro implantable telemetric reading device. The author used a flexible paper-like polymer supercapacitors consisting of two slightly separated carbon nanotube

(CNT) paper/polyaniline (PANI) composite electrodes solidified in the gel H_2SO_4/polyvinyl alcohol (PVA) electrolyte. The capacitor has extremely high area capacitance of 1.3 mF mm^{-2} and excellent cycling stability showing less than 6 % capacitance loss after 10 000 charge/discharge cycles[112, 113]. The function of this high energy density supercapacitor was explained as providing resilience for the full system in the case of intermittent outages in radio frequency power by adding a short storage time.

Conventional sensors are mostly powered by a micro battery. However, the research work of Amit Pandey *et al* showed the prospects of the supercapacitor for powering a wireless bio-sensor. The author paralleled two commercial capacitors to increase the voltage rating and used a DC-DC converter to keep constant voltage outputs. This is an example showing how to engineer the supercapacitors as reliable power source for bio-medical devices[111].

The technical challenges of utilizing supercapacitors as implantable power sources are obvious. A single supercapacitor always display low cell voltage which cannot meet the requirements of most type of bio-medical devices. Therefore, paralleling is necessary for overcoming the problem, which means increasing the total volume of the power sources. Besides, the energy densities of present supercapacitors are still much lower than the batteries, which highly limited their application range.

The battery/supercapacitor hybrid structure combines the desirable characteristics of both the battery and the supercapacitor in a single integrated device of light weight and

extended energy capacity[114]. Currently, such power source is mainly investigated for powering the electric vehicles[115]. At the same time, some researchers also see its prospects for powering the implantable devices. Designing a high performance hybrid power sources for powering bio-medical devices have to be of the general characteristics as other types of power sources, which includes bio-compatibility, low toxicity, flexible, light weight and small sized.

1.2 Reviews on the materials for bio-compatible power sources

In the contents above, a comprehensive review about current research progress on power sources for bio-medical devices is given. In summary, designing such power sources is a complex multi-discipline project which may involves research work on bio-engineering, material science and electric engineering. In this PhD research project, our research group is dedicated to develop the high performance electrode material suitable for metal-air bio galvanic cells and solid state capacitors. Conductive polymers and carbon materials are chosen as the main research objects due to their bio-compatibility, high conductivity and activity for catalysing ORR. In the following part, a review will be given about the properties of these materials and their working principles as electrode materials for a “bio-battery” or supercapacitor.

1.2.1 Conductive polymers (CP)

The 2000 Nobel Prize in Chemistry was awarded to Alan J. Heeger, Alan MacDiarmid and Hideki Shirakawa for their extraordinary research work on highly conductive oxidized iodine-doped polyacetylene[116]. It was much earlier than that, in the late 60s, conductive polymers had already stepped into the central stage of material science research for widespread applications, including anti-corrosion layers[117], sensing devices[118], energy storage devices[119], actuators[120], non-liner optical devices[121, 122] *ect*. Unlike metal conductors naturally with free movements of electrons, conductive polymers obtain their conductivity through the movements of charge carriers along the overlapped and continuous orbital chains. The charge carriers are usually doped ions, which can be the electron acceptors (eg, K,Na) doped via a partial reduction process (*n-doping*) or the electron donors (eg. I_2, AsF_5) doped via a partial oxidation process (*p-doping*)[123]. The most well studied conductive polymers are mainly the conjugated polymers, including polyacetylene (PCA), polypyrrole (PPY), polythiophene (PTs), polyaniline (PANI) ect. The structures and conductivity ranges and structures of the most profoundly studied conjugated conductive polymers are showed in Table 1.3.

Table 1.3 Unit structure and conductivity range of some conjugated conductive polymers[124]

polymer	Structure	Conductivity (S cm^{-1})
Polyacetylene (PA)	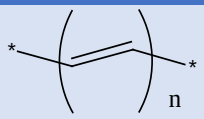	10^3 – 1.7×10^5
Polypyrrole （PPy）	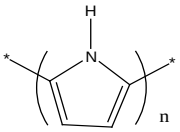	10^2 – 7.5×10^3
Polythiophene （PT）	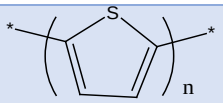	10 - 10^3
Polyphenylene and analogues	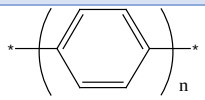	10^2 - 10^3
Poly(3,4-ethylene dioxythiophene) (PEDOT)	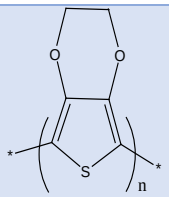	10^2 - 10^3
polyanniline	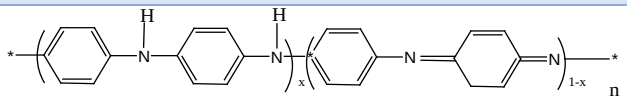	30 - 200

Among these conductive polymers listed above, polypyrrole (PPy), Poly(3,4-ethylene dioxythiophene) (PEDOT), polythiophene (PT) and polyanniline (PNAI) have been studied for bio-medical applications[125], including tissue engineering (PPy, PEDOT,PT,PNAI)， neural probes (PPy, PEDOT), biosensors and actuators (PPy,

PEDOT, PNAI) and drug delivery (PPy, PEDOT).

There are several universal properties of these conductive polymers which make them suitable for the bio-medical applications, which include bio-compatibility, good conductivity and ease of synthesis and modification. As for choosing the cathode material of a bio-galvanic cell, these properties are essential as well. In the bio-galvanic cell system, the cathode materials are expected to work as the ORR reduction catalyst. Therefore, the conductive polymers selected for cathode materials should be able to react with the dissolved oxygen effectively to produce continuous hydroxyl ions for the interface reaction of the metal anode. In 2005, V.G. Khomenko *el al* discussed the mechanism and feasibility of various types of conductive polymers as ORR catalyst in acid and neutral electrolyte[126]. The author proposed an "oxygen absorption" theory of the conductive polymers，indicating that the molecular oxygen can be absorbed by the carbon atoms on the polymer chain to form an "oxygen-conductive polymer" bridging complex and consequently be reduced. Figure 1.8 displays the "oxygen-conductive polymer" bridging complex showing the catalytic active sites of these polymers. These bridge complex structures are deduced based on the quantum-chemical calculations with complete optimization of the geometric bond parameters.

The author also concluded that the oxygen can interact only with conducting polymer in the reducing state and PEDOT showed no ORR catalytic activity. However, in later research work, it was proved that the modified PEDOT electrodes also have high ORR catalytic activity. In their work, Bjorn Winther-Jensen *et al.* claimed that the ORR

reduction process of PEDOT is a redox cycling process, which naturally rests in an oxidized form, is momentarily reduced by the action of the electrochemical cell[127].

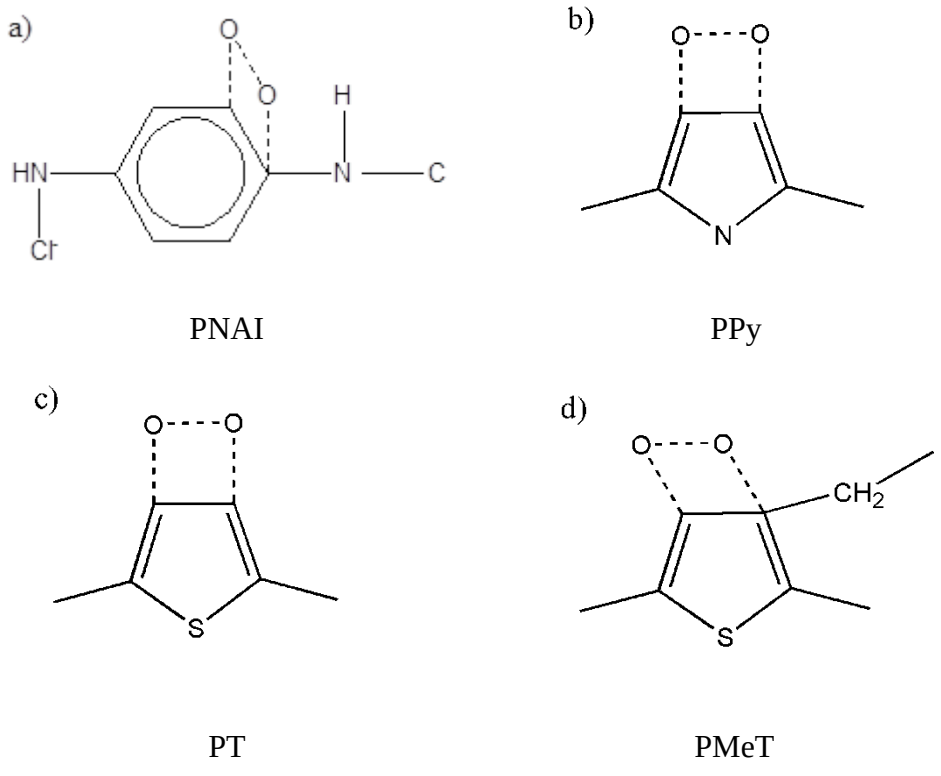

Figure 1.8 The "oxygen-conductive polymer" bridging complex formed during ORR[126]

The redox properties of PPy, PNAI, and PEDOT have been well studied in the past decade. It has been proved that the redox reactions of these conductive polymers are reversible. The study by V.G. Khomenko is valuable since it gave out the theoretical evidence than an "oxygen-conductive polymer" bridge complex can be produced during the ORR. However, the reaction mechanism is worth of further discussion. In this project, the author also discussed the mechanism of the conductive polymer as the

ORR catalyst, as explained in chapter 3.

Meanwhile, we also focused on the synthesis, modification and optimization of polypyrrole, in order to make it as an ideal electrode material for the zinc-air bio-galvanic cell as well as for solid state supercapacitors for possible bio-medical application. Polypyrrole has many interesting and unique properties when compared to other types of CPs. By choosing a proper dopant, the conductivity of PPy can be high up to 10^3 S cm^{-1} [128]. It is bio-compatible and also very stable in neutral and acidic aqueous solution[129]. Besides, polypyrrole can be easily synthesized in various type of nano structures, including nanotubes[130], nano fibres[131], nano particle[132] and even dendritic structures[133]. These nano–structured polypyrrole usually has high specific surface areas, which makes them even more favourable as the ORR catalyst or as the electrode material for supercapacitors. In the following part, a more detailed review on the electrochemical properties, synthesis and modification as well as applications of polypyrrole is given.

1.2.1.1 Synthesis of polypyrrole

The synthesis of polypyrrole has been profoundly studied using various methods, including (1) electro-polymerization at a conductive substrate (electrode) (2) chemical polymerization in solution by the use of a chemical oxidant (3) photo-chemically initiated polymerization and (4) enzyme-catalysed polymerization. However, the latter two methods are less developed due to technical challenges and the property limitation

of the resulting products.

For chemical polymerization, the monomers, dopants and oxidants are essential. The oxidants used for chemical polymerization mainly includes $(NH_4)_2S_2O_8$, H_2O_2 and many kinds of salts containing transition metal ions, such as, Fe^{3+}, Cu^{2+}, Cr^{6+}, Ce^{4+}, Ru^{3+} and Mn^{7+}[134]. Selecting the proper dopants is one of the main research directions to achieve higher electric conductivities or unique redox properties. The most frequently used dopants mainly include sulfonate groups and small anions such as Cl^- and NO_3^-. To improve the conductivity and specific surface areas of the resulting polymer, anionic surfactant are also added in the vast majority of cases. The intact molecules of the surfactant can be thickly absorbed on the PPY surface during the polymerization process which may act as the steric stabilizer. The presence of such steric stabilizer engenders the decrease in particle size and conductivity of PPY, as Aldissi et al. mentioned[135].

Chemical polymerization has the predominant advantage in controlling the morphologies of polypyrrole. Various types of nanostructured polypyrrole including nanofibers, nanotubes, and their well aligned membranes can be synthesised either using the soft-templates or hard templates. The soft templates usually refer to the organic surfactant or large sized organic molecular that can create the inorganic/organic mesostructures[136, 137]. The monomers can either be absorbed on the surfaces of these mesostuctures to produce the nanotubes or be encapsulated inside to produce the nanofibers. For example, by using $(NH_4)_2S_2O_8$ as the oxidant and hexadecyltrimethylammonium bromide (CTAB) as the ‘template’, fiber or ribbon like

structures can be obtained[136]. The PPy nanotubes can be synthesized by using Sodium 4-[(4-dimethylamino)phenyldiazenyl] benzenesulfonate (MO) as the 'template', which can form the nano rods in acidic solutions to absorb the pyrrole monomers[138].

There are many hard templates that can be applied for synthesizing nanostructured polypyrrole, such as particle track-etched polymeric membranes (PTMs)[139] and porous alumina membranes[140, 141], containing randomly distributed cylindrical pores with uniform diameters. These hard templates can be incorporated with polypyrrole to form the composite for various types of applications. Meanwhile, hard templates are also applicable for electrochemical polymerization. The hard template synthesis is carried out by introducing the monomer into the pores of the template and subsequent chemical or electrochemical polymerization of monomer. Because of the template confinement, the size and shape of the obtained product should theoretically reflect the size and shape of the pores or channels of the template[142]. Unlike the soft-templates which can be easily washed off after polymerization, most type of hard templates has to be removed by strong alkaline or acid solution that might cause the de-doping of the polymer[137, 142]. However, the shape of the resulting polymers tends to be more uniform.

Electrochemical polymerization is another major routine to synthesize polypyrrole. The electrochemical polymerization mechanism is a debatable subject as there have been a number of mechanisms proposed to date. However, what can be assured is that the reactive radical ion intermediates has to be formed during the polymerization process. The most well accepted mechanism is the Diaz's mechanism proposed in late 90s, which can be demonstrated by the schemes showed in Fig 1.9[143]

Electrochemical polymerization is capable of producing thin and flexible polypyrrole films. This technique can be applied for anti-corrosion treatment of metallic materials as well as surface coating for other conductive substrates. Since pyrrole has low oxidation potential, its electrochemical polymerization can be carried out in both the aqueous environment and organic solvent such as ionic liquid[144] or acetonitrile[145]. The solvent must minimize the nucleophilic reactions. Aprotic solvents appear to be the best for polypyrrole preparation. The protic acid, such as *p*-toluenesulfonic acid has to be added when using dimethylformamide or dimethylsulfoxide as the solvents[146]. In aqueous solution, high salt concentrations are necessary to give the polymer with the desired mechanical and conducting properties[145]. Beside the solvents and electrolyte, many other factors can affect the polymerization results, including the PH environment of the solution[147], temperature[148] and conductive substrates[149]. Different structural forms with different electrical and redox properties have been observed in PPy films depending mainly on the acidity of the polymerization medium and temperature. Therefore, control of electrochemical polymerization conditions is a complex but intriguing research object which can lead to the discovery of new high performance polypyrrole.

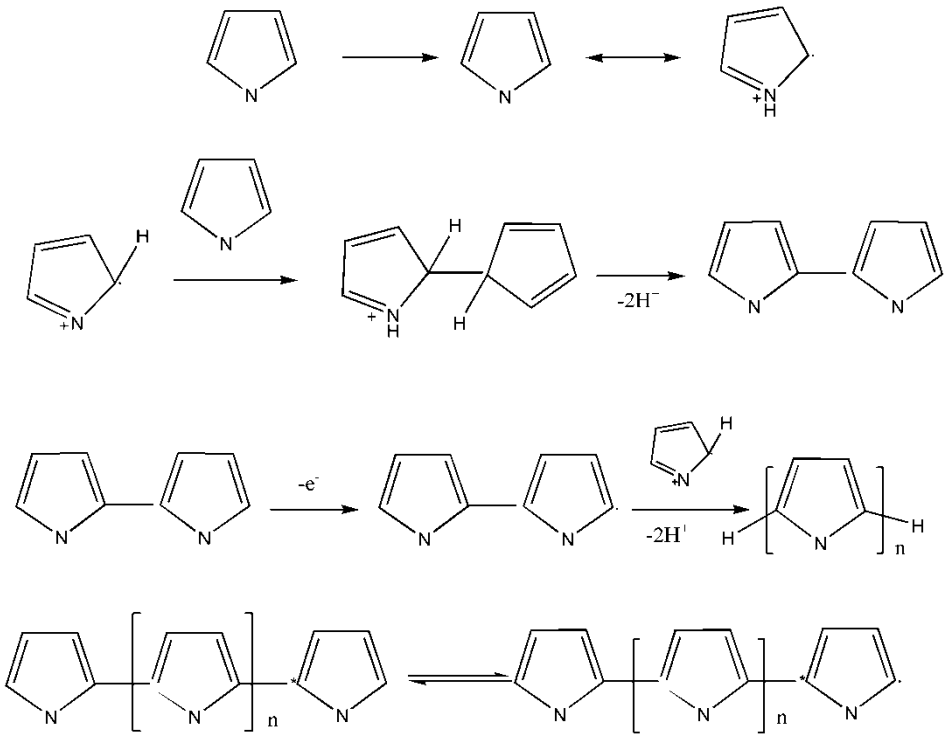

Figure 1.9 Mechanism for electrochemical polymerization of polypyrrole.

1.2.1.2 Properties and applications of polypyrrole

Polypyrrole possess many valuable properties such as electro-conductivity, bio-compatibility, redox activity and environmental stability. These properties are indispensable for the electrode materials targeted for implantable bio-medical energy or sensing devices[125, 150]. The conduction band and valence band gaps of conjugated polymers are narrower than the insulators and their conductivity is obtained via change of the band structures when being doped[124]. The doping can add charge carriers to the polymer and the charge carriers can either taking the electrons from the valence band

(*p*-doing) or adding electrons to the conduction band (*n*-doping). Polypyrrole generally belongs to the *p*-doing type CPs.

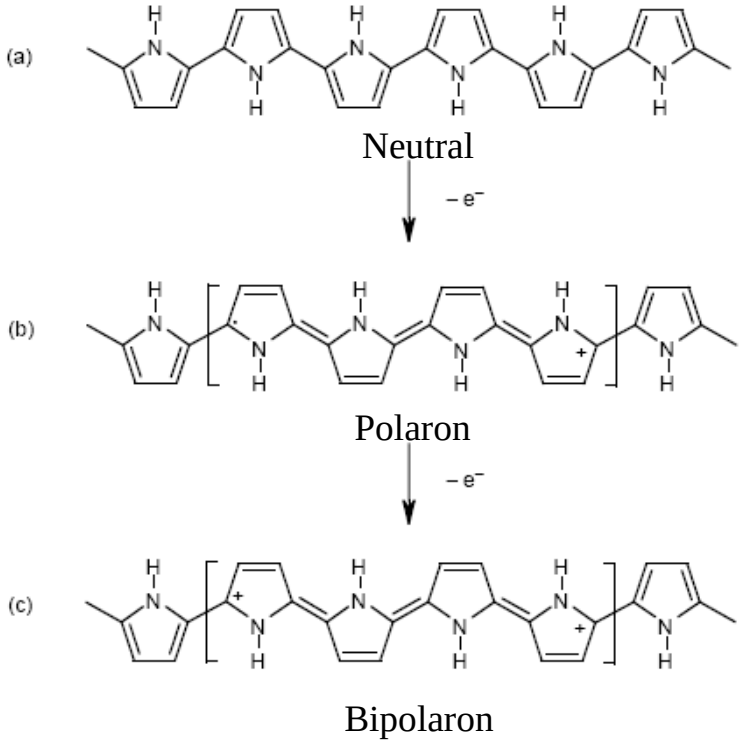

Figure 1.10 Electronic structures of (a) neutral PPy, (b) polaron in partially doped PPy[151]and (c) bipolaron in fully doped PPy

The doping mechanism and its effect on the conductivity of polypyrrole have been well studied. Like other types of CPs, polypyrrole also has two doping states, which are the polaron state and the bipolaron state as showed in Fig 1.10. The polaron state is defined as an intermediate doping state with one electron transferred to the bottom of the conduction band or being added to the top of the valence band. The bipolaron state refers to the complete doping achieved by the dimerization of two polarons[151, 152]. The

band structure revolution of PPy upon doping levels is illustrated in Fig 1.11. The band gap energy of polypyrrole can be narrowed to 1.4ev when 100% doped with two new bipolaron bands formed in the gap, as showed in Fig 1.10 (d)[153, 154]. The bipolaron doped state represents high oxidation level of the polypyrrole. In fact, the polaron state and bipolaron state are coexisting in the majority of doped polypyrrole.

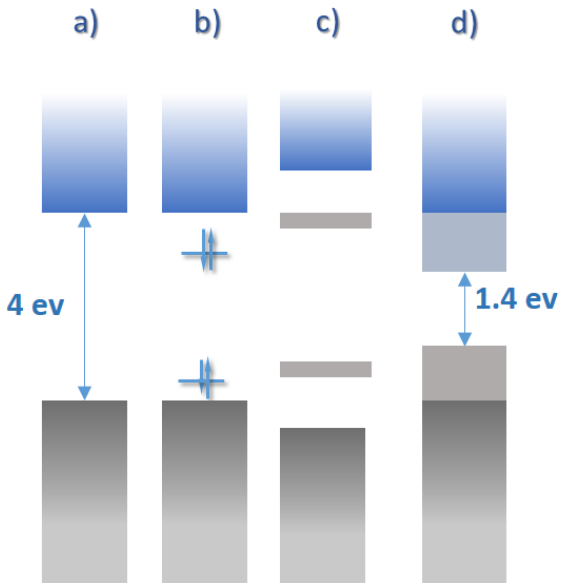

Figure 1.11 valence-effective Hamilton (VEH) band-structure evolution upon doping of polypyrrole: (a) undoped; (b) intermediate doping level: noninteracting bipolarons present on the chain; (c) per monomer 33% doping level[153] (d) per monomer 100% doping level[154].

The redox properties of polypyrrole are the prerequisite to work as the ORR catalyst. The redox reactions of a doped polypyrrole can be explained by the scheme showed in Fig.1.12. The redox reaction of doped polypyrrole can be described as the cation or

anion implosion/expulsion process[155]. These reactions are fast and highly reversible, and thus make polypyrrole a highly promising electrode material for pseudo-supercapacitors[156]. Besides, it is possible to further modify the polypyrrole by integrating other functional molecular groups into the polymer chain via the doping process, such as electro-catalysts, complex agents, polynucleotides and even DNA molecular. These functional groups can enable many possible applications of polypyrrole through its ion exchange process, which includes redox batteries, drug delivery pumps, artificial tissue and neuron simulators[157].

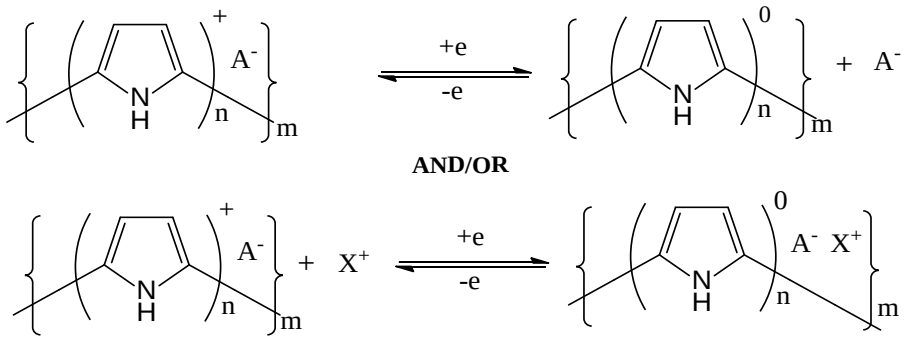

Figure 1.12 the scheme about reversible redox reaction mechanism of polypyrrole, A^- refers anions and X^+ represents the cations)[158]

The bio-compatibility and environmental stabilities of polypyrrole has been investigated comprehensively in vivo circumstance. Unlike PANI which displays acid–base transition associated with colour and conductivity changes, PPy is highly stable at the body temperature in neutral solutions. It has no toxic hazards associated with other aromatic amines[159].

In summary, conductive polymers have many predominant properties for bio-medical applications. However, like most of the current electronic-materials, there are also some inevitable disadvantages of CPs which can potentially deteriorate their electrochemical performances. The doped conductive polymers are usually less conductive than the carbon materials and their redox reversibility tend to be decreased upon reaction time in the aqueous solutions. Therefore, to enhance the electric conductivity and also protect the CPs from overoxidation, carbon based materials are usually chosen to be doped with the CPs. In this research project, two types of novel carbon materials, graphene and carbon nano tubes were selected and in the following section their properties and advantages will be reviewed.

1.2.2 Graphene

Graphene is defined as the flat monolayer of carbon atoms tightly packed into a two-dimensional 2D honeycomb lattice (Fig 1.13)[160]. It is a basic building block for graphitic materials of all other dimensionalities. Due to the unique structure, graphene has many predominant physical and chemical properties. The graphene on one atom thickness is a hundred times more chemically reactive than thicker sheets (graphite thin films)[161]. Besides, graphene has a remarkably high electron mobility at room temperature, with reported values in excess of 15,000 $cm^2 \cdot V^{-1} \cdot s^{-1}$[162]. Its theoretical specific surface area is up to 2630 $m^2\ g^{-1}$[160]. By far, graphene and its derivatives have been studied as one of the most promising materials for all kinds of energy storages devices[163].

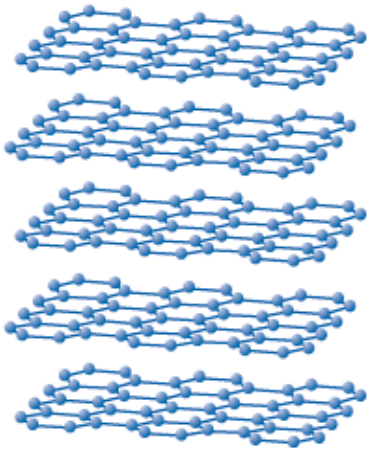

Figure 1.13 the schematic diagram of a two dimensional honeycomb graphene structure[160]

Most of the graphene nano sheets are prepared by the exfoliation of graphite either mechanically or chemically. The research group lead by Andre Geim and Kostya Novoselov at University of Manchester is the first group who extracted single-atom-thick crystallites from bulk graphite. They pulled graphene layers from natural graphite and transferred them onto thin silicon wafer using a processing method called either micromechanical cleavage or the Scotch tape technique[164]. Other physical method such as electron beam (plasma) etching,[165] arc-discharge method[166], chemical vapour deposition (CVD)[167] and ball milling[168] *ect*. However, the most common method is the chemical exfoliation based on the hummers method. This method use the mixture of sulfuric acid (H_2SO_4), sodium nitrate ($NaNO_3$), and potassium permanganate ($KMnO_4$) to oxidise and exfoliate sp2 carbon layers form of graphite[169]. The resulting product of such method is the so called graphene oxide with lots of structural defects and oxygen

functional groups on the carbon sp2 basal planes (Fig1.14). These oxygen functional groups are clustered into rows and islands, resulting in graphitic regions intermixed with islands of oxygen-functionalized atoms. The presence of these functional groups reduces the interplane forces and therefore graphene oxide are electrically insulating materials due to their disrupted sp2 bonding networks[170].

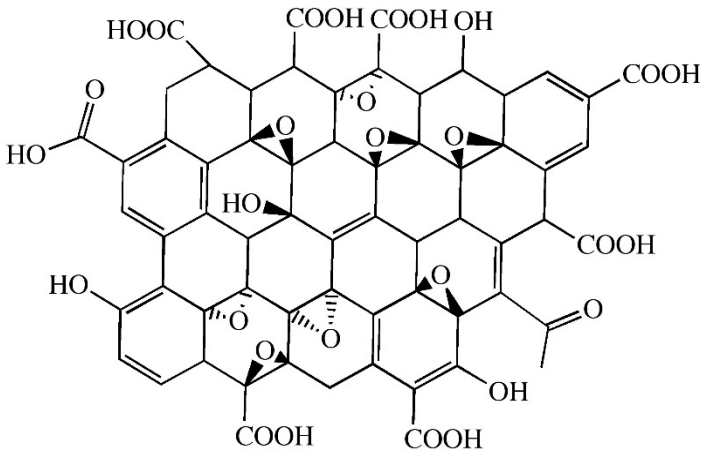

Figure 1.14 the schematic diagram of the graphene oxide structure[170].

Reduction of graphene oxide is necessary to produce highly conductive electrode materials for energy storage devices. The reduction method includes the chemical reduction routine or physical reduction routine. A variety of chemical means may be used to reduce the dispersed graphene oxide, such as sodium borohydride[171], hydrazine hydrate[172], ascorbic acid[173], oxalic acid[174], hydriodic acid[175] or even active metal nano particles[176] *ect*. Physical reduction method mainly includes thermally-mediated reduction[177], UV-assisted reduction[178] *ect*. The experimental conditions of the most representative reduction method of graphene oxide is listed in table 1.4[176].

Table 1.4 the experimental conditions of the most representative reduction method of graphene oxide[175]

Method	Time required
Reduction with H_2 at 450 °C	2 hours
Anneal in vacuum at 1100 °C	6 hours
Reduction with hydrazine vapor at 40 °C and subsequently	22hours
Reduction in hydrazine solution at 100 °C	24hours
Reduction in 98% hydrazine hydrate	One week
Reduction with hydroquinone	20hours
Reduction with dimethylhydrazine at 80 °C	24hours
Multi-step reduction with $NaBH_4$, aryl diazonium salt of	27hours
Reduction with $NaBH_4$ solution (thin film)	2hours
Reduction with 55% HI at 100 °C (thin film)	<1hour
Reduction with Fe powder	6hours
Hydrothermal at 180 °C	6hours
Reduction with benzyl alcohol at 100 °C	24hours
Reduction in NaOH or KOH solution at 50–90 °C	Few minutes

Reduced graphene oxide and graphene oxide all have been considered as promising material for bio-medical applications. At 2011， Kan wang *et al* studied the bio-compatibility of graphene oxide by testing its effects on human fibroblast cells and mice. The author concluded that GO should not be a proper implantable material as it has sever cytotoxicity towards lung cells. The GO fragments can enter into cytoplasm and nucleus, decreasing cell adhesion, and induce cell floating and apoptosis. Exposures to GO may induce severe cytotoxicity and lung diseases[179]. Later at the same year, XY. Zhang *et al* published a more detailed study about the effects of graphene oxide on mice lung cells. The author emphasised the cytotoxicity is dose dependant. No significant pathological changes were observed in all the examined organs when

mice were exposed to 1mg kg^{-1} of GO for 14 days[180]. The bio-compatibility of reduced graphene oxide is less controversial. The reduced graphene oxide has been comprehensively studied for various types of bio-medical applications. H. chen *et al* studied the biocompatibility of chemically prepared flexible RGO film. Their experimental results suggested that graphene paper provides a good substrate for the adhesion and proliferation of L-929 cells, which proved the biocompatibility of the RGO paper[181]. By far, reduced graphene oxide has been considered as one of most important research objects for the bio-medical applications, including biosensors and imagine devices[182, 183], drug delivery[184, 185], cancer therapy[186, 187], antibacterial papers[188-190].

1.2.3 Carbon nano tubes (CNT)

Before the "gold rush" of graphene, carbon nano tubes are the most popular carbon material being studied for all kinds of applications. CNT is consisted of graphitic sheets, which are rolled up into a cylindrical shape (Fig1.15). The diameter of a single walled CNT (SWCNT) is about 1-2 nm[191] and the diameter of multi-walled CNT is around 2-25 nm[192]. The CNTs have been constructed with length-to-diameter ratio of up to 132,000,000:1[193], which is the typical two dimensional nano material. CNT has the chemical and physical strengths because of its unique structure. Chemical bonding of nanotubes is composed entirely of sp2 bonds, similar to those of graphite, which are more strong than the sp3 bonds found in alkanes and diamond[194].

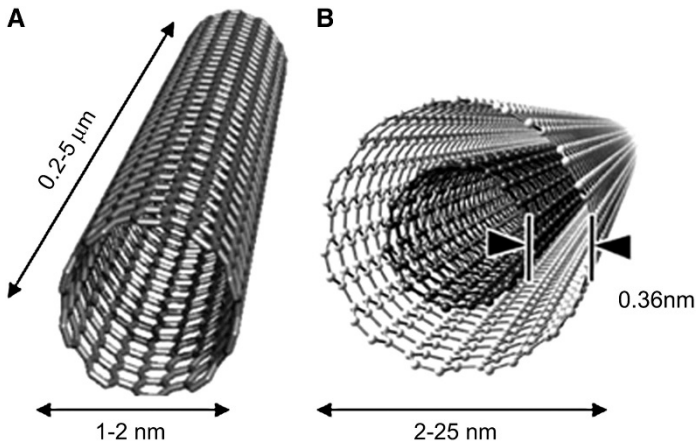

Figure 1.15 structural scheme of (a) single walled CNT (b) multi-walled CNT[195]

Carbon nano tubes has widespread application in various fields, including optics, energy storage, environmental science and bio-medical engineering *ect*[196]. Its toxicity is the major concern for bio-medical applications. The discussions on this topic are still fragmentary and subject to criticism just as that of the graphene oxide. Major issues such as lung toxicity, in vivo absorption, distribution and excretion, cytotoxicity all needs further investigation[197]. However, some of the modified CNTs are tested to be bio-compatible with low cytotoxicity which is suitable for in vivo implantation. Immobilization of CNTs is one of the most effective methods to reduce the toxicity of CNTs. For example, Gordon. G. Wallace *et al* reported the bio-compatibility of immobilized CNTs array on the polymeric matrix substrate[198]. Correa-Duarte *et al.* developed the honey-comb shaped CNTs bundles on the silica substrate and reported no cytotoxicity towards the L929 cells[199]. Other effective method to reduce the toxicity of CNTs is the bio-functionalization[200], such as coupling CNTs with amino acids, DNA

molecular or peptide. Carbon nano tubes are also a popular material for energy storage devices mainly because of its large specific surface areas, high electric conductivity and ease of functionalization. It has been widely utilized as electrode material for supercapacitors, batteries and fuel cells[201].

1.3 Summary

Implantable medical devices (IMDs), such as cardiac pacemakers[14, 24, 202], defibrillators[203], implantable monitors and imaging devices[18, 204], cochlear implants[205], etc., are applied universally in modern clinical diagnosis and treatment. Generally, the IMDs are powered by independent battery systems providing stable and continuous electrical energy output[15]. The current batteries for IMDs mainly include various types of lithium batteries, including Li/I_2-PVP, where PVP is poly 2-vinyl pyridine, Li/V_2O_5, Li/MnO_2, Li/SVO, where SVO is silver vanadium oxide, Li/SO_2 [21, 24, 28], and zinc-air batteries for hearing-aid devices[16, 205]. These batteries are generally designed to power therapeutic devices for chronic diseases (e.g., cardiac pacemakers) because of their high discharge voltage and high energy density. More recently, enormous research work has been carried out to develop microscale implantable medical devices (mIMDs), including implantable diagnosis/monitoring capsules[8], microscale drug pumps[11], implantable microsensing devices[113, 206], *etc*. These devices usually require flexible, microsized, and even non-toxic, implantable power sources that can be easily integrated into the microdevices without inducing a significant size/weight increment. Traditional implantable power sources, including the lithium batteries and zinc-air batteries, all require total encapsulation by stiff metal shells to prevent the leakage of toxic

substances. This inevitably confines their shapes and produces extra weight. Therefore, the significance of developing power sources for those newly developed advanced implantable bio-medical devices arose.

Miniature or flexible aqueous metal-air batteries are currently considered to be one of the most promising candidates for powering mIMDs, which mainly include the zinc-air battery system and the magnesium-air battery system[12, 16, 70]. The volume of these batteries can be easily reduced by reforming the battery into one monolithic flexible structure with a non-toxic and ductile metal anode [207, 208]. Meanwhile, body fluids such as blood plasma, gastric fluid, or urine are all ionic conductive solutions that can be applied as electrolyte[63, 64, 105]. Therefore, it is possible for the battery to be dry-implanted into the human body when sealed by water-permeable films. Meanwhile, paralleled solid state supercapacitors with good flexibility are considered to be a promising candidate for powering advanced IMDs since it possesses adequate energy outputs. Therefore, we choose this as one of our main studying targets.

Design of the power sources for the IMDs generally involves three major tasks. 1), the proper system should be chosen with adequate energy outputs that can power the IMDs. 2) The materials for constructing the devices, including cathode, anode and catalytic component should be optimized in order to enhance the performance of the implantable energy devices. 3) Configuration of the cell is important. The battery should be small sized, packed properly and better to be flexible.

In this project we choose the zinc-air “bio-galvanic” cells and solid state

supercapacitors and their advantages are discussed above by comparing with other energy storage systems. The zinc-air bio galvanic cells have medium range power outputs, low toxicity, low cost and less risk of gas emission (compared to Mg-air battery). Conductive polymers are proofed to have oxygen reduction catalytic activity in previous research work. Besides, most of them are bio-compatible which are suitable for various types of biomedical applications. Hence, we choose one of the most economy and environmental friendly CP, polypyrrole, as the main research target. Properties, fabrication and bio-compatibility of nano structured carbon materials including carbon nano tubes and graphene are reviewed. They are generally of high electric conductivity and large specific surface areas, making them the top choice for incorporating with CPs to optimize the ORR catalytic efficiency for the zinc-air bio galvanic cell.

Chapter 2

Experimental Methods

2.1 Chemical reagents and materials

Reagent	Grade	Company
Acetone	Analytical Reagent	Ajax Finechem
Ethanol	Analytical Reagent	Ajax Finechem
Pyrrole	Analytical Reagent	Sigma Aldrich
Phosphate buffered saline		Sigma-Aldrich
Bovine serum albumin , (lyophilized powder)	Impurity < 0.01%	Sigma Aldrich
4-(2-hydroxyethyl)-1-piperazineethanesulfonic acid	Analytical Reagent	Sigma Aldrich
Sodium carbonate	Analytical Reagent	Sigma Aldrich

Reagent	Grade	Company
Sodium sulfate	Analytical Reagent	Sigma Aldrich
Sodium chloride	Analytical Reagent	Sigma Aldrich
Sodium bicarbonate	Analytical Reagent	Sigma Aldrich
Sodium hydroxide	Analytical Reagent	Alfa Aesar
Potassium permanganate	Analytical Reagent	Sigma Aldrich
Potassium chloride	Analytical Reagent	Sigma Aldrich
Potassium phosphate dibasic trihydrate	Analytical Reagent	Sigma Aldrich
Magnesium chloride hexahydrate	Analytical Reagent	Sigma Aldrich
Calcium chloride	Analytical Reagent	Sigma Aldrich
Toluene-4-sulphonic sodium salt	Analytical Reagent	Sigma Aldrich
Iron(III) chloride	Analytical Reagent	Sigma Aldrich
Multi walled carbon nano tubes	>98% carbon basis	Sigma Aldrich

Reagent	Grade	Company
	6-13 nm × 2.5-20 μm	
Sodium dodecylbenzenesulfonate	Analytical Reagent	Sigma Aldrich
Hexadecyltrimethylammonium bromide	Analytical Reagent	Sigma Aldrich
Ammonium persulfate	Analytical Reagent	Sigma Aldrich
Graphite powder		Fluka
Hydrochloride acid	ACS reagent (37%)	Fluka
Sulphuric acid	98 wt.% in H_2O	Ajax Finechem
Potassium permanganate	Analytical Reagent	Sigma Aldrich
hydroiodic acid	57 wt. % in H_2O	Sigma Aldrich
Zinc	Purity > 99.97%, trace element basis	Sigma Aldrich
Phosphoric acid	85 wt. % in H_2O	Sigma Aldrich

Reagent	Grade	Company
Polyvinyl alcohol	M_w 85,000-124,000	Sigma Aldrich
Cellulose acetate membrane	Pore size, 0.2 μm	Sigma Aldrich
dialysis tube		Sigma Aldrich
Conducting Silver paste		EMS, USA

2.2 Synthesis and Preparation

2.2.1 Preparation of simulated body fluids

The preparation of simulated body fluid used in this project referred to the method introduced by Tadashi Kokubo *et al*[209]. Before preparation, all containers were ultrasonic washed with deionized water, dried under 60°C and cooled down to room temperature.

1) Add 700 mL distilled water into a 1000 mL beaker. Heat it to 36.5±1.5 °C in the water bath with magnetic stirring.. Prepare 0.2 M (100mL) and 1M (15mL) NaOH solutions separately. Weight chemicals and add all the chemicals in the order as listed in Table 2.1

Table 2.1 Adding orders and amounts of chemicals for preparing the simulated body fluid

Chemicals	Purity	Amount (g)
NaCl	>99.95%	5.403
$NaHCO_3$	>99.95%	0.504
Na_2CO_3	>99.95%	0.426
KCl	>99.95%	0.225
$K_2HPO_4 \cdot 3H_2O$	>99.00%	0.230
$MgCl_2 \cdot 6H_2O$	>98.00%	0.311
0.2M NaOH	-	100mL
HEPES	>99.90%	17.892
$CaCl_2$	>95.00%	0.293
Na_2SO_4	>99.90%	0.072

Add 1M NaOH solution dropwisely to adjust the PH to 7.35±0.5, which was determined using a calibrated pH meter.

2) Cool down the as prepared SBF to room temperature and keep it into a refrigerator of 4°C

2.2.2 Preparation Graphite Oxide

Graphite oxide was synthesized from natural graphite by a modified Hummers method. Firstly, weigh 1 g of graphite powder and place it into 500 mL round bottom flask. Add 60 mL H_2SO_4, put the flask in an ice bath, and stir the mixture. Then, Weigh 4 g KMnO4 and gradually add it to the mixture leave mixture in the ice bath for ~5 to 10 minutes after addition. Take the mixture out of the ice bath and keep stirring it at room temperature for 12 hours. The colour of the resulting mixture should be black/dark green after treatment. After the acid treatment, put the flask on an ice bath and slowly add 200 to 250 mL deionized water to the reaction mixture. Add 30% H_2O_2 solution via micro-pipette until the mixture lightens in colour. The colour of the mixture should be bright orange with golden flakes—a brown colour indicates incomplete oxidation. Pour the mixture onto a fritted glass funnel (coarse pore) to isolate solids. Wash solid product with the HCl solution (3% to 10%), followed by the deionized water. Finally, the resulting solids can be collected from the filter and dried under high vacuum. (It should not be an experimental protocol, please write it into a paragraph)

2.2.3 Fabrication of Graphene Oxide

Weigh 50 mg graphite oxide powder and put it in the baker filled with 100 mL deionized water. Ultrasonic the mixture for 40 minutes at 45% amplitude using a Branson sonicator until a uniform yellowish-brown dispersion is obtained (graphene oxide dispersion). After sonication transfer the graphene oxide dispersion into a dialysis bag. Place the dialysis bag into a 1000 mL beaker filled with deionized water for 1 week. This step is set to remove the trace elements in the graphene oxide dispersion.

2.2.4 Electrochemical polymerization

The electrochemical polymerization is carried out by using a three electrode cell with working electrode (conducting substrates), counter electrode (platinum plate) and a reference electrode (Ag/AgCl) (as showed in Fig.2.1). The power supply for electrochemical polymerization is the CHI660 electrochemical working station.

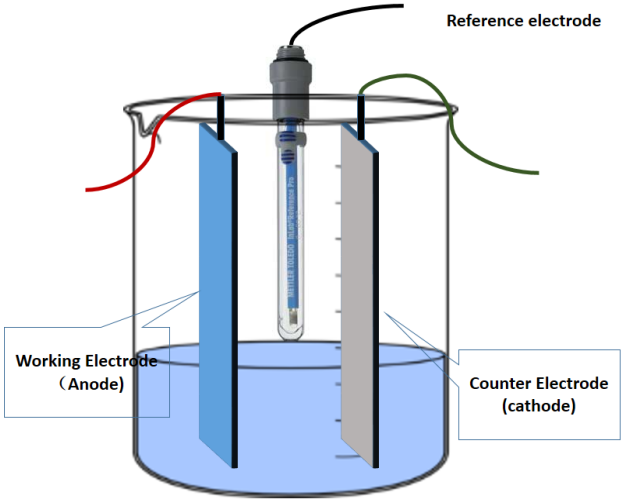

Figure 2.1 a three-electrode electropolymerization cell.

2.2.5 Chemical polymerization

The experimental setup of the chemical polymerization is composed of four parts, including a magnetic stirrer, the nitrogen gas flow pipe, a thermometer and a three necked flask. The configuration of the reactor is depicted in Fig 2.2. The nitrogen gas flow is set to protect the polymerization and the reaction temperature should be controlled under 4°C. Oxidants are added from one of the necks using a plastic syringe or a micro pipette. The whole reaction should be carried out under constant stir.

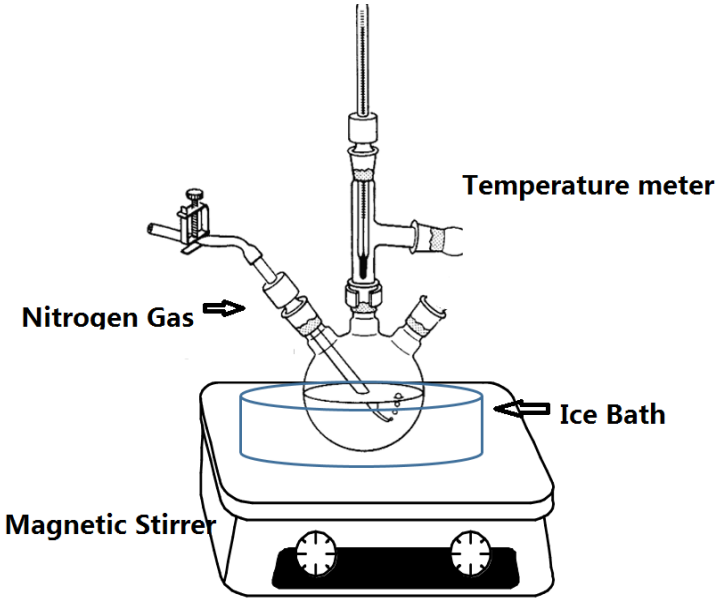

Figure 2.2 Reactor setup for chemical polymerization

2.3 Characterization

2.3.1 Scanning Electron Microscopy (SEM)

Scanning Electron Microscopy (SEM) was utilized for morphological analysis of micro/nano-structure and the SEM is usually equipped with an energy dispersive spectrometer (EDS). SEM/EDS provide chemical analysis of the field of view or analysis of minute particles. In this study, the FESEM images were recorded using a JEOL JSM7500FA cold-field-gun scanning electron microscopy (CFG-SEM) (JEOL Ltd., Japan).

2.3.2 Raman Spectroscopy

Raman spectroscopy is a spectroscopic technique based on inelastic scattering of monochromatic light, usually from a laser source. It relies on inelastic scattering, or Raman scattering, of monochromatic light, usually from a laser in the visible, near infrared, or near ultraviolet range. In this work, Raman spectra were obtained using a confocal Raman spectrometer (Jobin Yvon HR800, Horiba) utilizing 632.8 nm diode lasers.

2.3.3 X-ray photoelectron spectroscopy (XPS)

X-ray photoelectron spectroscopy (XPS) is a surface-sensitive quantitative spectroscopic technique that measures the elemental composition at the parts per thousand range, empirical formula, chemical state and electronic state of the elements that exist within a material. In this project, X-ray photoelectron spectroscopy (XPS) is conducted using a SPECS PHOIBOS 100 Analyser installed in a high-vacuum chamber with the base pressure below 10–8 mbar, X-ray excitation was provided by Al Ka radiation with photon energy hν = 1486.6 eV at the high voltage of 12 kV and power of 120 W. The XPS binding energy spectra were recorded at the pass energy of 20 eV in the fixed analyser transmission mode. Analysis of the XPS data was carried out using the commercial CasaXPS2.3.15 software package.

2.3.4 Atomic force Microscopy (AFM)

Atomic force microscopy (AFM) is a high-resolution scanning probe type microscopy, with demonstrated resolution of a nanometer, more than 1000 times better than the optical diffraction limit. In this work, Atomic force microscopy (asylum, MFP-3D) is applied for topographical scan to measure the film thickness and observe the surface morphology. The MFP-3D uses a flexured scanner and patented NPS^{TM} sensors which measure the exact position of each axis (X-Y).The samples are mounted on an ultra-flat glass substrate glued by conducting silver gel.

2.3.5 Electron transmission microscope (TEM)

TEM are capable of imaging at a significantly higher resolution than light microscopes, owing to the small de Broglie wavelength of electrons. The TEM images provides fine details of the structural information and morphology of the materials. In this project, the JOEL JEM-2011 is employed for observing the morphology of the as prepared graphene oxide and the graphene/conducting polymer composites. The JEOL JEM-2011 is a 200 kV conventional LaB6 transmission microscope capable of 0.16 nm spatial resolution and is ideal for the X-ray microanalysis of nanoscale structures. The microscope also has STEM capability with bright field imaging and chemical profile or elemental mapping.

2.4 Electrochemical Methods

2.4.1 Cyclic Voltammetry

Cyclic voltammetry (CV) is a potentiodynamic electrochemical measurement which can conveniently and reliably elucidate the electrochemical property of the analyte in solution. In cyclic voltammetry, the electrode potential ramps linearly versus time as shown in Figure 2.3. This ramping is known as the experiment's scan rate (V s-1). The potential is applied between the reference electrode and the working electrode and the current is measured between the working electrode and the counter electrode. This technique is widely used to study the mechanism, kinetics, electrochemical active surface area and thermodynamics of electrochemical reaction for either heterogeneous reaction occurring at the electrode surface or homogeneous reaction in solution.

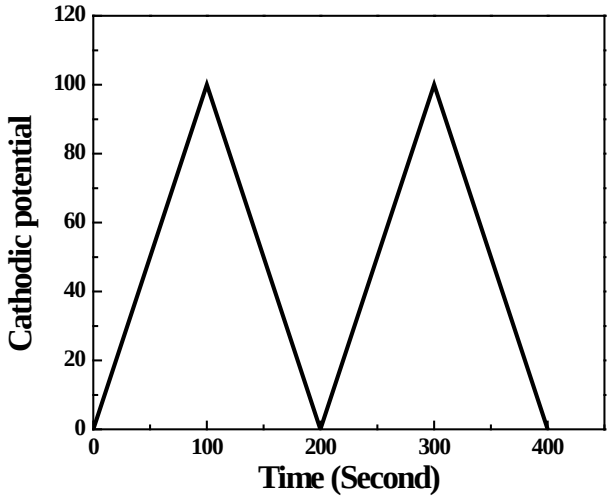

Figure 2.3 An example of a classical style of triangle waveform used in cyclic voltammetry

In this study, CV was mainly used to study the electrochemical redox behaviour and determine the specific capacitance for electrode materials. In general, the CV measurement was performed using a CHI660 electrochemical working station (CH Instruments， Shanghai). CVs of electrodes were recorded in a three-electrode system utilizing a platinum plate counter electrode and an Ag/AgCl reference electrode in the PBS (pH=7.4) solution.

2.4.2 Electrochemical Impedance Spectroscopy

Electrochemical impedance spectroscopy (EIS) is used to characterize electrode processes and complex interfaces for electrode materials. Electrochemical impedance

is usually measured by applying an AC potential to an electrochemical cell and then measuring the AC current signal generated by the cell. This current signal can be analysed as a sum of sinusoidal functions (a Fourier series). In this study, EIS were performed using the CHI660 electrochemical working station (chapter3, chapter4) and a Gamry EIS 3000™ system (chapter 5, chapter 6), and the frequency range spanned from 100 kHz to 0.1 Hz with an AC amplitude of 10 mV at open circuit potential. The EIS results were analyzed by the Zview software.

2.4.3 Cell Test

The charge/discharge performance of the batteries and solid state supercapacitors were tested using the Multi-channel battery testing system (Land CT2001A, Wuhan Jinnuo Electronics Co. Ltd) equipped with the data collection software. The testing current range of the machine is between 1mA – 1000 mA. The system is capable of pre-setting multi-step charge/discharge procedure with different current rate and the cut-off potentials.

2.4.4 Electrochemical quartz crystal microbalance (EQCM)

EQCM is a useful tool to characterize the mechanical properties and ion exchange behaviours of conducting polymers. It monitors the mass changes per unit area by measuring the change in frequency of a quartz crystal resonator. In this study, a

potentiostatic and waveform generator was equipped with the EQCM setup to measure the variation in the electrode mass occurring during the electrochemical processes. 10 MHZ AT-cut crystals (purchased from International Crystal Manufacturing Company, OK, USA) with two vacuum deposited gold electrodes of surface area 0.24 cm^2 area were used. The quartz crystal was mounted in a cell using silicon rubber. The polypyrrole doped with *p*-Toluene-4-sulphonic sodium salt was deposited on the quartz crystal under the protection of nitrogen gas using constant current of 0.5 mA cm^{-2} for 2 minutes. The ion exchange behaviour of the polymer films was characterized in the corresponding electrolyte applied for cell construction.

Chapter 3

Electrochemical synthesized polypyrrole as cathode materials for Zn-polymer battery with various biocompatible aqueous electrolytes

3.1 Introduction

The bio-compatibility of materials for constructing an implantable energy device are the most important issue for the battery design. To satisfy the safety demands, we chose polypyrrole (PPy) as the cathode material, due to its non-toxicity[159, 210], stability[129, 211], and other predominant advantages such as high conductivity[128] and redox reversibility[212]. Zinc was chosen as the anode material due to its moderate interface reactions in the neutral and acidic aqueous electrolytes[79].

Electrochemical synthesis was applied for obtain uniform and thin layers of polypyrrole with firm contact with the conducting substrate (stainless steel mesh). It is a technique that allows producing clean polymers, preventing the unexpected incorporation of ions from oxidant as dopant in the chemical polymerization process[213-215]. Three types of neutral aqueous electrolytes were chosen: NaCl solution, phosphate buffered saline (PBS) solution, and simulated body fluid (SBF). They are all non-toxic electrolytes

ideal for the biocompatible batteries. Zinc was chosen as the anode material, mainly due to its moderate interface reactions in aqueous electrolyte. In addition, Zn is considered to be biocompatible. The amount of zinc commonly consumed in self-selected supplements for adult is 15-100 mg daily.

The discharge performances varied among the batteries with different electrolytes. This phenomenon also evokes the research interest in tracing the relationship between the discharge performance and the reactions in polypyrrole films. The Zn-polypyrrole battery has rarely been reported, especially the Zn-PPy batteries using bio-compatible electrolyte The Zn-polypyrrole batteries exhibit large discharge capacity at low current rate, which makes them a suitable candidate power source for certain applications, such as implantable devices.

A detailed discussion about the reaction mechanism of the polypyrrole cathode is given in this chapter. Raman spectrum is employed as the tool to identify the oxidation levels of polypyrrole before and after discharge, which is in correspondence with the catalytic activity of the polypyrrole[126]. EQCM is employed to study the ion exchange behaviours at the interface between electrolyte and polypyrrole cathode. By analysing the EQCM data, the effect of different electrolytes on the discharge performances can be explained.

3.2 Experimental Methods

3.2.1 Preparation of electrolyte

Three types of electrolyte were prepared for battery construction: 0.1 M NaCl solution, phosphate buffered saline (PBS) solution, and simulated body fluid. The PBS solution was prepared by dissolving one PBS tablet in 200 mL de-ionized water. The ion concentrations of the PBS buffer electrolyte and the SBF are listed in table 3.1. All chemicals were purchased from Sigma–Aldrich and used as received.

Table 3.1 Ion concentrations in SBF and PBS buffer electrolytes.

	Ion concentrations (M)	
	PBS buffer	SBF
Na^+	0.167	0.142
K^+	0.0027	0.005
Mg^{2+}	–	0.00153
Ca^{2+}	–	0.00264
Cl^-	0.1357	0.102
$H_2PO_4^-$	0.01	–
HPO_4^-	0.01	0.001
OH^-	–	0.02

	Ion concentrations (M)	
	PBS buffer	SBF
HCO_3^-	–	0.006
CO_3^{2-}	–	0.004
SO_4^{2-}	–	0.0005
HEPES	–	0.075

3.2.2 Electro-deposition of polypyrrole films

Polypyrrole films were electrochemicaly deposited on stainless steel mesh substrate in an aqueous solution containing 0.1 M freshly distilled pyrrole monomer and 0.1 M *p*-toluenesulfonic acid sodium salt (*p*TSNa). The solution was deoxygenated by nitrogen gas for 30 min before deposition. The polypyrrole films were polymerized under a constant current of 0.5 mA cm^{-2} for 30 min[143].

3.2.3 Battery assembly

Pieces of 1 mm thick Zn foil were cut into squares 1 cm × 1 cm in size and then polished mechanically to remove the oxidation layers. Both the Zn square and the polypyrrole film were immersed in the electrolyte. The areas of both electrodes were restricted to 1 cm^2.

3.2.4 Characterization methods

The growth in weight of the polypyrrole film was monitored in situ by an electrochemical quartz crystal microbalance (EQCM). The thickness and surface morphology were measured using an atomic force microscope (AFM, Asylum Research MFP-3D). Raman spectroscopy was carried out to characterize the redox state of the polypyrrole film before and after discharge, using a JOBIN YVON HR800 Confocal Raman system with 632.8 nm diode laser excitation on a 300 lines/mm grating at room temperature.

The discharge tests were carried out with a battery testing device (Land CT2001A, Wuhan Jinnuo Electronics Co. Ltd), which was interfaced to a computer with software allowing the discharge process to stop at the pre-set cut-off potentials. The cells were discharged from the open circuit potential to 0.7 V with a discharge rate of 40 μA mg^{-1}.

Electrochemical impedance spectroscopy (EIS) was performed using a CHI 660C electrochemistry workstation. The ion exchange behaviour of the polymer films was characterized in the corresponding electrolyte applied for cell construction by EQCM.

3.3 Results and discussion

3.3.1 Properties of polypyrrole films

A polypyrrole film was deposited on a gold coated quartz crystal under the same conditions as for the electrodes used for battery construction. The mass change was observed in situ by converting the change in frequency of the quartz crystal resonator. The mass of polypyrrole increased linearly during the deposition period, which indicated that the conductive film grew normally with the sulfonate doping process[216]. The film conductivities were measured by a four-probe detector, and the average value was calculated to be 70 S m^{-1}.

Atomic force microscope images were obtained within a region of 10 μm × 10 μm (Fig. 3.1) to investigate the surface morphology and thickness of the polypyrrole film deposited on the gold coated quartz crystal. The thickness of the film is less than 1 μm, as shown in Fig 3.1(b). The ultra-thin films have less charge transfer resistance and thus allow much easier ion-exchange with the electrolyte than the thicker ones[217].

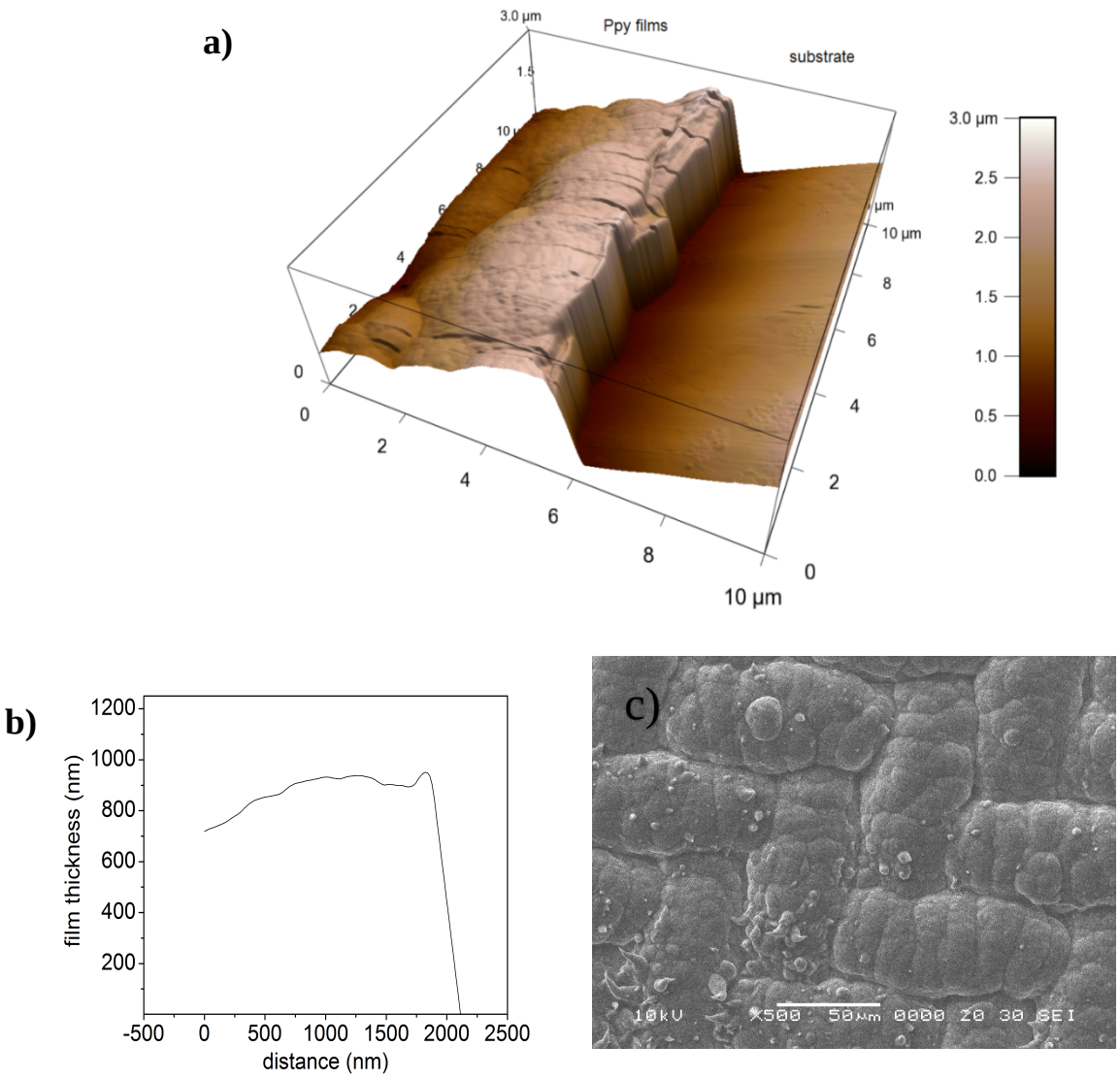

Figure 3.1 AFM image of *p*TS doped PPy film (a), and the film thickness measured along the film profile (b) SEM images of PPy deposited on stainless steel mesh (c)

3.3.2 Battery discharge

Fig. 3.2(a) presents the discharge curves of the Zn/aqueous electrolyte/PPy batteries, which showed very high capacities calculated according to the mass of polypyrrole. The anode reaction can be identified as interfacial dissolution and oxidation of the Zn foil which can be concluded to obey the redox equation below

$$Zn+2OH^{-}\rightarrow Zn_2(OH)+2e^{-}$$

At the beginning of the discharge, an insoluble thin layer of zinc hydroxide is formed on top of the zinc electrode, which causes a sharp potential drop. Zinc dissolution, however, will also cause the pH of the electrolyte to decrease and thus stimulates the dissolution of the insoluble zinc hydroxide[218]. As can be seen from Fig.3.2, the discharge plateau of the Zn/NaCl/PPy battery lasts longer than for the cells using the other two electrolytes, although there is a sharper potential drop at the beginning of discharge. Also, the battery open circuit potentials (OCPs) are in a descending order of NaCl (1.16 V) > PBS (1.09) > SBF (1.02 V).

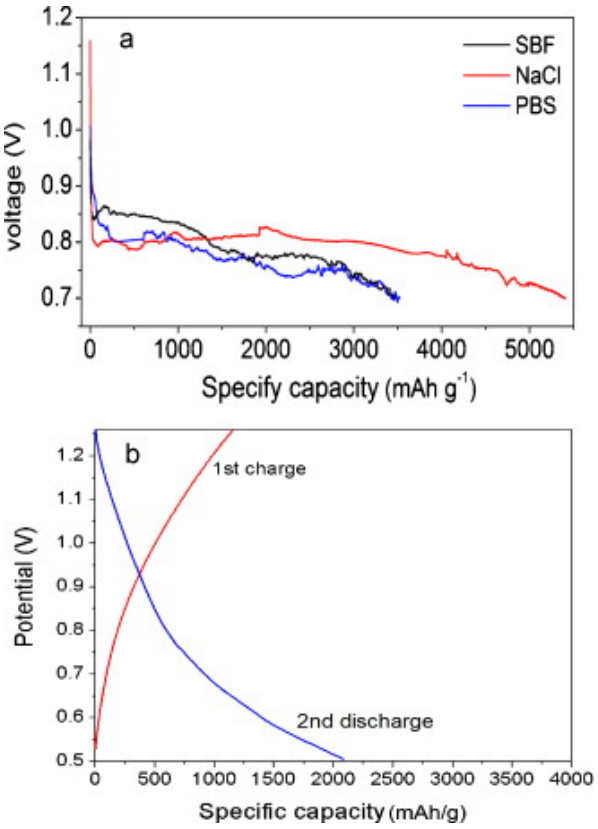

Figure 3.2 (a) Discharge curves of Zn/PPy batteries (40 μA mg^{-1}) with different electrolytes: simulated body fluid (black line), 0.1 M NaCl (red line), PBS buffer solution (blue line); (b) the 1st charge and the 2nd discharge curves of Zn/PPy batteries in SBF electrolyte (160 μA mg^{-1}).

If the mechanism of the battery is simply explained as the redox reactions between the Zn foil and the polypyrrole film, there is definitely not enough polypyrrole to be reduced and thus maintain the long discharge plateaus. This means that the cathode reaction cannot be simply explained as the reduction of conductive polymer. Not much evidence has ever been provided to investigate the role of polypyrrole in batteries. In order to understand the reversibility of the Zn/PPy batteries, the cells with SBF as electrolyte were charged and discharged at a current density of 160 μA mg^{-1} for another

cycle (as shown in Fig. 3.2(b)). It can be seen that the Zn/PPy batteries delivered a reversible capacity of more than 2000 mAh g^{-1}, suggesting its great potential as biocompatible power sources in the practical applications. Figure 3.2 (b) is the 1st charge and the 2nd discharge curves of Zn/PPy batteries in SBF electrolyte under the discharge rate of 160 μA mg^{-1}, which is four times as much as the current density applied for the discharge curves showed in figure 3.2 (a). In such case, the discharge time is much shorter. The Zn anode is not precipitated with the $Zn(OH)_2/Zn^{2+}$ layer, and therefore the diffusion process and interfacial reactions are simple and fast. Besides, the discharge curves showed in figure 3.2 (b) was tested under the oxygen gas bubble. The gas flow also affected the ion diffusion process， which accelerated the ion diffusion process in the electrolyte and stabilized the interfacial reaction on the anode side. Fig 3.3 presents the polarization behaviour of Zn electrodes after immersion for 72 h in the three electrolytes. The corrosion potential of Zn in NaCl solution is higher than in the PBS buffer, implying that the Zn dissolution is easier in the PBS buffer. If the discharge properties are only correlated to the redox reaction on the Zn foil, the battery with PBS buffer electrolyte should have higher capacity than the others, which is untrue according to the discharge curves. This indicates that the battery properties must also be affected by the reactions of the polypyrrole. In order to elucidate the functions of the polypyrrole film, both the electrochemical properties and its redox states before and after discharge are discussed in the following part.

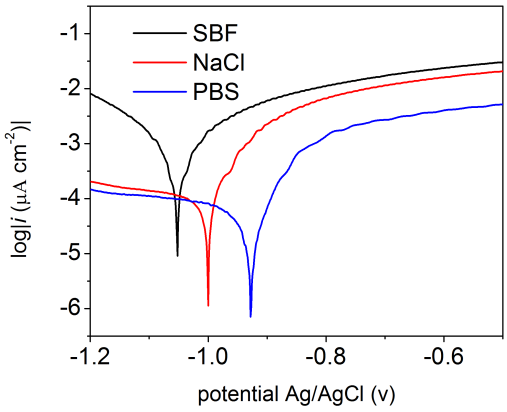

Figure 3.3 Polarization curves of Zn electrodes in different electrolytes: simulated body fluid (black line), 0.1 M NaCl (red line), and PBS buffer solution (blue line).

3.3.3 Electrochemical properties of polypyrrole electrode

Polypyrrole with $p\text{TS}^-$ counterions (PPy/$p\text{TS}^-$) was investigated in different electrolytes by cyclic voltammetry (Fig 3.4) to evaluate the redox characteristics and the charge storage capacities of the electrodes. The thicknesses of the polymer films used for cyclic voltammetry (CV) testing are similar, since the films were deposited under the same conditions. The electrodes were scanned between −1.0 V and 0.3 V (vs. Ag/AgCl) to prevent over oxidation or insulation of the film[219-221]. The oxidation potentials of the films in the three electrodes are at around -0.2 V, however, it is obvious that the peak currents of the PPy films in the NaCl and PBS electrolytes are relatively higher than in SBF, and there are no obvious reduction peaks of polypyrrole in SBF, while the polypyrrole films in both the NaCl and the PBS have a reduction peak at around -0.6 V, which suggests that the film in SBF has less capacity and reversibility.

The relevant reduction and oxidation mechanisms of the PPy electrodes are shown in Scheme 3.1.

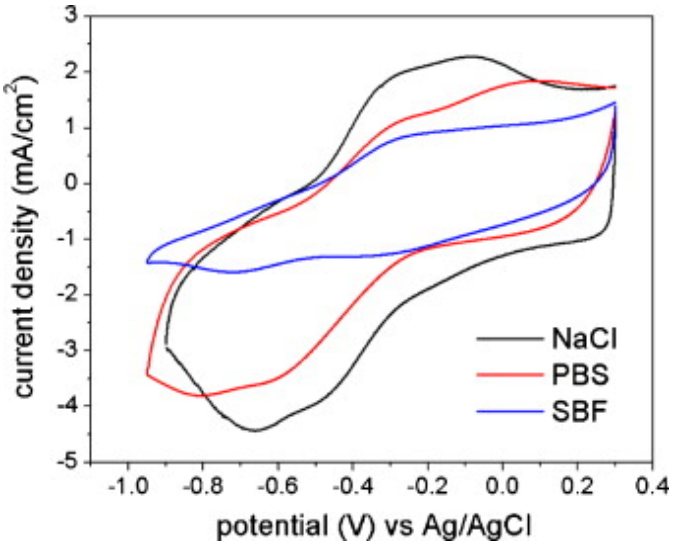

Figure 3.4 Cyclic voltammetric response of (PPy/pTS⁻) in different electrolytes: PBS buffer solution, 0.1 M NaCl, and simulated body fluid; scan rate = 10 mV/s.

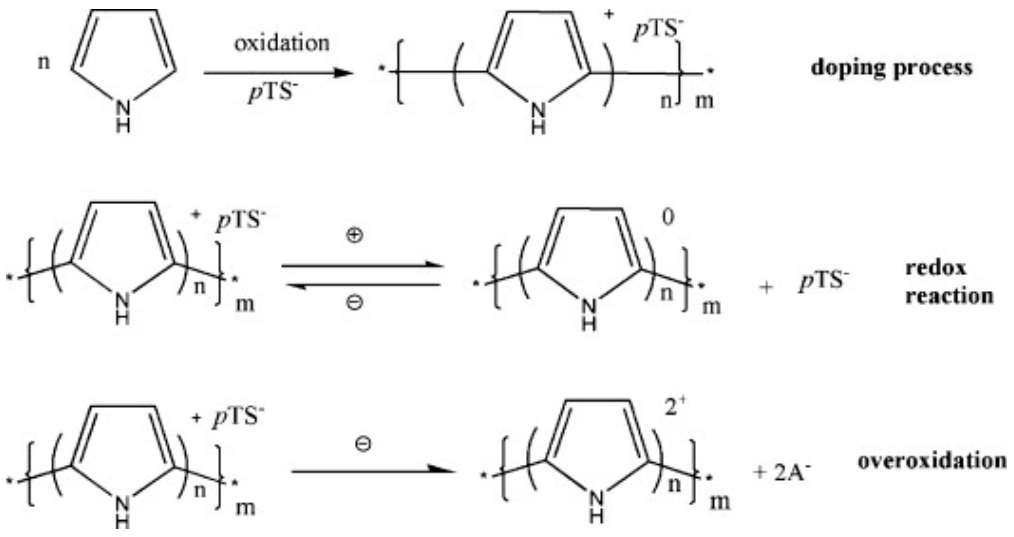

Scheme 3.1. Reduction and oxidation reactions of the PPy films.

The mass change curves converted from the EQCM response are shown in Fig 3.5. Since pTS^{n-} is a large counterion, the ion exchange mechanism of polypyrrole can be mainly ascribed to the cation exchange model[222, 223]. During reduction, the mass increase of PPy/pTS^{n-} is caused by the absorption of cations in the electrolyte so as to neutralize the anionic sulfonyl groups of the pTS^{n-} counterions, while the mass decrease during the oxidation is due to the desorption of cations. The curves in Fig 3.5 reveal that the ion exchange of polypyrrole film in the NaCl solutions is much more violent than in the other electrolytes. This is mainly because the NaCl solution only contains chloride ions, which are univalent small counterions and have little effect on the ion mobilities of Na^+ ions. Thus, the Na^+ ions can be easily inserted into or expelled from the polymer and participate in the redox reaction. Both the SBF and PBS buffer electrolytes contain large amounts of large counterions or organic moleculars ($H_2PO_4^-$ in PBS buffer or 4-(2-hydroxyethyl)-1-piperazineethanesulfonic acid (HEPES) in SBF), which could retard the ion migration.

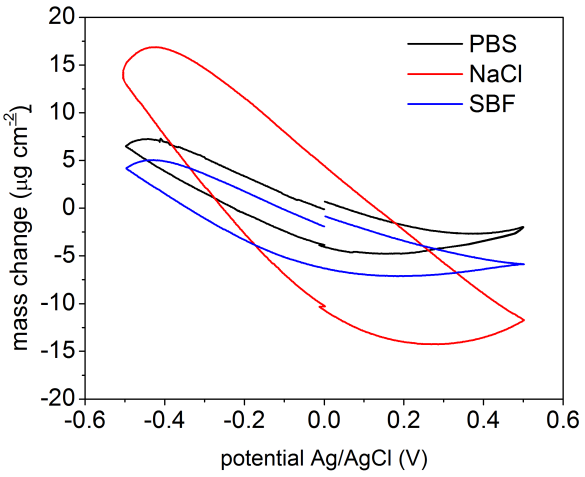

Figure 3.5 Mass change converted from the EQCM frequency response in different electrolytes: PBS buffer solution (black line), 0.1 M NaCl (red line), and simulated body fluid (blue line).

The polymer films were also investigated using electrochemical impedance spectroscopy (EIS) before and after discharge (Fig 3.6 (a) and (b)). Two well-separated patterns were observed: an arc was obtained at high frequencies, which is related to the metal/polymer and polymer solution interface charge transfer processes, while the lines in the low-frequency region indicate capacitive behaviour related to the film charging mechanism. The difference in the real part of the impedance between low and high frequencies could be used to evaluate the value of the electrochemical charge transfer resistance (R_{ct})[224].

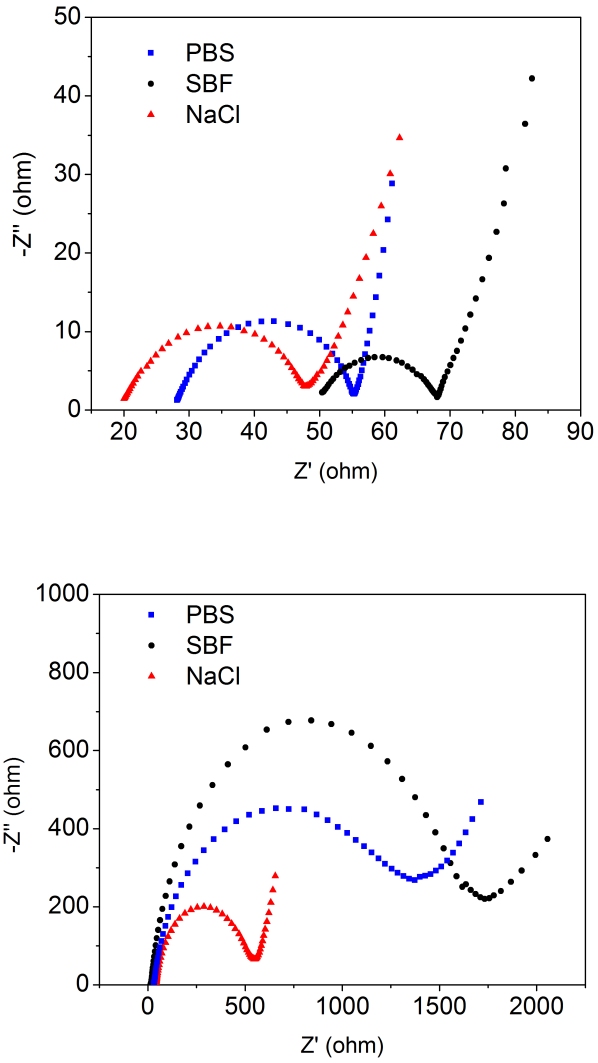

Figure 3.6 Impedance plots of the PPy electrodes in different electrolytes (a) before discharge, and (b) after discharge.

The charge transfer resistance of the films immersed in different electrolytes was calculated as 27.439 ohm (NaCl), 27.35 ohm (PBS), and 19.654 ohm (SBF), respectively. The cells with NaCl and PBS electrolytes have almost the same Rct, while the Rct value for the cell with SBF as electrolyte is lower. After discharge (72 h),

however, the Rct of the cell with NaCl solution as electrolyte (432.89 Ω) is much lower than for the others. The higher charge transfer resistance of the cells using PBS or SBF as electrolyte compared to those using NaCl, maybe due to the absorbed larger HPO_4^{2-}, $H_2PO_4^-$, and HEPES species on the surface of electrodes, which blocked the ion diffusion to some extent.

The redox kinetics of polypyrrole films is mainly controlled by the ion-exchange and charge transfer processes[212]. Since the PPy film has both a faster ion-exchange rate and smaller charge transfer resistance in NaCl solution, the redox activities are higher. Therefore, the discharge capacities of Zn/NaCl/PPy batteries are larger than for the batteries containing the other two electrolytes. The CV curves in Fig 3.5 reveal that the PPy films have similar redox reactivity in both the PBS buffer and the SBF solution. The discharge capacities of batteries with PBS buffer electrolyte, however, are much lower than for the ones with NaCl electrolyte, similar to the case of the Zn/SBF/PPy battery. This is due to the fact that the resistances in both the ion-exchange and charge transfer processes are much larger in the PBS buffer than in the NaCl solution.

3.3.4 Redox states of polypyrrole before and after discharge

Since it has been proved that both the redox kinetics and the associated reactivity have effects on the discharge capacities, it is quite necessary to find out the exact redox process of the polypyrrole films. It is obvious that the reduction of polypyrrole is not the main contributor to the high capacities. The polypyrrole film would lose its conductivity if it were fully reduced and cause the inactivation of the battery. In previous research work, the genuine cathode reaction was explained as oxygen

reduction[72, 102]. No evidence has ever been provided, however, about the redox states of the polypyrrole films before and after discharge, which is the direct proof for elucidating the reaction mechanism.

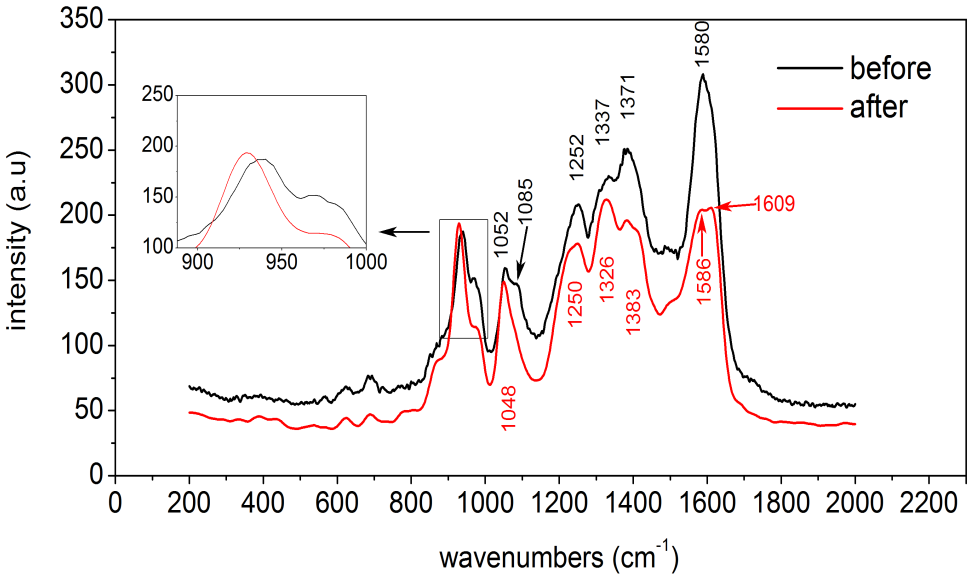

Figure 3.7 Raman spectra of PPy/*p*TS film before and after battery discharge in SBF. The inset is an enlargement of the indicated region.

The redox states of polypyrrole before and after discharge were studied by Raman spectroscopy (Fig.3.7). The peak at around 930cm^{-1} can be assigned to the symmetric stretching mode of the counter ions. It is always accompanied by a broad shoulder on the high frequency side, which is assigned to the incorporated salts[225]. These two vibrational peaks coexist, indicating that the film both before discharge and after discharge is a mixture of polaron and bipolaron polypyrrole. The 980 cm^{-1} band (the broad shoulder at around 930 cm^{-1}) indicates that certain sites on the PPy chain are still in the benzoid form (reduced state). The vibrational mode at 930 cm^{-1}, assigned to a C-

H out-of-plane deformation of the quinoid form, is related to the oxidized sites[226]. The PPy film before discharge clearly has a double peak at about 1052 and 1085 cm^{-1}, which can be assigned to the C-H in-plane deformation of oxidized PPy. In contrast, there is only one peak at 1048 cm^{-1} for the discharged sample, which indicates that the film also contains the fully reduced species. The bands in the high frequency region around 1600 cm^{-1} correspond to the backbone stretching of C=C bonds, and their intensity is correlated to the polymer conductivity[226-228]. The peak intensity of the PPy film after discharge in this region is significantly lower than for the film before discharge, implying that the film partially loses its conductivity after the discharge process[228].

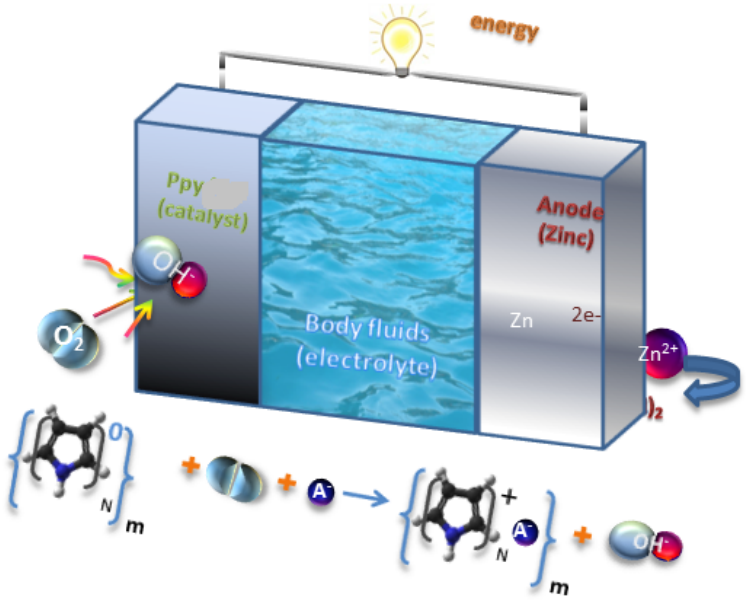

Figure 3.8 The schematic diagram shows the working mechanism of a Zinc/bio fluid/polypyrrole battery system

According to the analysis of the Raman spectra above, the PPy electrodes were partially reduced after discharge, staying in an intermediate state which contains both the reduced and the oxidized forms. Accordingly, the film is not likely to be fully reduced and then oxidized in an orderly way. This means that there are reversible redox reactions that arise on the polymer, as showed in Fig 3.8. The redox reversibility and ultra-high ionic mobility of polypyrrole in these aqueous electrolytes make it clear that its redox reaction is a simultaneous bidirectional process. Polypyrrole can act as an oxygen consumer and thus accelerate the oxygen dissolution. At the same time, it can also be reduced and incorporated with Zn^{2+}, which helps to maintain the zinc dissolution rate.

3.4 Conclusions

The electrochemical properties and reaction mechanism of the Zn/bio fluids /polypyrrole battery has been investigated. The role of polypyrrole film in the battery can be concluded as both that of an oxygen consumer, which can catalyze the oxygen dissolution, and that of an electron acceptor, which helps to maintain the Zn dissolution rate. Both the capacitance and the ion-exchange capability of the PPy films in different electrolytes affect the discharge performance. Higher values of polymer capacitances and ion-exchange rates induce higher capacities. Based on this understanding of such

mechanisms, further modifications of the polymer electrodes can be carried out, which is essential for developing biocompatible batteries with non-toxic aqueous electrolytes.

Chapter 4

Flexible cellulose based polypyrrole – multiwalled carbon nanotube films for bio-compatible zinc battery activated by simulated body fluid

4.1 Introduction

As it has been discussed in chapter.1, an implantable bio-galvanic cell should be small sized and better to be flexible. Monolithic paper based battery is obviously one of the most promising candidate. A paper based battery is composed of thin layers of cathode, anode and separators with these three components tightly integrated together. The sacrificial anode, Zinc foils, are of excellent ductility and therefore the flexibility of the whole battery highly relies on the cathode side.

In previous study, the mechanism of a Zinc/bio fluids/polymer battery has been discussed. The aqueous Zinc-air battery is powered by the redox reaction between zinc anode and oxygen, while its cathode material works as the oxygen reduction catalyst which provides oxygen ions for zinc oxidation throughout the discharge process (as

illustrated in Fig 3.8)[72, 102]. The catalytic activity of cathode material is critical to the battery performance. Therefore, to find the cathode material with excellent ORR catalytic efficiency is also of top-priority for designing such battery.

In summary, the ideal cathode for fabricating a flexible bio-galvanic cell should possess both the flexibility and high ORR catalytic activity. The two decisive factors for achieving high ORR catalytic activity mainly include high specific surface areas and good redox capability of the material. In this chapter, a simple and economical method is developed for making flexible electrodes by coating polypyrrole (PPy)/multiwalled carbon nanotube (CNT) composite on cellulose membranes. Lightweight PPy was coated on miniscule multiwalled CNTs (MWCNTs) via the chemical polymerization method, yielding a nanostructured composite with large specific large surface area and high electric conductivity. The full battery was constructed using the deposited PPy/CNT thin layer as the cathode and simulated body fluid as the electrolyte. Previous work has proved that the biocompatibility of immobilized multiwalled-CNT-based implants is comparable with that of the existing medical grade materials, which proves that it is capable for bio-medical application.

The effect of cathode materials with different PPy content on the battery discharge performances is discussed based on the results of various electrochemical testing methods. To simulate the “in-vivo” environments, bovine serum albumin is added into the simulated body fluids. The effect of protein components on the discharge performances is also discussed.

4.2 Experimental

4.2.1 Preparation of the CNT-PPy composite thin layer

The MWCNTs were treated with a refluxing acid mixture of 65% HNO_3 and 98% H_2SO_4 ($v(HNO_3)$: $v(H_2SO_4)$ = 3:1) for 12 hours. The carboxylic acid group functionalized MWCNTs were then centrifuged and rinsed with deionised water to remove the acid residues until its pH reached 6.5. The obtained functionalized MWCNT powder was dried at 60 ^oC in a vacuum oven for 12 hours. 40 mg of the as-prepared powder was uniformly dispersed in 100 mL deionised water by ultrasonication using 500 mg sodium 4-dodecylbenzenesulfonic acid (SDBS) as the surfactant. The PPy/CNT composites were prepared by chemical polymerization. Three types of composites were prepared, keeping the amount of CNT constant, but varying the pyrrole monomer concentration as: 0.2, 0.1, and 0.05 M. 100 mL 0.25 M iron trichloride solution was added dropwise into the pyrrole-CNT suspension placed in an ice bath. The resulting mixture was left overnight to achieve full oxidation, followed by filtration, thorough rinsing, and vacuum drying.

4.2.2 Battery construction

0.4 mg mL^{-1} PPy/CNT aqueous suspension was prepared by ultrasonication. Thin layers of PPy/CNT were deposited on cellulose filter membranes by filtrating 10 mL of

the suspension. The PPy/CNT thin layer was applied as the cathode material, with the cellulose membrane as the substrate and separator. Fig 4.1 shows the flexibility of the cellulose based PPy/CNT electrodes.

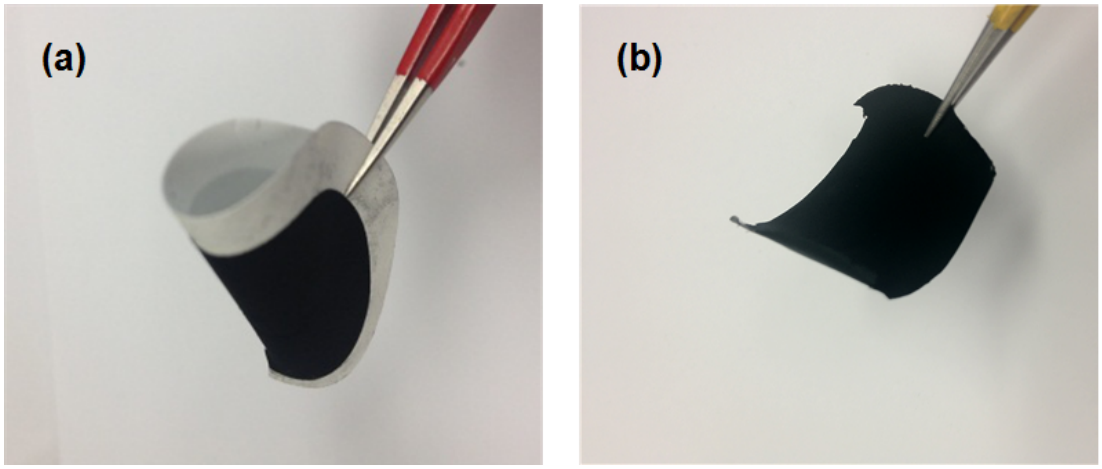

Figure 4.1 Digital picture of (a) a folded cellulose based PPy/CNT electrode and (b) peeled off PPy/CNT film

Zinc foil was cut to a size of 1 × 1 cm, polished, and washed with acetone prior to use. Both the zinc anode and the PPy/CNT cathode were immersed in a beaker filled with electrolyte to a fixed height of 1 cm. The electrolyte was the modified simulated body fluid with content of 0, 8, 16, and 40 g L^{-1} bovine serum albumin (BSA). This electrolyte has the same ionic composition as human blood plasma, but without glucose or protein. The concentrations of BSA in the three types of electrolyte were 10%, 20%, and 40% of the BSA protein in genuine body fluid, which is reported as 80 g L^{-1} [229]. A full battery sealed by water permeable paper has also been made and tested using the SBF

electrolyte containing 8 g L^{-1} BSA.

4.2.3 Characterization

The surface morphology of the PPy/CNT powder was observed with a field emission scanning electron microscope (FESEM, JOEL 7500) and a transmission electron microscope (TEM, Philips CM12) with an accelerating voltage of 120 kV. The Raman measurements were performed with a JOBIN YVON HR800 Confocal Raman system with 632.8 nm diode laser excitation on a 300 lines/mm grating at room temperature. Electrochemical impedance spectroscopy (EIS) measurements and cyclic voltammetry (CV) were carried out on a CH workstation (CHI 660B). The battery discharge tests were carried out by using a battery testing device (Landlt Co., China). The cells were discharged from the open circuit potential to 0.6 V under a discharge current density of 60 μA cm^{-2}. Polarization curves of Zn foil in different electrolytes were also obtained with the CH workstation (CHI 660B). Specific areas of samples were tested with a Nova 1000 Brunauer-Emmett-Teller (BET) surface area analyzer, and the sample conductivities were tested with a JANDEL RM3 four point probe instrument.

4.3 Results and discussion

4.3.1 Characterization of as-prepared PPy/CNT composites

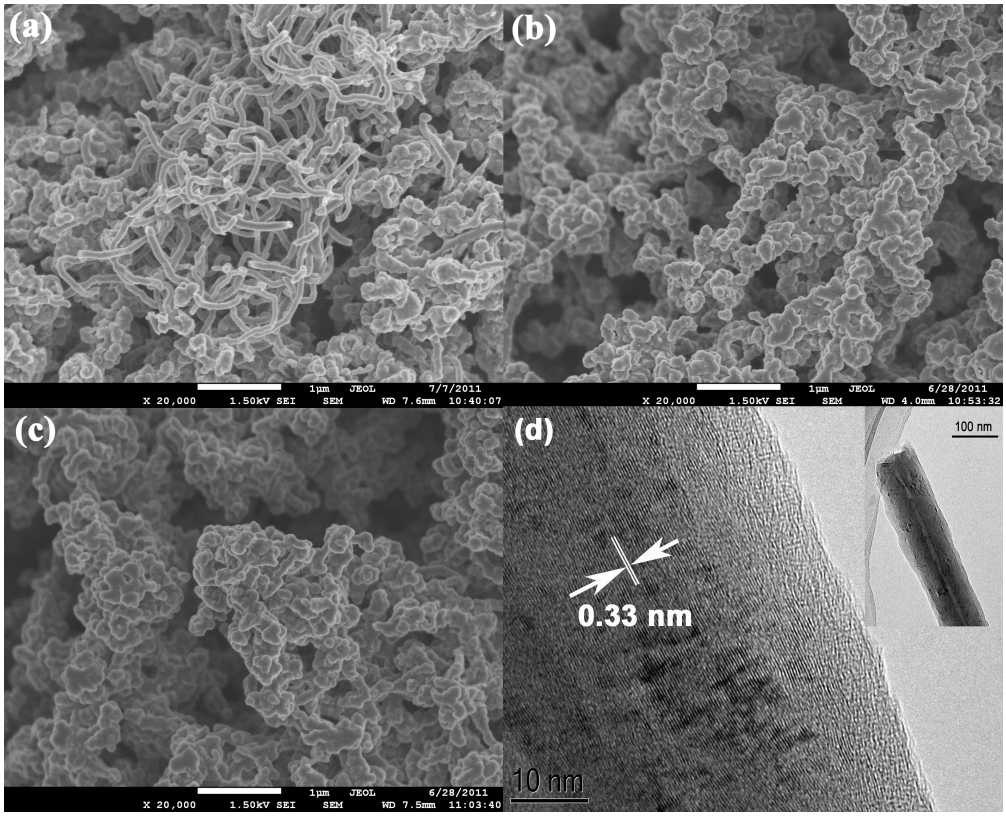

Figure 4.2 FESEM images of PPy/CNT composites prepared from (a) 0.05 M pyrrole + 0.4 mg mL^{-1} CNT, (b) 0.1 M pyrrole + 0.4 mg mL^{-1} CNT, and (c) 0.2 M pyrrole + 0.4 mg mL^{-1} CNT; and (d) high resolution TEM image of composite made from 0.1 M pyrrole + 0.4 mg mL^{-1} CNT.

Fig.4.2 (a-c) presents FESEM images of PPy/CNT composites synthesized with different monomer concentrations. The composites generally have a porous structure

formed with the entangled PPy-coated CNTs or CNT network. As the monomer concentration increases, however, the agglomeration of PPy particles becomes more noticeable, and this decreases the specific surface area, as shown in Fig. 2(c). According to the BET and conductivity testing results, the specific surface areas of these composites prepared from 0.2 M pyrrole, 0.1 M pyrrole, and 0.05 M pyrrole were 16.07 $m^2 g^{-1}$, 20.14 $m^2 g^{-1}$, and 24.65 $m^2 g^{-1}$, respectively. They exhibited conductivity of 94 S cm^{-1} (0.05 M pyrrole + 0.4 mg mL^{-1} CNT), 72 S m^{-1} (0.1 M pyrrole + 0.4 mg mL^{-1} CNT), and 57 S cm^{-1} (0.2 M pyrrole + 0.4 mg mL^{-1} CNT). This indicates that an excess amount of pyrrole monomers were polymerized on the PPy-CNT surface induces the stacking of PPy particles and reduces the specific surface area of the composite. The composite synthesized with 0.1 M pyrrole displays a relatively uniform porous structure, as shown in Fig.4.2 (b). Its TEM image in Fig.4.2 (d) clearly demonstrates that the hollow MWCNT structure was encapsulated by PPy, which was uniformly polymerized on the surface of the CNT. The lattice spacing of MWCNTS is about 0.34nm and the lattices are dislocated at the interface which suggests strong bonding between the MWCNT lattice and polypyrrole coating layer.

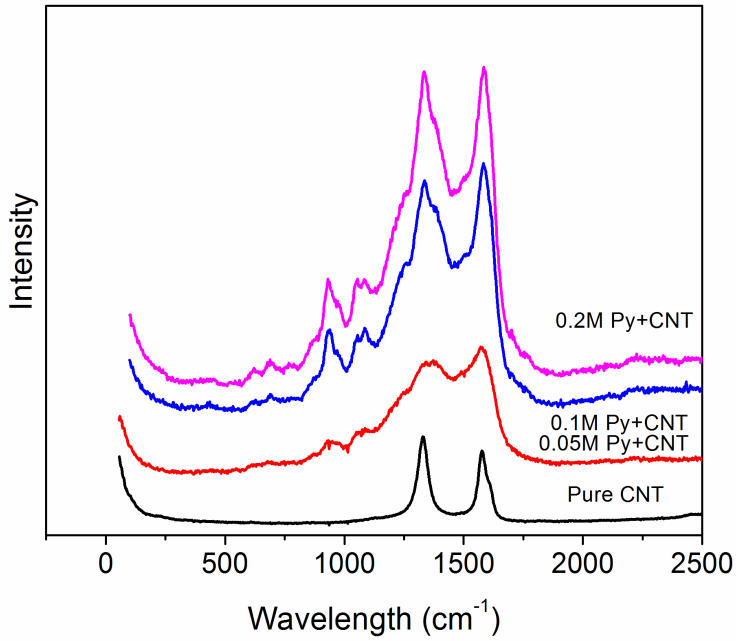

Figure 4.3 Raman spectra of (a) pure MWCNT and composites prepared from (b) 0.05 M pyrrole + 0.4 mg mL^{-1} CNT, (c) 0.1 M pyrrole + 0.4 mg mL^{-1} CNT, (d) 0.2 M pyrrole + 0.4 mg mL^{-1} CNT.

To study the molecular structure of the resulting PPy/CNT composites, Raman spectroscopy was carried out to provide sufficient evidence. Fig.4.3 presents the Raman spectra of pure functionalized carbon nanotubes and of composites prepared with different PPy content. All three types of PPy/CNT composite display identical doped PPy structures. The peaks at 1050 and 968 cm^{-1} are associated with the quinonoid polaron structure, and those at 1086 and 940 cm^{-1} are associated with the quinonoid bipolaron structure[225]. The peak at 1244 cm^{-1} is considered to be due to the N—H in-plane deformation. The pure carbon nanotubes have two very strong peaks at 1355 and 1580 cm^{-1}, which can be respectively associated with the D mode and G mode of carbon

bonding vibrations[230, 231]. The ranges of these two strong peaks overlap with the ring stretching peak of PPy at 1314 cm^{-1} and its C=C backbone stretching peak at 1610 cm^{-1}. Those peaks associated with bonds of PPy indicate that the PPy has been successfully polymerized on top of the tubular shells of the carbon nanotubes. There is an obvious trend, however, that a composite with less PPy content displays sharper D band and G band stretching peaks which overlap the ring stretching and C=C backbone stretching peaks.

4.4 Battery testing with different PPy/CNT electrodes

The batteries used zinc foil as the anode material and protein free simulated body fluid (SBF) as the electrolyte. They were assembled with cathodes made from all three types of PPy/CNT composites. The mechanism of such a battery has been considered to be similar to that of a primary metal air battery, according to the previous studies on magnesium/conductive polymer batteries with aqueous electrolyte[72, 102]. In this battery system, zinc is the unlimited sacrificial electrode, while PPy/CNT acts as the catalyst for the oxygen reduction process.

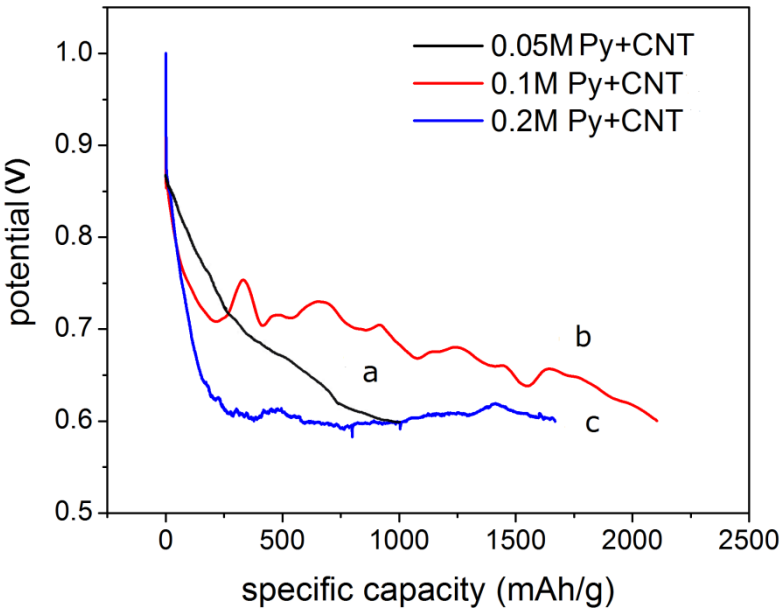

Figure 4.4 Discharge curves of batteries with different cathodes: (a) 0.05 M pyrrole + 0.4 mg mL^{-1} CNT, (b) 0.1 M pyrrole + 0.4 mg mL^{-1} CNT, (c) 0.2 M pyrrole + 0.4 mg mL^{-1} CNT in SBF electrolyte (current density = 40 mA g^{-1}).

Fig.4.4 displays the discharge curves of the three batteries under the current density of 60 µA cm^{-2}. The battery with the electrode prepared from 0.1 M pyrrole + 0.4 mg mL^{-1} CNT clearly shows the best discharge performance, with a higher discharge plateau voltage, which is almost 0.1 V higher than those of the other two types, and its discharge potential drops much more slowly. The differences in discharge performances can be mainly ascribed to the catalyst efficiency of the cathode materials for oxygen reduction, whilst the catalyst efficiency is decided by the properties of the cathode materials, including the specific surface areas, conductivity, and redox capabilities. The cathode material with higher specific surface area and redox capabilities is generally more efficient as the oxygen reduction catalyst. Inside the composite, polypyrrole is the redox

active material and CNT is the supporting framework to enhance the material conductivity. The cathode material made from 0.1 M Py +CNT get the balance of enhanced conductivity and redox capability, and thus it shows the best discharge performance. The FESEM images (Fig.4.2) have provided evidence that the agglomeration of PPy becomes more significant as the PPy content increases in the composite. This induces a decrease in the surface area, where the electron transportation and redox reaction occur. Meanwhile, excess PPy coated on CNT reduces the conductivity offered by the carbon nanotubes. Thus, the discharge plateau of the battery with its cathode made from 0.2 M pyrrole + CNT displays a lower plateau voltage due to its relatively lower specific surface area and lower conductivity. On the other hand, polypyrrole works as an oxygen reduction catalyst, which helps to retain the discharge plateau.

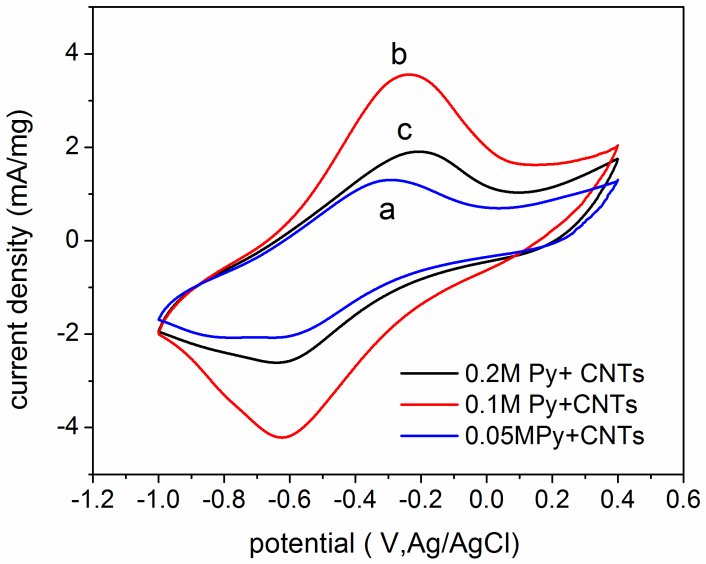

Figure 4.5 Cyclic voltammetry of different electrodes in SBF electrolyte: (a) 0.05 M pyrrole + 0.4 mg mL^{-1} CNT, (b) 0.1 M pyrrole + 0.4 mg mL^{-1} CNT, (c) 0.2 M pyrrole + 0.4 mg mL^{-1} CNT (scan rate = 10 mV s^{-1}).

Fig. 4.5 shows cyclic voltammetry (CV curves) at the same scan rate (10 mV S^{-1}) of all three cathodes made from the different composites. The maximum potential of the redox peaks suggests that the redox capabilities of the composites made from 0.05 M PPy + CNT are significantly lower than the other two types of cathode materials. This could explain the absence of a discharge plateau in the battery with the cathode made from 0.05 M pyrrole + CNT, in which case, the oxygen reduction is quickly inactivated when the PPy/CNT composite completely loses its redox activity. To verify this, electrochemical impedance spectra of all three types of batteries were collected after 6 hours discharge (when the batteries with cathode made from 0.1 M pyrrole + CNT and 0.2 M pyrrole + CNT reach their discharge plateaus) and are shown in Fig. 4.6.

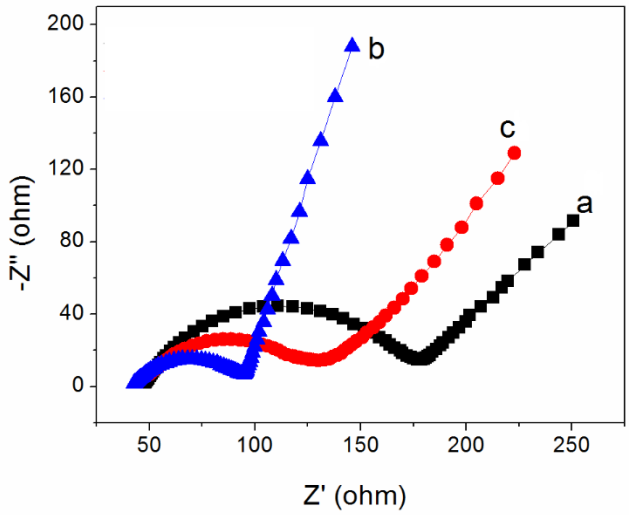

Figure 4.6 Electrochemical impedance spectroscopy of batteries with electrodes made from (a) 0.05 M pyrrole + 0.4 mg mL^{-1} CNT, (b) 0.1 M pyrrole + 0.4 mg mL^{-1} CNT, (c) 0.2 M pyrrole + 0.4 mg mL^{-1} CNT after 6 hours discharge.

The first semicircles displayed in the curves usually correspond to the interface charge transfer resistance, together with the contact resistance between the electrodes and the current collector[232, 233]. The charge transfer resistance, R_{ct}, of the electrode made from 0.05 M pyrrole + CNT is calculated as 126 Ω, which is significantly larger than for the other two types of batteries. The large internal resistance can be mainly ascribed to the inactive cathode material, which loses its function as the oxygen reduction catalyst after a few hours of discharge, which consequently induces a constant drop in the discharge potential.

4.4.1 Testing of battery performance using 'simulated body fluid' as electrolyte

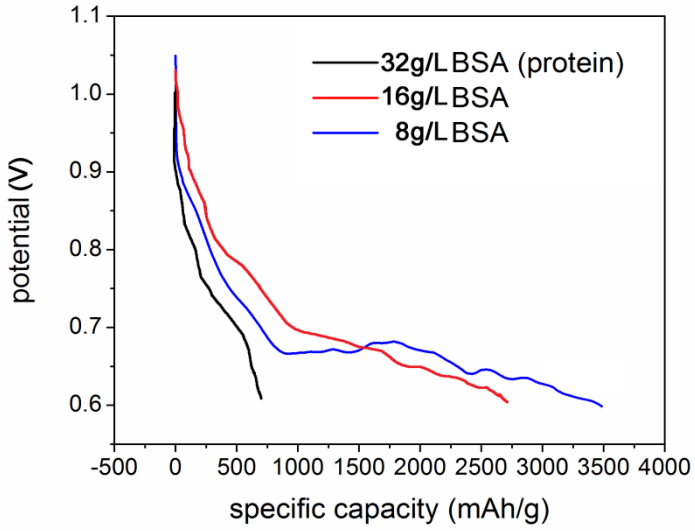

Figure 4.7 Discharge curves of batteries with simulated body fluid electrolyte containing (a) 8 g L^{-1} BSA, (b) 16 g L^{-1} BSA, (c) 32 g L^{-1} BSA.

According to the discussion in section 4.3.2, it is found that the cathode material made from 0.1 M pyrrole + CNT has the best discharge performance in the protein-free simulated body fluid. Therefore, in this section, only this type of cathode was used to assemble the batteries being tested in electrolytes with different protein concentrations. Fig 4.7 presents the discharge curves of batteries using different electrolytes with different levels of bovine serum albumin (BSA). It is notable that all the discharge curves turn out to be smoother than those in Fig 4.4, indicating that the discharge

potentials are stabilized by the protein. Meanwhile, the discharge plateaus are prolonged significantly after adding 8 g L^{-1} and 16 g L^{-1} BSA.

It is interesting to discuss the effects of the BSA concentration on the battery discharge processes. The anode and cathode reactions of the battery can be described by the electrochemical equations below

Cathode $PPy^{+} + e^{-} \leftrightarrow PPy^{0}$

$O_2 + 2e^{-} + 2H_2O \rightarrow 2OH^{-}$

Anode $Zn \rightarrow Zn^{2+} + 2e^{-}$

$Zn^{2+} + 2OH^{-} \rightarrow Zn(OH)_2$

$Zn(OH)_2 \rightarrow ZnO + H_2O$[234]

The cathode reaction is mainly the oxygen reduction process along with the reversible redox process of PPy, while the anode reaction is the oxidation process of zinc described by the equations above. The BSA molecule can affect the electron transfer process and thus slow down the redox reactions on both sides, especially the interface reactions of the zinc electrode.

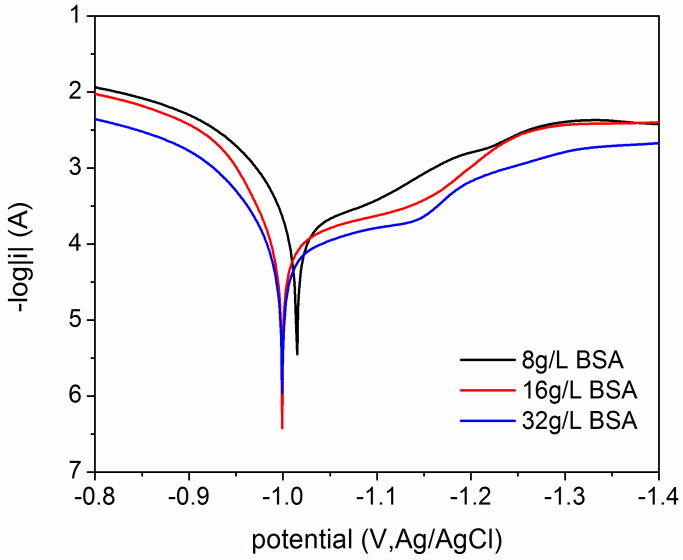

Figure 4.8 Polarization curves of zinc foil in simulated body fluids containing (a) 8 g L^{-1} BSA, (b) 16 g L^{-1} BSA, (c) 32g L^{-1} BSA.

Fig.4.8 shows the polarization curves of zinc foil in the three types of electrolyte. In the presence of the organic substances, the cathodic wave shows characteristic inhibition waves. The waves can be explained as due to the absorption of the organic species, and they demonstrate the inhibition efficiency[235]. The length and height of such a wave correspond to the inhibition efficiency, which is mainly decided by the BSA concentration. This can explain why the discharge potential drops so quickly in the battery with electrolyte containing 32 g L^{-1} BSA. In this case, a large amount of big organic molecules can be adsorbed and cover the zinc surfaces, which hinders the interface reaction of the zinc electrode. Diffusion of the oxidation products on the zinc electrode is blocked by the adsorbed organic molecules, making the battery inactive. When the concentration of the organic molecules is low, however, it could slow down

the loss of electrons from the zinc electrodes and thus allow the battery to display a longer discharge plateau, as shown in Fig. 4.7(c).

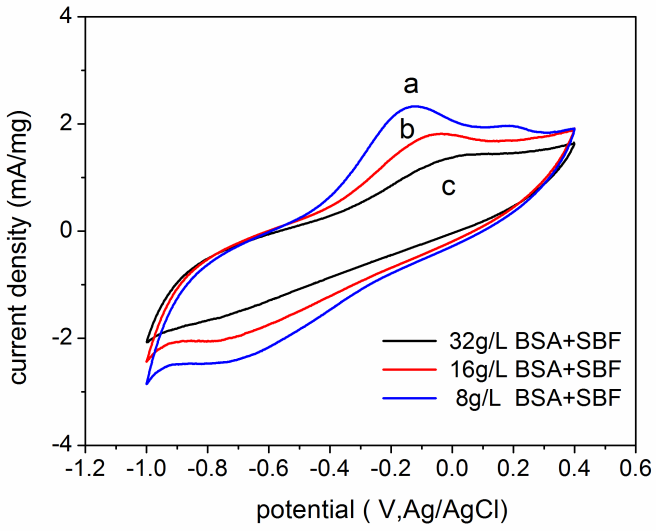

Figure 4.9 Cyclic voltammetry of electrodes made from 0.1 M pyrrole + 0.4 mg mL^{-1} CNT in electrolyte containing (a) 8 g L^{-1} BSA, (b) 16 g L^{-1} BSA, (c) 32 g L^{-1} BSA (scan rate 10 mV s^{-1}).

On the other hand, the redox peaks in the CV curves (Fig. 4.9) of the batteries with different BSA concentrations in the electrolyte have generally become broader than those of the electrodes tested in protein-free SBF. This indicates that the ionic charge transfer processes were retarded when BSA was added to the electrolyte. The bovine serum albumin is a long chain molecule composed of several hundred of amino acids. The viscosity of its aqueous solution increases significantly with increasing solute concentration. Therefore, the retardation of ionic charge transfer becomes more obvious

when the BSA concentration increases, inducing a drop in the discharge plateau and lower discharge capacity.

4.4.2 Assemble a sealed Battery

The battery is targeted for dry implantation and to then be activated by body fluids. Thus, we have developed a sealed battery which consists of zinc foil (anode), PPy/CNT deposited cellulose membrane (cathode and separator), and stainless steel mesh (current collector). A picture of a battery of this type is shown below in Fig. S1. The stainless steel mesh was pasted onto the electrodes using highly conductive silver paste, and the battery was sealed with water permeable filter paper.

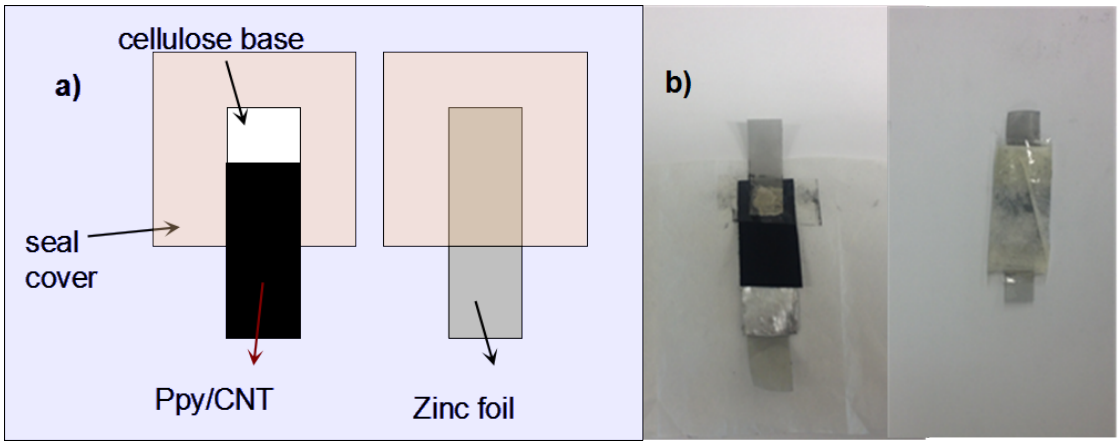

Figure 4.10 Schematic graph (a) and Digital photographs (b) of a sealed PPy|CNT|Zn battery. (The PPy/CNT composite used in this battery is made from 0.1 M Py + 0.4mg mL^{-1} CNT.)

Fig. 4.11 shows the discharge curve of this battery at the current density of 40 mA/g (calculated based on the actual weight of PPy/CNT electrode). The capacity of the sealed cell is 326 mAh/g, which is lower than that of the open cell. The specific capacity of the sealed battery is much lower than that of the open cell, mainly because the oxygen concentrations of these two cells are different. Less oxygen participated in the anode reaction '$2Zn^{2+} + O_2 + 2H_2O + 4e^- \rightarrow 2Zn(OH)_2$' in the sealed battery, causing the decrease in the battery capacity.

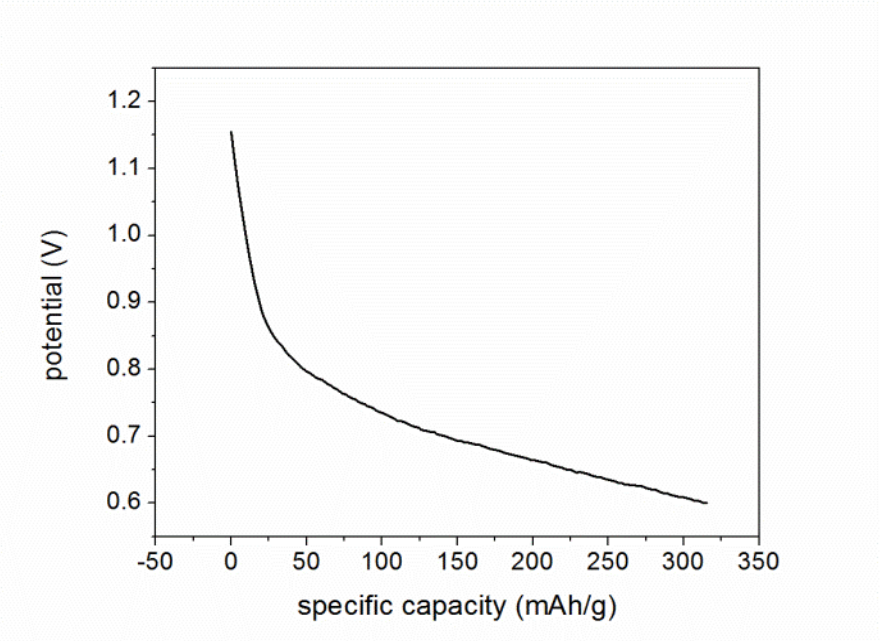

Figure 4.11 Discharge curve of the sealed PPy/CNT|Zn cell immersed in the revised simulated body

4.5 Conclusions

Three types of PPy/CNT composite with varied PPy content were successfully synthesized by chemical polymerization. The morphologies of the composites showed porous structures with PPy particles coated on CNT fibers. A series of batteries was constructed by using PPy/CNT composite deposited on cellulose paper as the cathode and zinc foil as the anode. The composite made from 0.1 M pyrrole + 0.4 mg mL^{-1} CNT had the best discharge performance. It also had the best stability and the highest discharge capacity in the simulated body fluid. Experiments aimed at testing the battery with electrolyte containing proteins were conducted with this type of cathode material. It was found that a small amount of BSA protein can stabilize the discharge potential and prolong the discharge plateau. However, as the protein concentration increased, the ionic charge transfer process can be retarded by the large protein molecules, inducing the decrease of discharge plateau potential and the discharge capacity.

Chapter 5

One-step synthesis of Graphene / polypyrrole nano fiber composites as cathode material for bio compatible Zinc/polymer battery

5.1 Introduction

As it has been concluded in chapter 4, developing the high performance cathode material for the Zinc/body fluids/polymer composites battery system is the key issue for achieving longer battery service life. Carbon based materials are obviously ideal supporting materials to be incorporated with the conducting polymer for improving the ORR catalytic efficiency. In chapter 4, carbon nanotubes was applied as the framework to enlarge the surface areas and enhance the electric conductivity of the cathode material and consequently improve its ORR catalytic efficiency.

Compared with carbon nano tubes, the reduced graphene oxide is advantageous in some aspects for bio compatible battery applications. First of all, the reduced graphene oxide (RGO) are generally considered to be bio-compatible if it is reduced by a non-toxic reducing agent[181, 236, 237]. Graphene nano sheets has a 2D plane structure composed of sp2 carbon atoms, and therefore its electron transfer resistance is extremely low and its

theoretical specific surface areas is large[160]. Graphene can be an ideal base material to load the nano particles or fibres to produce 3D nano structured composites for all kinds of energy storage devices[238-240].

On the other side, polypyrrole can be synthesised as nano particles, nano tubes or nano particles by either soft templates or hard templates, as discussed in chapter.1 (1.2.1.1). In this chapter, we choose micro-micelles templates to synthesis the polypyrrole fibres and sandwich the fibres between the graphene nano sheets. The reaction mechanism scheme is showed as Figure 5.1. The positively charged surfactant micelles can be sandwiched between negatively charge graphene oxide (GO) via electrostatic[241]. The pyrrole monomers are encapsulated into the micelles and polymerized after adding the oxidation agents and therefore retain the same shape as the inner wall of the micelles.

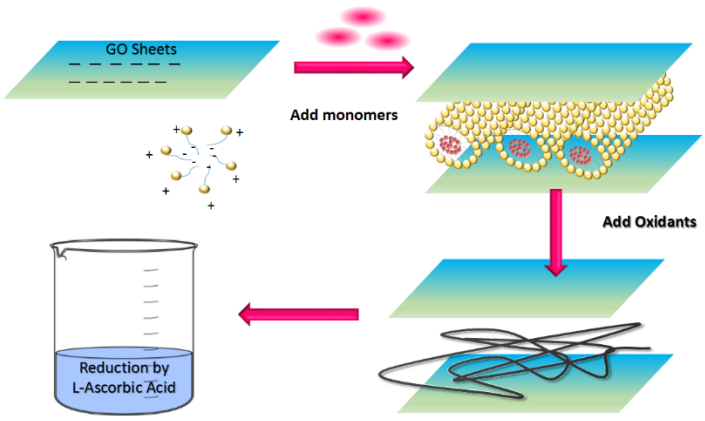

Figure 5.1 The scheme shows the one-step synthesis mechanism of reduced graphene oxide/polypyrrole fibre composites.

The Battery testing is performed using two types of cathode material, including the pure PPy fibre and the RGO/PPy composites. The discharge results proved that RGO/PPy is obviously better cathode material than the pure PPy fibre. The synergism of RGO upon the ORR catalytic efficiency is discussed based on the electrochemistry testing results.

5.2 Experimental

5.2.1 Synthesis of polypyrrole fibre/ graphene composite

5.2.1.1 Materials Preparation

Chemicals used for materials synthesising were all purchased from Sigma Aldrich Australia Pty Ltd. Pyrrole was distilled before polymerization to remove the impurities. 0.109 g (0.3 mmol) cetrimonium bromide (CTAB) was added into 200 mL deoxygenated water to form spherical micelles for wrapping the pyrrole monomers [242]. 0.27 mL (20 mM) pyrrole was added in subsequently. The pyrrole/CTAB suspension was stirred and placed in an ice bath to keep the reaction temperature at 0 ^{o}C. 0.91 g (20 mM) ammonium persulfate was dissolved in 10 mL water and added dropwisely into the pyrrole/CTAB suspension. The mixture was stirred for 24 hours for fully polymerization.

The polypyrrole fibre/graphene composite was synthesised via a one-step polymerization method using pyrrole monomers and graphene oxide aqueous solution as precursors. The graphene oxide was obtained from natural graphite powder by a modified Hummers method referring the exfoliation process developed by Xu *et al* [243]. The concentration of as prepared graphene oxide (GO) solution was quantified as 9.6 mg mL^{-1}. The resulting homogeneous yellow-brown dispersion was stable for several months and ready for future processing. 2 mL GO solution was diluted by 20 mL 0.1 M hydrochloride acid solution and then mixed with the Pyrrole (20mM)/CTAB(1.5mM) mixture. The polymerization conditions was followed as that for synthesising the pure polypyrrole fibers. The resulting powder was filtered and washed by ethanol and deionized water for several times and then heated in 100 mL 2 M ascorbic acid solution at 60 ^{o}C for 5 hours to obtain the reduced graphene oxide (RGO). The GO component in the synthesis precursor is 19.2 mg and Pyrrole is 20 mM = 0.4 mmol = 26.8 mg (since the solution volume is 20 mL), the GO/Py ratio in the precursor is 70%.

5.2.1.2 Battery construction

A silky slurry containing 80% (wt%) active material, 10% Polyvinylidene fluoride (PVDF) and 10% carbon black were prepared by a KK-250S planetary mixer (Mazerustar, japan). The cathode electrodes were fabricated by pasting the composite slurry onto stainless steel mesh confined to a square area of 1 cm^2. Zinc foils were polished, ultrasonic cleaned and cut into 1 cm × 2 cm specimens. The self-made glass

cubes with the fixed width of 1 cm were applied as the battery cases (as showed in Fig.5.2). Both the cathode and anode were attached tightly to each side of the cube and simulated body fluid was injected just before testing. The electrolyte, namely the simulated body fluid (SBF) was prepared referring to the procedure reported by T. kokubo *et al* which has the same ionic composition as human blood plasma[244].

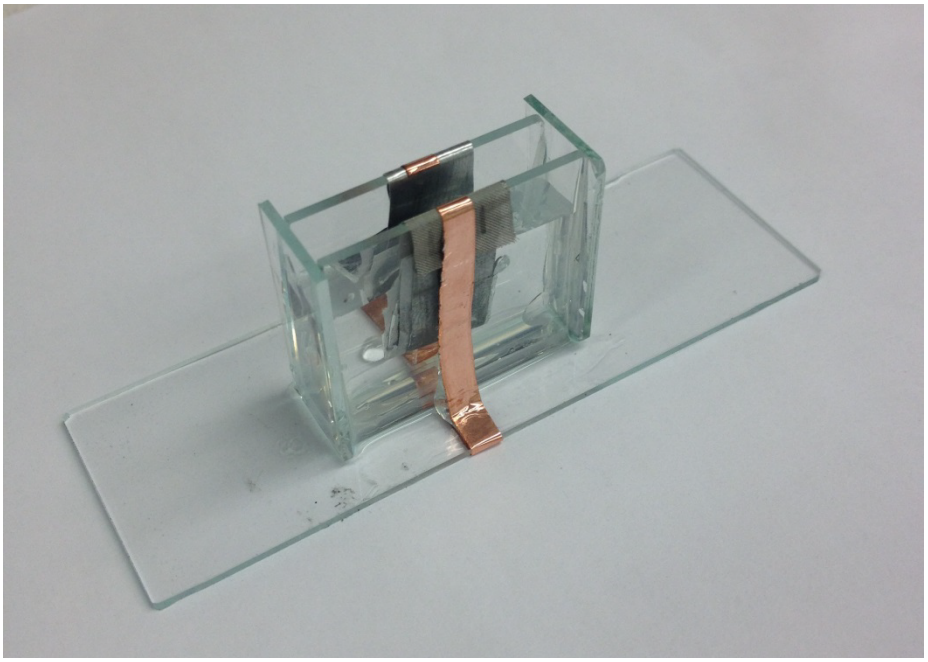

Figure 5.2 The digital photograph of a fully constructed battery

5.2.1.3 Characterizations

The chemical characterization of PPy fiber and PPy fiber/GNs composite were carried out by both Raman spectrum (JOBIN YVON HR800 Confocal Raman system) and X-

ray photoelectron spectroscopy equipped with a SPECS PHOIBOS 100 Analyser and the AlKa radiator as X-ray excitation source. The material morphologies were investigated by field emission electron microscope (JOEL 7500) and transmission electron microscope (JOEL JEM-2011). Specific areas of materials were tested by a Nova 1000 Brunauer-Emmett-Teller (BET) surface area analyse. 20mg powder composite were pressed into a circle plate (1.0cm in diameter) using a compressor equipped with a high pressure vacuum pump for conductivity testing. The thickness of the compressed plate were measured by an electrical calliper. The bulk resistance of the plate were measured by a JANDEL RM3 four point probe instrument and the material conductivity were calculated using the equation $\kappa = L/RS$, where L is the thickness of the film, S is the cross sectional area and R is the bulk resistance. The electrochemistry testing including cyclic voltammetry (CV) and electrochemical impedance spectroscopy (EIS) were performed by a CHI 660 electrochemistry working station. The battery discharge performances were conducted and recorded by a Land^{TM} battery testing system.

5.3 Results and Discussion

5.3.1 Characterizations of cathode materials

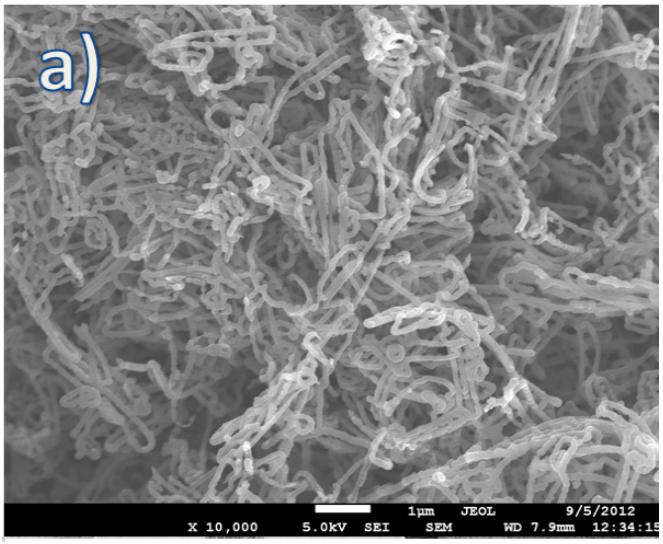

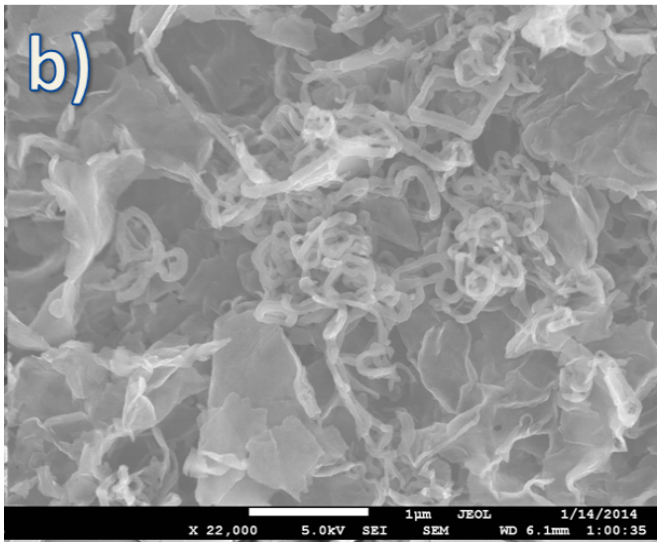

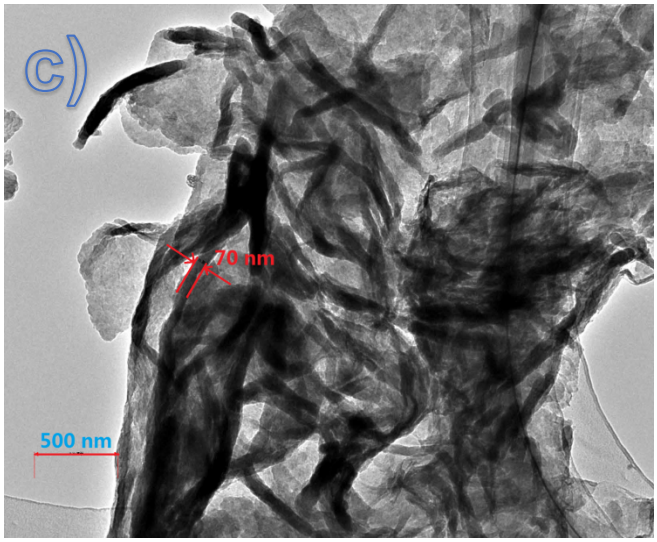

Figure 5.3 Field emission electron scanning microscope (FESEM) image of (a) pure polypyrrole fiber and (b) polypyrrole fiber/ RGO composite; Transmission electron microscope (TEM) images of (c) polypyrrole fiber/ RGO composite

Fig 5.3 (a) shows the morphology of pure polypyrrole fibers synthesized using cationic surfactant CTAB as template. The pyrrole monomers are encapsulated in the cores of cylindrical surfactant micelles and thus the polymer morphology is retained same as that of the micelles. The concentration of CTAB is strictly controlled 4 times of its critical micelle concentration (CMC), under which condition the micelles are wire-like. According Fig 5.3 (a), the polypyrrole fibres are long and uniform with the average thickness of 100nm. Its specific surface area and electric conductivity are measured as 345 m^2 g^{-1} and 76.4S cm^{-1} respectively. After being incorporated with the RGO nano sheets, both the specific surface area and conductivity of the composite are significantly increased to 561 m g^{-1} and 141 S cm^{-1}, respectively. Both the large surface area and high electric conductivity are crucial for the cathode material to achieve high

electrochemical catalytic activity. According to Fig 5.3 (b) the polypyrrole fibres are interwoven between graphene layers with the relatively smaller average thickness which is around 70nm. Such structure is much clearer under the observation of TEM image as showed in Fig 5.3 (c). The long and tangled polypyrrole fibres distribute on the RGO nano sheets evenly and the RGO nano sheets are coated with a sheer layer of polypyrrole. The finer polypyrrole fibres and large-scaled two-dimensional coated graphene sheets together create a larger specific surfaces areas than the pure polypyrrole nano fibres.

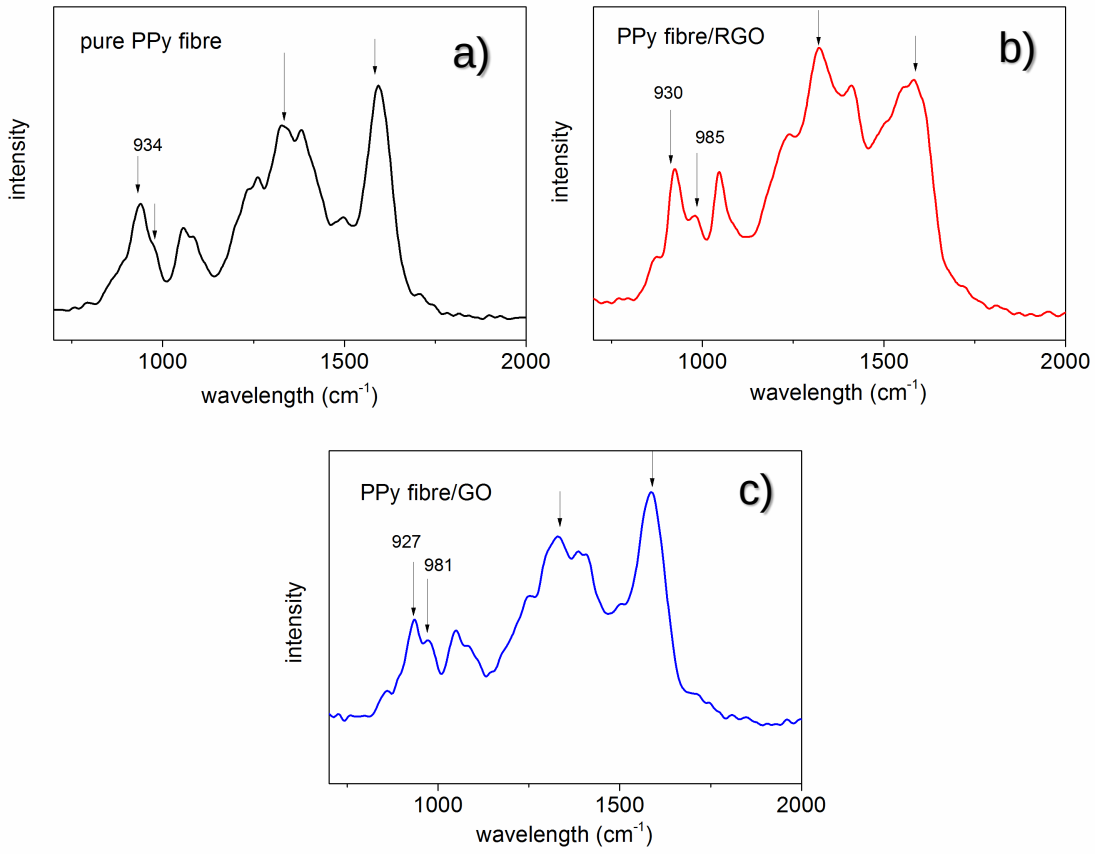

Figure 5.4 Raman spectrums of (a) pure PPy fiber (b) PPy fibre/RGO composite and (c) PPy fibre/GO composite

To characterize the chemical structure transformations of the composites after reduction and the interactions between the polypyrrole fibres and the graphene nano sheets, Raman spectrums were performed on each samples as showed in Fig. 4 (a-c). All of the samples displayed characteristic peaks assigned to the doped polypyrrole structures[225]. The peak representing the C-H in plane deformation appears at 934cm^{-1} for pure polypyrrole fibers which shifted to 930cm^{-1} for PPy/GO and 927cm^{-1} for PPy/RGO. Meanwhile, small shoulder peaks adjacent to the 930cm^{-1} band are observed both the PPy/RGO (985cm^{-1}) and PPy/GO (981cm^{-1}). Such peaks are related to the reduced state of the PPy chain[226], suggesting incomplete oxidizing process. Therefore, the PPy of both the composites are not fully oxidized which are composed of both the cation doped and dication doped states. This type of shoulder peak is not distinctive in the spectrum of the pure PPy fibre, indicating that the pure PPy fibre are fully oxidised and mostly dication doped. It reveals that the function groups on the graphene basal plane are associated to the nitrogenous functional groups of PPy backbone via the same doping mechanism as that of Cl^-, however, with slightly less efficiency than the latter[245]. The graphene basal structure has two well documented characteristic peaks including D-band at 1340 cm^{-1} and a broad G-band at 1580 cm^{-1}. These two peaks correspond to the first order scattering of the E2g mode of 2D graphite lattice and the in-plane bond stretching motion of the carbon Sp2 atoms respectively[246]. These two band regions are boarded for both the PPy/GO and PPy/RGO composite as they overlapped with the ring stretching and C-C backbone stretching (1325cm^{-1}) band regions of polypyrrole backbones (1600cm^{-1})， which also provides evidence for strong chemical interactions

between graphene and polypyrrole. The intensity ratio of D band versus G band is significantly higher for PPy/RGO composite comparing to that of PPy/GO composite. This is mainly due to the emergence of structural defects after the removal of large amounts of oxygen functional groups[177, 247]. It is notable that ascorbic acid also has slightly reduced the polypyrrole causing the split of the band at 1580cm^{-1} region. However, the reduction of polypyrrole has almost no negative effects on the electric conductivity of the PPy/RGO composite as the high electric conductivity of the composite is mainly contributed by the fast electron transfer rate of reduced graphene oxide.

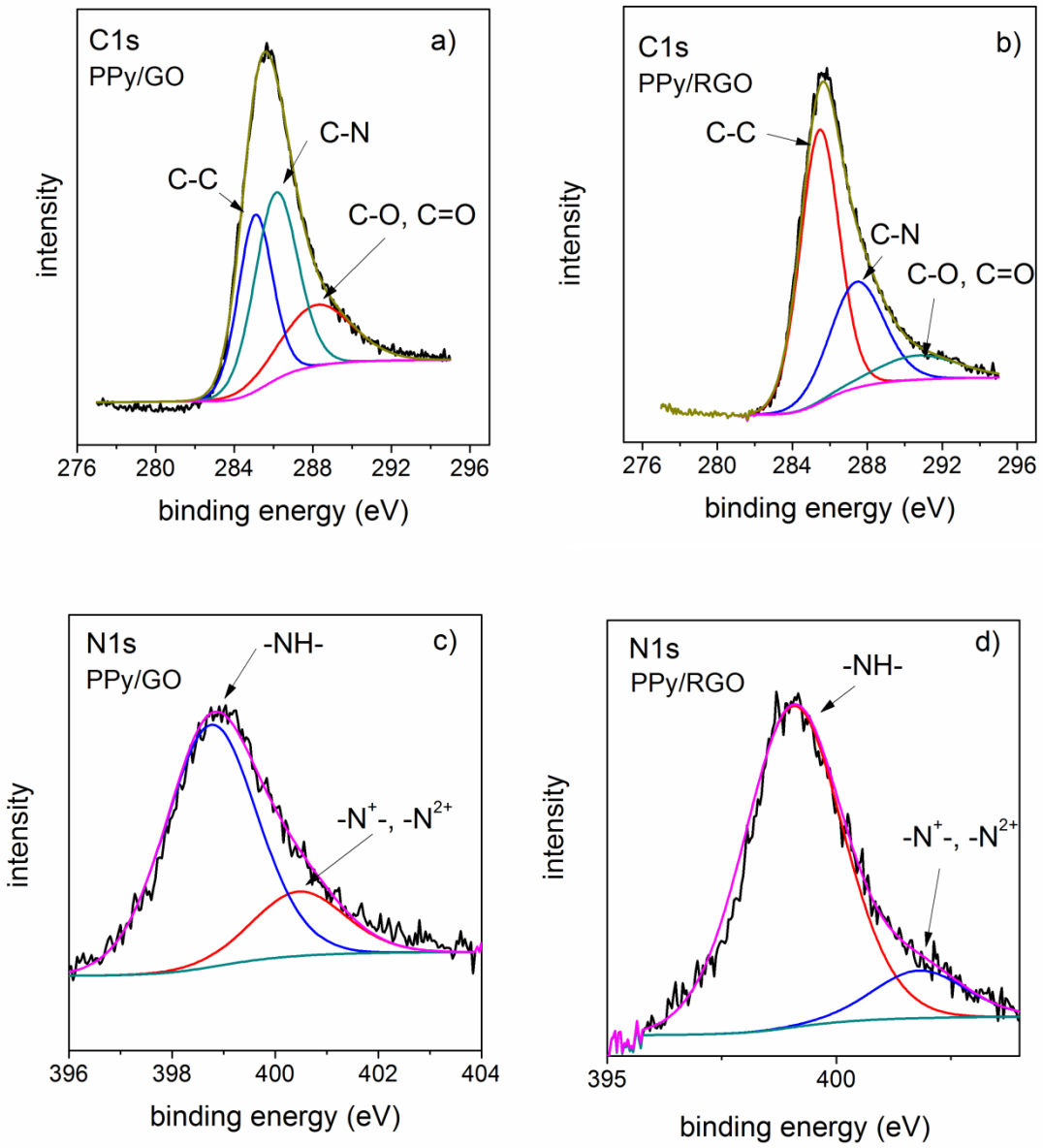

Figure 5.5 De-convoluted C1s and N1s X-ray photoelectron spectroscopy (XPS) spectra of PPy fiber/GO composite (a, c) and PPy fiber/RGO composite (b, d)

The reduction effect of ascorbic acid on PPy/RGO composite was further investigated by X-ray photoelectron spectroscopy (XPS) as well. The peak deconvolution and

fittings are carried out using the Gaussian-Lorantzian shape peaks based on the Shirley background correction. The peak at 284.5ev for C1s spectra represents the non-oxygenated C-C bonding, which is obviously intensified after reduction. The board peak at 288.4ev can be assigned to the carbon oxygen bonding including C-O and C=O[248]. This peak is significantly weakened upon reduction. The transformations of these two peaks reveal that the reduction process is efficient. The de-convoluted N1s spectra of both the composites exhibit two distinct peaks. The dominating peaks at 399.0ev represent the neutral amine nitrogen structure (-NH-) and the tail peaks at 401ev is related to the positively charged nitrogen[249, 250]. The intensity of the high-BE tail peak is weakened upon reduction, indicating the ascorbic acid also has slightly reduced the doped polypyrrole which is in correspondence with the Raman spectra analysis.

5.3.2 Electrochemistry testing

Fig 5.6 (a, b) shows the discharge performances of batteries with two types of electrolyte being tested under different discharge current rates. Each testing session with a certain discharge current density was pre-set as 300 minutes. It is obvious that the batteries with PPy/RGO cathodes reveal significantly better discharge performances in both of the electrolyte. Generally, they display higher and more stable discharge plateaus and less potential decline under any discharge current rates. On the contrary, the batteries composed of pure PPy fibre cathodes suffer from almost linearly potential drops. The embedded curves showing the dependence of energy density upon discharge

current rates indicate the superiority of the PPy/GR cathode from another aspect. The energy density is calculated based on the equation below,

$$E=1/2\ It\ V^2$$

Where I is the discharge current density, t is the discharge time and V is the plateau voltage. The batteries with PPy/RGO cathode display the highest energy density of up to 264 mWh g^{-1} in PBS buffer solution and 210 mWh g^{-1} in SBF while this value for batteries with pure PPy fiber cathodes are only 139 mWh g^{-1} and 129 mWh g^{-1} respectively.

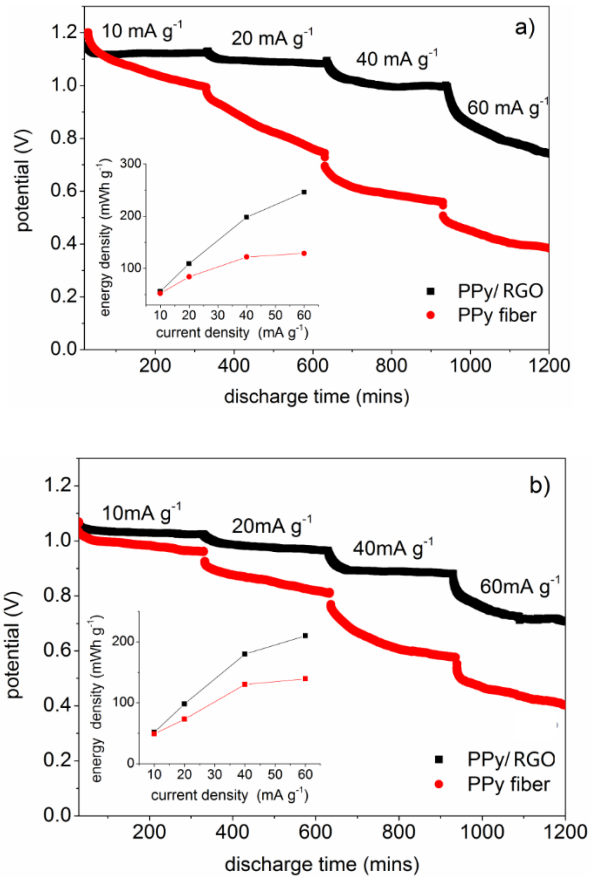

Figure 5.6 the discharge curves of batteries composed of both Pure PPy fibre and PPy/RGO electrodes being tested in (a) the 0.2M PBS solution and (b) SBF solution.

The effect of different electrolytes on battery discharge performances is relatively less distinctive. However, it is notable that the open circuit potentials of batteries with both types of cathode materials are slightly higher when tested in PBS. Meanwhile, in PBS electrolyte, the batteries generally possess higher discharge plateaus and present higher energy densities. On the other side, the discharge potential drops are severer in PBS solution, especially for the battery with pure PPy fibre cathodes.

In summary, these two key factors including the cathode materials and electrolyte are decisive for the battery discharge performances. The role of the cathode material can generally be explained as the oxygen reduction catalyst which catalyst the oxygen to be reduced to hydroxyl ions for zinc oxidation throughout the discharge process. The cathode materials achieve their catalysis effects via its reversible redox reaction with oxygen. Therefore the catalytic efficiency of the cathode materials are mainly related to their redox reversibility and activities.

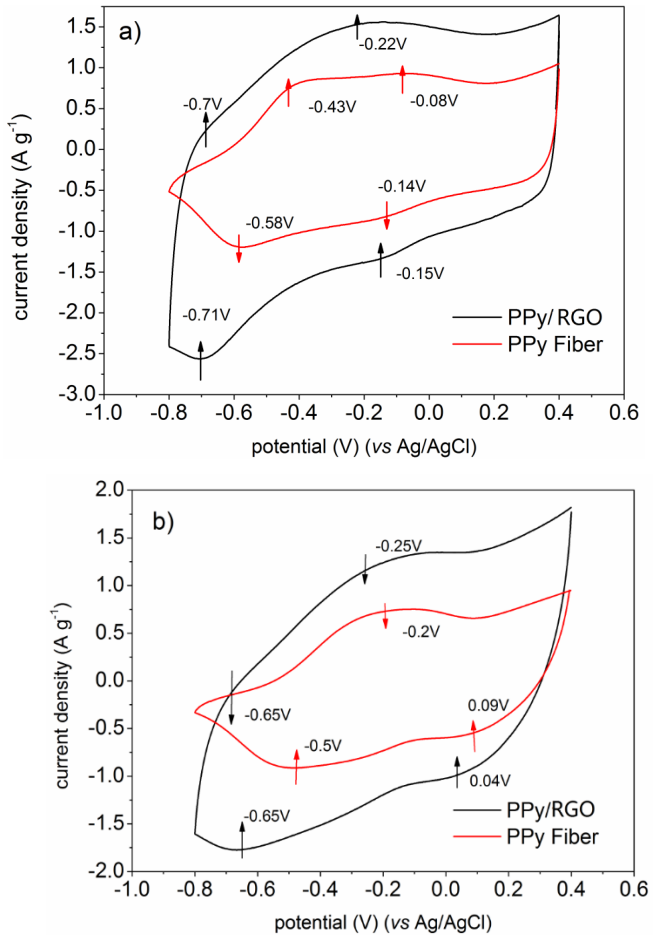

Figure 5.7 The cyclic voltammograms curves of PPy/RGO and Pure PPy fibre cathodes in (a) 0.2M PBS solution and (b) SBF (scan rate= 5mV s^{-1})

To investigate the redox activities of the cathode materials, cyclic voltammetry were conducted on both the Pure PPy fibre and PPy/RGO composites in PBS solution and SBF respectively, as showed in Fig 5.7 (a, b). It is very obvious in both of the CV curves in PBS and SBF that the redox capacitance of PPy/RGO composite is significantly higher than pure PPy fibre due to their larger current response. This phenomenon can be ascribed to the enhanced electric conductivity of PPy/RGO composite. In PBS

electrolyte, the pure PPy fibre as two board oxidation peaks at -0.43V and –0.08V and two reduction peaks at -0.58 V and -0.14V. Those peaks are all shifted slightly left for PPy/GR composite, as labelled in Fig 5.7 (a). These two redox pairs can be assigned to the cation expulsion and insertion process of the polypyrrole matrix, which can be demonstrated by the equations below,

$$(PPy)_n^0 A_L^- C_s^+ - e \leftrightarrow (PPy)_n^+ A_L^- + C_s^+ \quad (1)$$

$$(PPy)_n^+ A_L^- C_s^+ + e \leftrightarrow (PPy)_n^0 A_L^- + C_s^+ \quad (2)^{251}$$

Where the A_L- represents large sized anions ($H_3PO_4^-$, HPO_4^{2-}*et al*) and C_s^- means small sized cations (Na^+ ,K^+ *et al*). It is notable that the voltage difference between the second reduction/oxidation peak pair is narrower for PPy/RGO composite, suggesting better redox reversibility of the material. Therefore, the batteries with PPy/RGO cathodes displayed higher and more stable discharge plateaus mainly attributed by its better oxygen catalytic efficiency originated from its high redox reversibility and higher redox capacitance.

On the other side, the nature of the electrolyte can affect the redox capability of the cathode materials and consequently determine their catalytic efficiency. In PBS solution, the contour profiles of CV curves are near rectangular shape and higher current response than that of the SBF which both represents large capacitance. However, the CV curves in SBF generally display spindle like shapes with significant reduce in capacitance. This is mainly due to the presence of large molecular such as HPEPs which can block the charge transfer channels on the PPy matrix[252]. Due to this

effect, the open circuit potentials of batteries with SBF electrolyte are significantly lower and the charge potential drops are much severer.

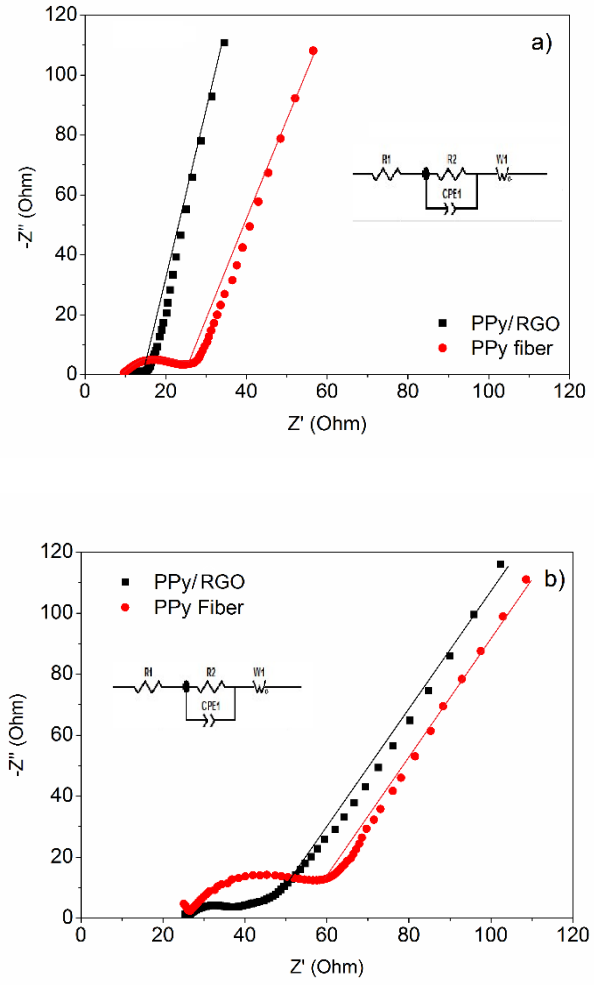

Figure 5.8 EIS spectra and the simulated spectra (lines) of PPy/RGO and pure PPy fiber tested in (a) 0.2 M PBS solution and (b) SBF solution. (Inset, equivalent circuits)

To further investigate the interfacial electrochemical behaviours of the cathodes in these two types of electrolyte, electrochemistry impedance spectrum (EIS) were tested after 3 hours discharge. The Nyquist plots reflecting the relationship of real impedance Z' versus imagery impedance Z'' are showed in Fig. 5.8 (a,b).

Table 5.1 the fitting values of the equivalent circuit elements

	R1	R2	Cp1	W1
Ppy fibre/PBS	9.63	8.64	0.76	15.4
Ppy RGO/PBS	9.48	3.95	0.69	4.86
Ppy fibre/SBF	24.52	20.6	0.77	40.1
Ppy RGO/SBF	24.41	8.59	0.68	42.3

The Nyquist diagrams mainly include a semicircle region lying on the real axis followed by a straight line. The semicircle observed at higher frequencies usually corresponds to the faradic charge carrier transfer process, and its radius can reflect the charge transfer resistance of the redox processes, whereas the linear part at the lower frequencies range represents the diffusion-controlled electrode process[253]. The EIS spectra were simulated using the equivalent circuit as shown in Figure 9 inset. It was composed of four major components, including bulk solution resistance R1, internal resistance R2, electron double layer capacitance C1 and the Warburg diffusion element W1. The values of each elements were calculated and listed in Table.2. It is obvious that in both electrolytes, the PPy/RGO electrodes present lower charge transfer resistance indicating the electrochemical process is more active for battery with PPy/RGO electrode, which can also explain its superior discharge performances. Meanwhile, the nature of electrolyte can affect the electrochemical processes by affecting the diffusion process and faradic charge carrier transfer process spontaneously. The biases of Nyquist plots at low frequency region are generally larger in PBS solution for both types of the electrodes.

The solution resistance which is generally recognized as the value of the real impedance axis at OCV, is 14.7 Ω for PBS solution and 26.4Ω for SBF respectively[254]. These results reveal that the ion diffusion process is generally faster in PBS solution due to the lower solution resistance. The low ion motilities can decrease the ion exchange rate at the interfaces of both the anode and cathode and consequently deteriorate the catalytic efficiency of the cathode and simultaneously the ion dissolution rate of the zinc anode. This can also explain why the batteries with SBF electrolyte have lower open circuit potential and lower capacities.

5.4 Conclusion

PPy fiber/RGO with high conductivity, large specific surface area are successfully synthesized via a simple one-step chemical polymerization method. Batteries constructed with such material have stable energy outputs at both the low and high current density. It is proved that such material is a highly effective oxygen reduction catalyst originated from its excellent redox reversibility and capacitance. Therefore such composite can work as an ideal cathode candidate for bio-compatible Zinc/polymer battery. The batteries using SBF and PBS electrolyte have different discharge performances due to nature of the electrolytes. SBF contains large organic cations which can induce the increase of solution resistance of the electrolyte and consequently retard the interface reaction at both the anode side and cathode side. Batteries with PPy/GR cathode achieved the energy densities of 264 mWh g^{-1} in PBS

and 210 mWh g^{-1} in SBF, suggesting its feasibility as a power sources for a board range of implantable micro-medical devices.

Chapter 6

Mechanically strong high performance layered polypyrrole nano fiber/graphene film for flexible solid state supercapacitor

6.1 Introduction

Over the last decade, low cost, efficient and miniature energy storage devices became key research directions worldwide due to the fast expanding market of portable electronics. Future electronics such as roll-up display, electronic paper, stretchable integrated circuits, and wearable systems for personal multimedia or medical devices all need reliable energy supplies with good flexibility[255, 256]. Supercapacitors generally have moderate energy density ranging between 0.1 to 10 Wh Kg^{-1} which usually exhibit high-energy-storage efficiencies and excellent cycling stabilities[257]. Therefore, high performance flexible solid state supercapacitors are capable of being applied as one of the promising power sources for various types of flexible devices. Furthermore, solid states supercapacitors have also been considered as a possible power supply for implantable bio-medical devices as discussed in chapter 1.

Ever since the discovery of graphene, many research works has been carried out to develop supercapacitors using graphene or graphene based composites as the electrode materials[164]. Graphene has the interesting one atom thick single layer hexagonal lattice structure which brings out many excellent physical and chemical properties making it a versatile material for many applications[160, 164]. It is investigated as the electrode materials for supercapacitors mainly due to its fast charge carrier transportation[162, 258], chemical stability in aqueous solutions[259] and high specific surface areas[260]. The specific capacity of the exfoliated graphene nano sheets is superior to most of the carbon materials including carbon nanotubes, which is 2620 m^2/g theoretically[160 260-263]. It has been evidenced that the average specific capacity of supercapacitors with graphene based electrodes in both organic and aqueous electrolyte are all above 200F g^{-1} [261]. Previous work also showed that high quality graphene based capacitor exhibits a specific energy density of 85.6 Wh kg^{-1} at room temperature[264]. Meanwhile, graphene nano sheets can be easily made into mechanically strong freestanding papers various methods, which is suitable for making flexible solid state supercapacitors[265-267].

As a derivate of carbon material, supercapacitors with graphene electrodes are generally electrical double layer capacitors (EDLCs) which gain capacity by quick electrostatic charge carrier storage. For EDLCs, specific surface area of electrode is critical since the charge carriers adsorption occurs on the interface between electrolyte and electrode[257, 268]. However, the specific area of flexible graphene paper can be significantly reduced due to the restack of graphene nano sheets. Meanwhile, the capacities of EDLCs are limited comparing to most of the pseudocapacitors composed of conductive polymers or metal oxide electrodes[269, 270]. The pseudocapacitors obtain

high capacities by the addition of reversible electrochemical reactions to the double layer capacitance, but their cycling stabilities are normally poor due to the change of structural conformation with the repeated ion exchange processes[257]. To achieve high capacity without deteriorating the cycling life, carbon materials including graphene nano sheets are usually incorporated with conductive polymers or metal oxide to create the pseudo-EDLCs pair.

In this chapter, a layered structure of polypyrrole (PPy) nano fibres and graphene nano sheets was produced by a simple method. Polypyrrole are inexpensive and can enhance the capacity effectively[271-274]. Nano structured polypyrrole synthesised using the surfactant micelles templates is ideal electrode materials since it is inexpensive, highly conductive and of large specific surface areas[242, 275]. The restack of graphene nano sheets were significantly mitigated due to the evenly distributed polypyrrole nano fibres in between graphene nano sheets. A gel type electrolyte, phosphate acid (H_3PO_4) infused Polyvinyl alcohol (PVA) is applied to make integrated flexible capacitors. Such capacitors demonstrates high galvanostatic discharge specific capacitance of 345 F g^{-1}.

6.2 Experimental

6.2.1 Preparation of PPy nano fibres and Graphene oxide (GO) dispersion

Chemicals used for synthesising polypyrrole nano fibres including pyrrole monomers, ammonium persulfate (APS) and cetrimonium bromide (CTAB) were all purchased from Sigma Aldrich Australia Pty Ltd. Pyrrole was distilled before polymerization to remove the impurities. 0.109g (0.3mmol) CTAB was added into 200 mL deoxygenated water to form spherical micelles for wrapping the pyrrole monomers [242]. 0.27 mL (20mM) pyrrole was added in subsequently. The pyrrole/CTAB suspension was stirred and placed in an ice bath to keep the temperature at 0^{o}C. 0.91g (20mM) Ammonium persulfate was dissolved in 10 mL water and added dropwisely into the pyrrole/CTAB suspension. The mixture was stirred for 24 hours for fully polymerization. Graphene oxide was synthesised from natural graphite powder by a modified Hummers method referring the exfoliation process developed by Xu *et al* [243]. The concentration of as prepared graphene oxide (GO) solution was quantified as 9.6mg mL^{-1}. The resulting homogeneous yellow-brown dispersion was stable for several months and ready for future processing.

6.2.2 Preparation and reduction of GO and PPy fibre/GO papers

Both the thin PPy fibre/GO paper and GO paper were prepared by vacuum filtration method using polycarbonate filter membranes. 2 mL GO dispersion was diluted by 20 mL water and vacuum filtered to produce a thin and smooth GO film. To make PPy fibre/GO paper, 10mg PPy fibre was added into 20 mL water and ultrasonicated for 30 seconds. 1 mL GO is mixed with the PPy fibre dispersion and filtered. The films are vacuum dried at 50^{o}C for 12 hours. The GO and PPy fibre/GO films were reduced by immersing in Hydriodic acid (HI, 47%) for 20 minutes at 4^{o}C[175].The films were washed by water and ethanol to remove the acid residues.

6.2.3 Construction of capacitor cells

The procedures to fabricate the PVA/ H_3PO_4 gel and the supercapacitor device are similar to what we previously reported[276]. Briefly, 10g PVA was dissolved in 100 mL \water at 90^{o}C. The PVA: H_3PO_4 ratio was kept as 9:1. Before constructing the cell, the films were all immersed in the electrolyte overnight and dried afterwards. The gel electrolyte was spread on top of the dried films uniformly. Another piece of film was put on top of the semi-dried electrolyte layer and pressed to get a good attachment. Stainless steel mesh was cut into two pieces of wires and jointed at the back of the films by highly conductive silver paste.

6.2.4 Characterization and Cell testing

Topographic heights of graphene oxide nano sheets were measured by the atom force microscope (Asylum Research, MFP-3D). Bright field and high resolution transmission electron microscope (TEM) images were taken by a JOEL JEM-2011 microscope with 120KV accelerating voltage. Morphologies of the as prepared PPy fibre and PPy fibre/GR films were observed with a field emission scanning electron microscope (FESEM, JOEL 7500). The Raman measurements were performed with a JOBIN YVON HR800 Confocal Raman system with 632.8 nm diode laser excitation on a 300 lines/mm grating at room temperature. X-ray photoelectron spectroscopy (XPS) was performed a XPS system equipped with a hemispherical energy PHOIBOS 100/150 analyser. The strain-stress curves of pure GO and GO/PPy fibre films were tested before and after being reduced by hydriodic acid using a shimadzu EZ mechanical tester. Electrochemical testing including impedance spectroscopy (EIS), cyclic voltammetry (CV) and cell charge/discharge performances were carried out by a CH Instrument (CHI 660B).

6.3 Results and discussions

6.3.1 Morphologies

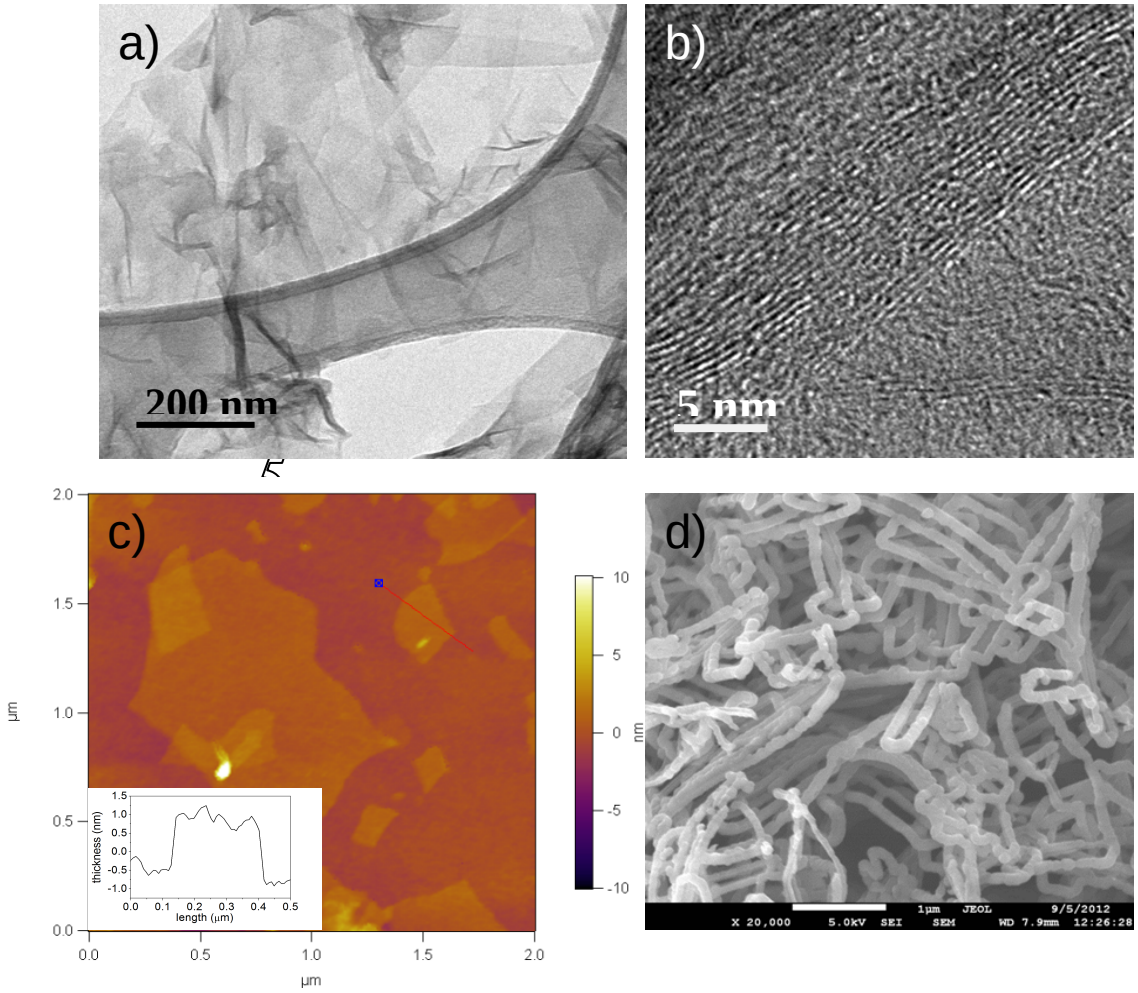

Figure 6.1 (a) Bright field transmission electron microscope image of exfoliated graphene oxide sheets. (b) High resolution TEM image of exfoliated graphene oxide sheets along the profiles (c) AMF image of exfoliated graphene oxide layers (d) FESEM image of chemically synthesised PPy fibre

Topological height and surface dimensions of as prepared graphene oxide sheets were measured AFM and TEM respectively. Graphene oxide nano sheets with large surface dimensions are observed from bright field TEM image (Fig 6.1(a)). The graphene sheets are of sheer veil like morphology which ripples slightly producing wrinkles at the overlapped areas. The thickness of graphene oxide sheets is measured as 1.5nm by AFM as showed in Fig 6.1 (c). Such thickness can be assigned to 2-3 layers of pristine graphene oxide sheets, representing the complete exfoliation of graphite oxide[277]. Due to the presence of CTAB, the pyrrole monomers can be encapsulated in the hydrophobic cores of surfactant micelles where they polymerized and thus keep the polymer morphology same as that of the micelles. The average thickness of polypyrrole nano fibres is about 100nm as showed in Fig .1 (d). The long fibres are long and uniform in diameters which can easily interwoven together producing a porous network structure.

Fig 6.2 showed the morphologies of pure RGO film and RGO/ PPy fibre films from different views. Fig 6.2 (a) and (b) are the cross section images of the PPy fibre/RGO film. The interspaces between graphene layers are produced by the evenly distributed PPy fibres, which significantly reduce the stacking of RGO layers comparing to the pure RGO films as showed in Fig 6.2 (e). After adding 50% (WT%) PPy fibre, it is found the film thickness is enlarged 7 times compared with that of the pure RGO film, as showed in Fig 6.2 (c) and (f). The top view of the RGO/PPy fibre film is showed in Fig 6.2 (d). The polypyrrole fibres are warped by the RGO sheets producing enlarged surface areas with large numbers of concaves and convexities. Generally, the GO film assembled by vacuum filtration can induce stacking of graphene oxide sheets. The

polypyrrole fibres have the function of spacing the RGO layers, creating a loose layered structure with pores and higher surface area.

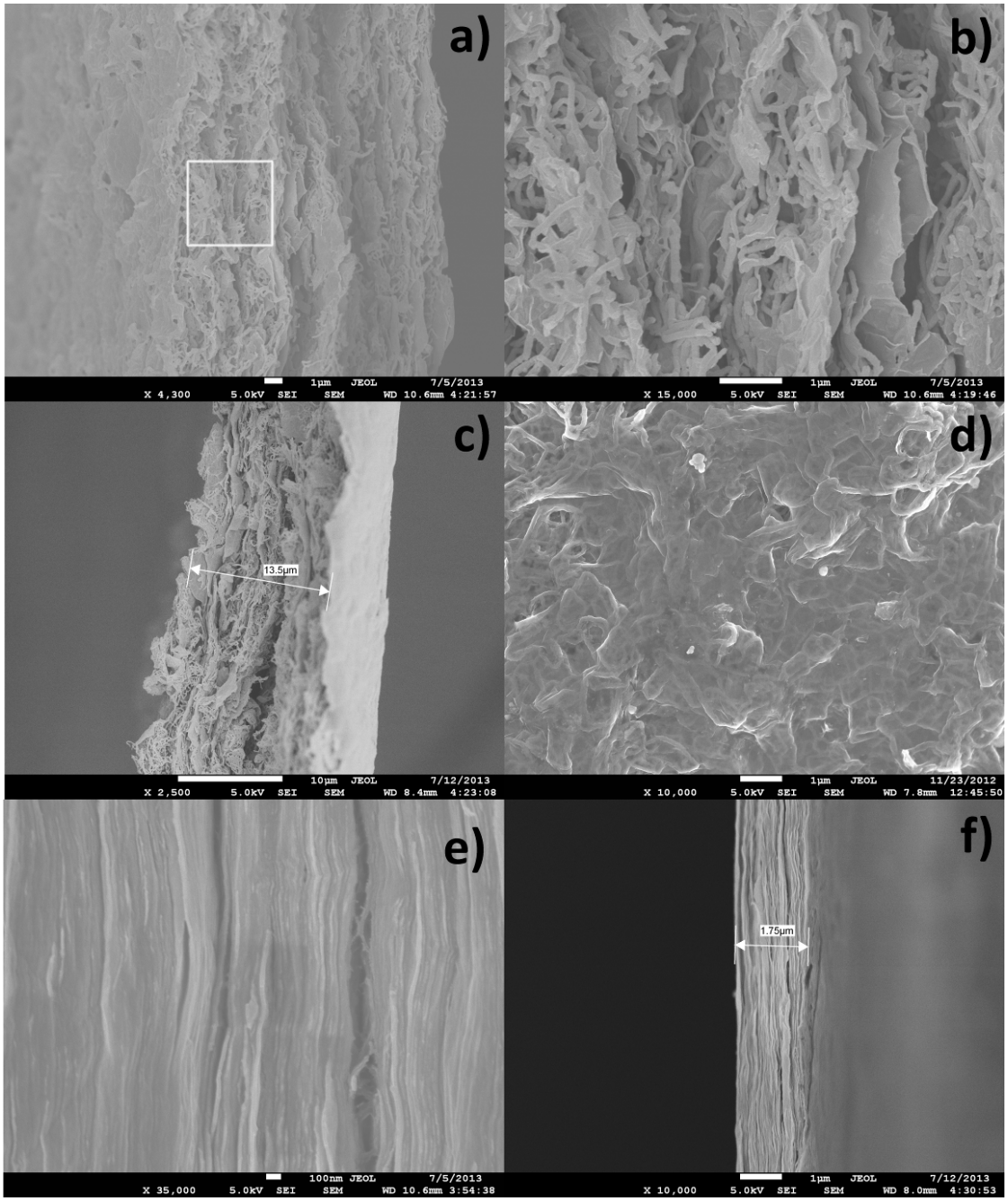

Figure 6.2 FESEM images showed (a) cross section of PPy fibre/GR film (b) localized cross section of the area which defined by the pane in (a). (c) thickness of PPy fibre/GR film. (d) surface of PPy fibre/GR film. (e) cross section of pure GR film (f) thickness of pure GR film. (GR= reduced graphene oxide)

6.3.2 Mechanical properties and conductivity

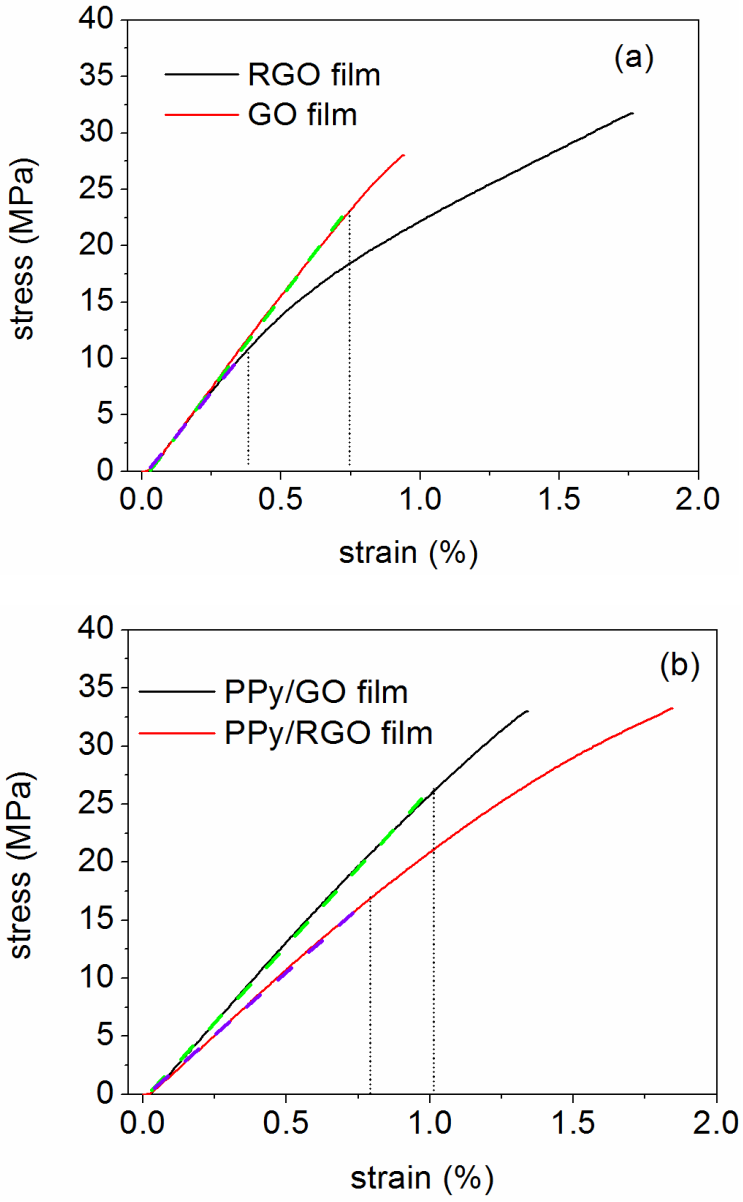

Figure 6.3 Strain stress curves of GO film (a) and PPy/GO film before and after reduction by HI.

According to the cross section image of RGO films, it can be seen that the structure of ordered layer of RGO sheets retained well after being reduced by HI acid [175]. HI is a residue free strong reducing agent capable of removing the carbonyl and carboxyl groups fast and efficiently without gas release. Thus, both the structures and mechanical properties of the films can be retained after reduction. The strain stress curves of RGO film and PPy/RGO film (Fig 6.3) both composed of a typical "washboard" pattern with the linear elastic regions and the self-reinforcing region[278]. The young's modulus did not reduce significantly upon chemical reduction, which are 15% for GO film, and 19% for PPy/GO film respectively, indicating that the elasticity of both films are retained well after being reduced by HI. The embedded PPy nano fibres did not deteriorate the elasticity though they significantly reduced the compactness of pure GO/RGO films according to the SEM images. On the other side, the increase of both the fracture strength and maximum elongation for pure GO film increased more significantly than the Ppy/GO film upon reduction according to the data calculated and illustrated in table 6.1.

Table 6.1 Conductivities and Mechanical properties of different type of flexible films

Types of films	Conductivity (S cm^{-1})	Young's modulus (GPa)	Ultimate strength (to fracture/MPa)
PPy/GO	3.80×10^{-2}	2.6	34.9
PPy/RGO	142.08	2.1	35.0
Pure GO	1.11×10^{-2}	3.2	27.6
Pure RGO	164.92	2.7	32.5

The removal of oxygen functionalities induced the decrease of carbon lattice interlayer distances and thus enhanced the interactions among RGO sheets. Such phenomenon is also notable but less significant for PPy fibre/GO film due to the presence of interlayered PPy fibre network structures. The conductivity of both PPy/GO and pure GO film increases significantly after reduction which are correlated to the increase of C/O ratios as showed in table.1 [173, 279]. The conductivity of pure RGO film is up to 164.92 S cm^{-1}, suggesting the high reduction efficiency of HI.

6.3.3 Chemical characterizations

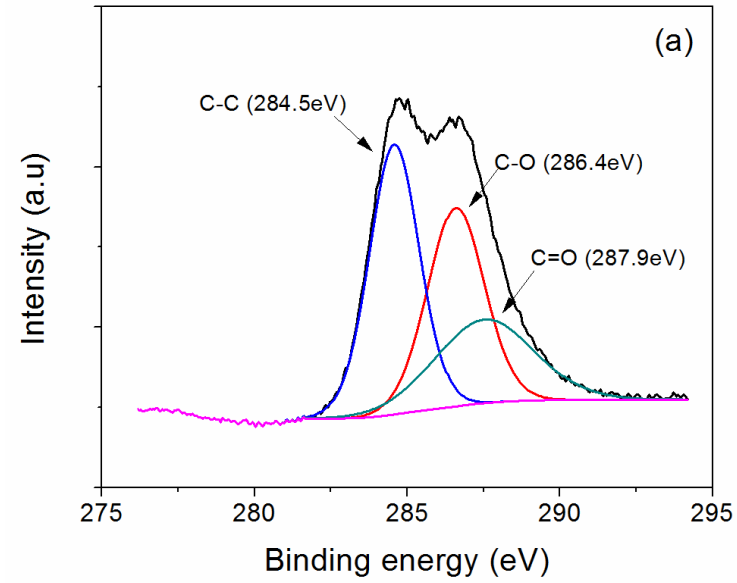

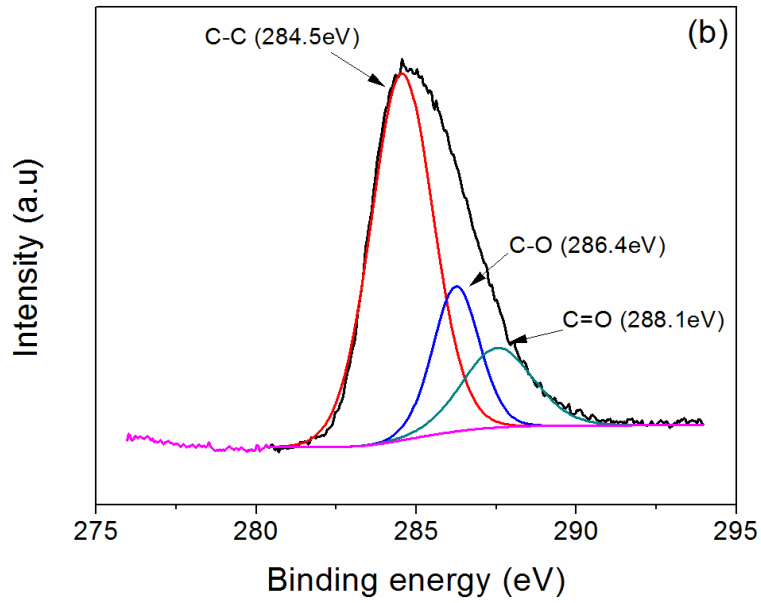

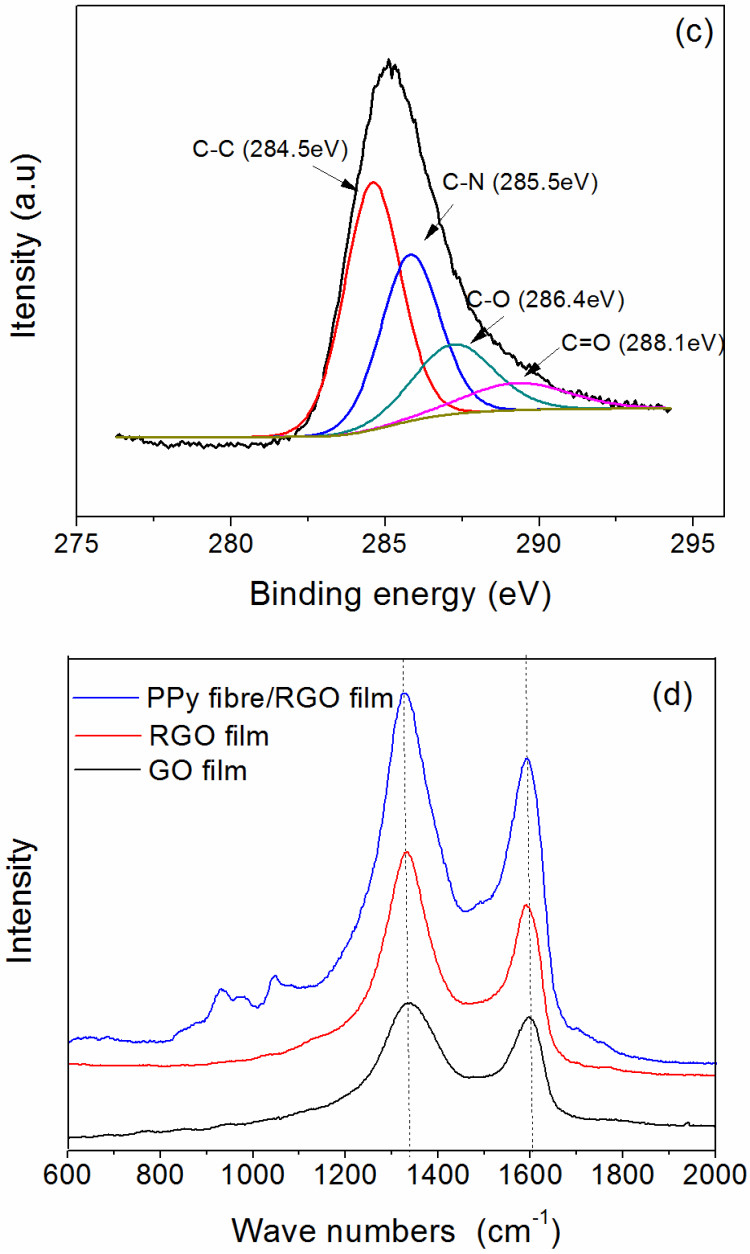

Figure 6.4 De-convoluted XPS C1s spectra of (a) Pure GO film (b) HI reduced RGO film (c) HI reduced PPy fibre/RGO film and (d) Raman Spectra of all these three types of films distinguished by different colours (blue for PPy fibre/RGO film, red for RGO film and black for GO film)

To further investigate the reduction effect of HI on different types of films, X-ray photoelectron spectroscopy is performed and analysed (Fig 6.4 (a-c)). Curve fittings of the spectrums are carried out using the Gaussian-Lorantzian shape peaks based on the Shirley background correction. The peaks representing the C-C bonding at 284.5 ev show dominating intensity in both the spectra of RGO film and PPy fibre/RGO film[172, 280]. The pure GO film has two strong peaks of oxygen functionalities including C-O bonding at 286.4 eV and C=O bonding at 287.9 eV which are significantly weakened after reduction. The C/O ratio of pure GO film is 2.76 which rises to 7.76 after reduction. This suggests that the removal of oxygen functionalities is efficient and successful. The spectrum of PPy fibre/RGO film contains the peak of C-N bonding with the binding energy of 285.5 eV and the nitrogen percentage of which are 11.82[281]. The bonding information is also investigated by Raman spectrum as showed in Fig 6.4(d). The Raman spectrum of graphene oxide film displays the D-band at 1340 cm^{-1} and a broad G-band at 1580 cm^{-1}, which corresponds to the first order scattering of the E2g mode of graphite lattice and the in-plane bond stretching motion of the carbon sp^2 atoms respectively[282]. The D peak is mainly attributed to the structural imperfections on the carbon basal plane. After reduction, the intensity ratio between D band and G band (I_D/I_G) is significantly increased for the pure GO film. This is mainly due to the decrease in the average size of the sp^2 domains upon reduction of the exfoliated GO, which consequently produces more imperfections because of the emerging of enormous edges and wrinkles belonging to the fragmentized carbon sp^2 domains[283, 284].

The Raman spectrum of PPy fiber/RGO film also displayed characteristic peaks related to the polypyrrole structures. The peak at 940cm^{-1} demonstrates the C-H out of plane

deformation while the peak at 998 cm^{-1} can be assigned to the pyrrole ring deformation. The peak at 1045cm^{-1} corresponds to the C-H in plane deformation which has a small shoulder peak at 1049cm^{-1} related to the anion dopants[225, 227].

6.3.4 Electrochemical performances

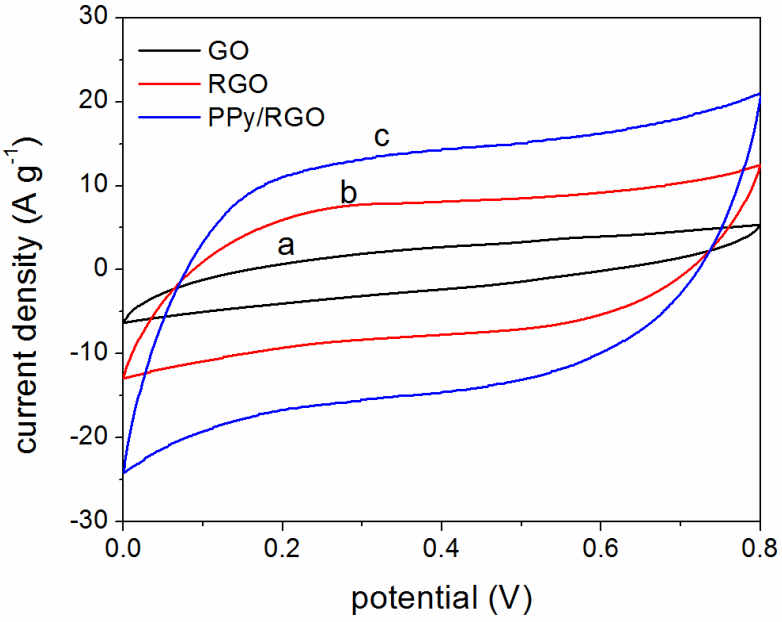

Figure 6.5 Cyclic voltammetry curves of capacitors using H_3PO_4/PVA gel as electrolyte with different flexible electrodes at the scan rate of 50mV S^{-1}, (a) GO film (b) RGO film (c) PPy fibre/RGO film

Fig 6.5 shows the CV curves of the flexible supercapacitors constructed with these film electrodes and PVA/H_3PO_4 gel electrolyte at the scan rate of 50mV S^{-1}. It is obvious that the capacitance of pure RGO film is significantly larger than the pure GO film,

which can be ascribed to its enhanced electronic conductivity of the film electrodes. The capacitor with PPy fibre/RGO film electrodes generally displayed the largest near rectangular CV curve showing the ideal capacitive behaviour, suggesting the excellent ionic and electronic transportation of the electrodes. It is worth nothing that although the conductivity of PPy/RGO electrode is slightly lower than the pure RGO film, its capacitance is still much higher than the other two types. Its high capacitance can be mainly ascribed to two key factors including its porous structure and the contribution by the faradaic pseudocapacitance of polypyrrole fibres. The porous structure of PPy fiber/RGO film provides larger interface between the electrolyte and the film electrodes and therefore enhances the accessibility for electron storage and transportation.

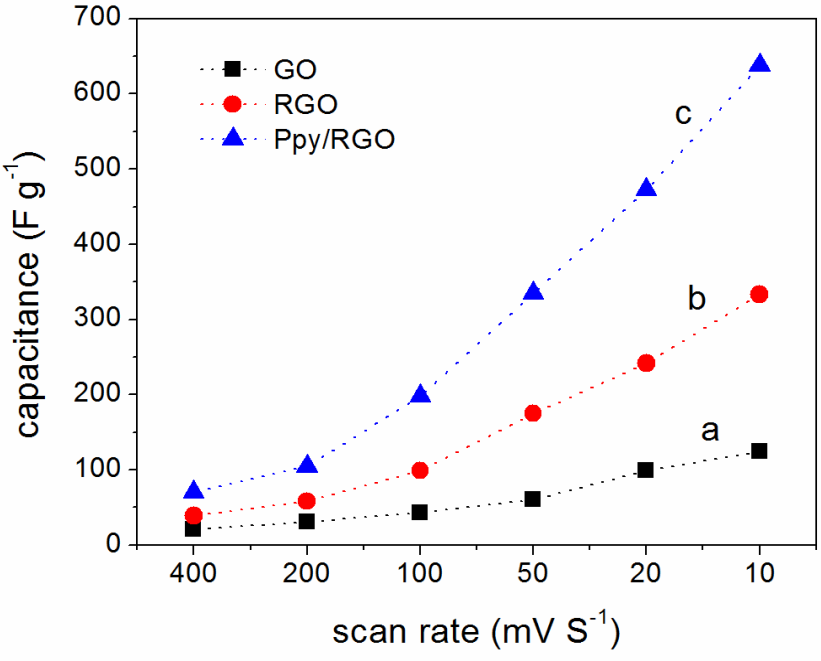

Figure 6.6 Specific capacitance Versus Scan rate of supercapacitors composed of different free standing electrodes (a) GO (b) RGO (c) PPy fibre/RGO

Fig 6.6 exhibits the variations of capacitance upon scan rates of all three types of capacitors. The capacitance were calculated according to the equation below,

$$C = \frac{1}{S\ m\ \Delta V}\int_{V}^{V+V_0} i dV$$

Where *S* is the scan rate of CV, *m* is the total loading mass of the electrodes, ΔV is the potential range and *i* is the current. The capacitance of supercapacitors with PPy fibre/RGO electrodes has the most significant growth at the lower scan rates which can be ascribed to the increased faradic capacitance obtained by more sufficient redox reaction of Polypyrrole. It is notable that the capacitance of capacitor with PPy/RGO film electrode retains more than double as much as that of the other two types, indicating that the capacitive behaviour of PPy fiber/RGO film electrodes maintained better at any scan rates. The galvanostatic charge/discharge of all three types of supercapacitors at the current density of 1A g^{-1}, were tested as showed in Fig 6.7.

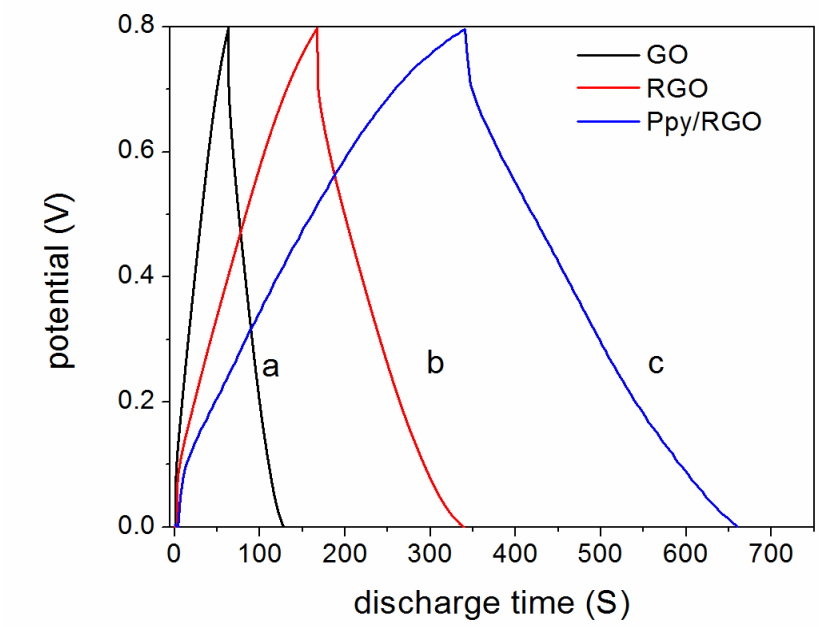

Figure 6.7 Galvanostatic charge–discharge curves of flexible supercapacitors with electrodes of (a) pure GO film (b) pure RGO film (c) PPy fibre/RGO film

There are small voltage drops (IR drops) showed in all the discharge cruves, which are caused by the internal resistance of the supercapacitors [285]. The Pure GO and RGO film showed the near triangle shaped charge/discharge curves suggesting that their capacitance are mainly contributed by the EDLs (electrochemical double layers). The capacitance of supercapacitor with pure RGO film (153F g^{-1}) is much higher than the one with GO film electrodes (53F g^{-1}). The discharge curve of PPy fibre /RGO film shows two stages with the first stage (0.75-0.25V) purely attributed to the EDLs capacitance and the second stage (0.25V -0V) with the EDLs and Faradic capacitance combined.

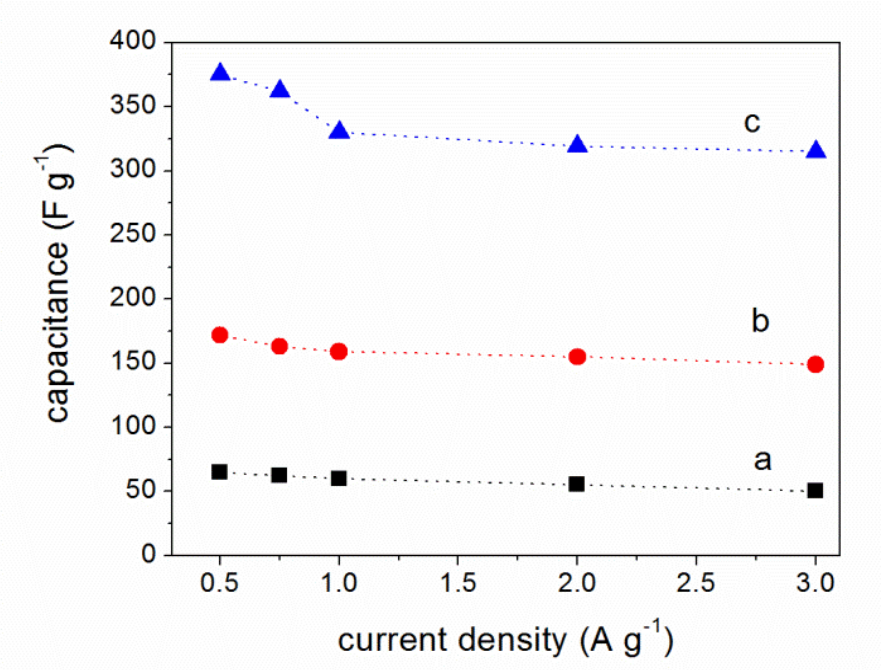

Figure 6.8 Capacitances versus charge/discharge current densities of flexible supercapacitors with electrodes of (a) pure GO film (b) pure RGO film (c) PPy fibre/RGO film

Fig 6.8 reveals the capacitances of all three types of supercapacitors at different discharge current densities. The capacitances of both Pure GO film and RGO film have no significant variation upon the charge/discharge rate due to their EDLs capacitive mechanism, whereas the capacitor composed of PPy fiber/RGO film electrode exhibit slight capacitance decrease at higher charge/discharge rate. This is mainly caused by the incomplete doping/dedoping reaction of PPy fibre, at which case, the pseudocapacitance belongs to the PPy fibre is decreased.

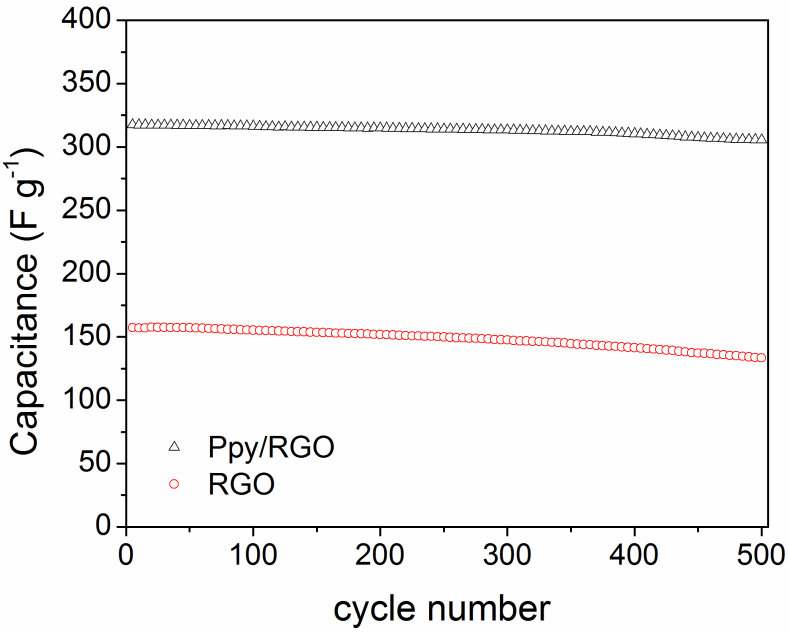

Figure 6.9 Cycling performances of supercapacitors with PPy fibre/RGO film (black triangle) electrodes and pure RGO film electrodes (red circle).

The cycling performances of both the supercapacitors composed of PPy fibre/RGO films and pure RGO films are showed in Fig 6.9. The retention rate of capacitance of both type of supercapacitors are excellent. The capacitance of the supercapacitor with PPy fibre/RGO film electrodes dropped only 3.4% after 500 cycles and the one with pure RGO film electrodes has the total capacitance reduction of 6.9% respectively. It is significant that the flexible supercapacitor with PPy fibre/RGO film has much higher capacitance and better cycling performance than the one with pure RGO film. The enhanced capacitance of the flexible supercapacitor with PPy fibre/RGO electrodes are mainly attributed by its porous structure between layers and faradic capacitance gained from the redox reaction of the polypyrrole component. It is interesting that its cycling

performance is much more stable than most supercapacitors with chemically synthesised PPy/RGO electrodes.

According to the surface morphology of the PPy fibre/RGO film showed in Fig 6.2 (d), the PPy fibres are mostly sandwiched by the sheer graphene nano sheets layer by layer, which protected PPy fibres from the volumetric swelling and deformation of polymer chains caused by the continuous injection and dejection of counter ions and charge carriers during the cyclic redox reactions[286]. Meanwhile, the protective graphene layers improved the charge transportation by reducing the charge transfer resistance. Therefore, the capacitance drop of such supercapacitor constructed by the multi-layer structured PPy fibre/RGO film electrodes during the cycling performances is much less significant when compared to those with chemically synthesised PPy/RGO electrodes.

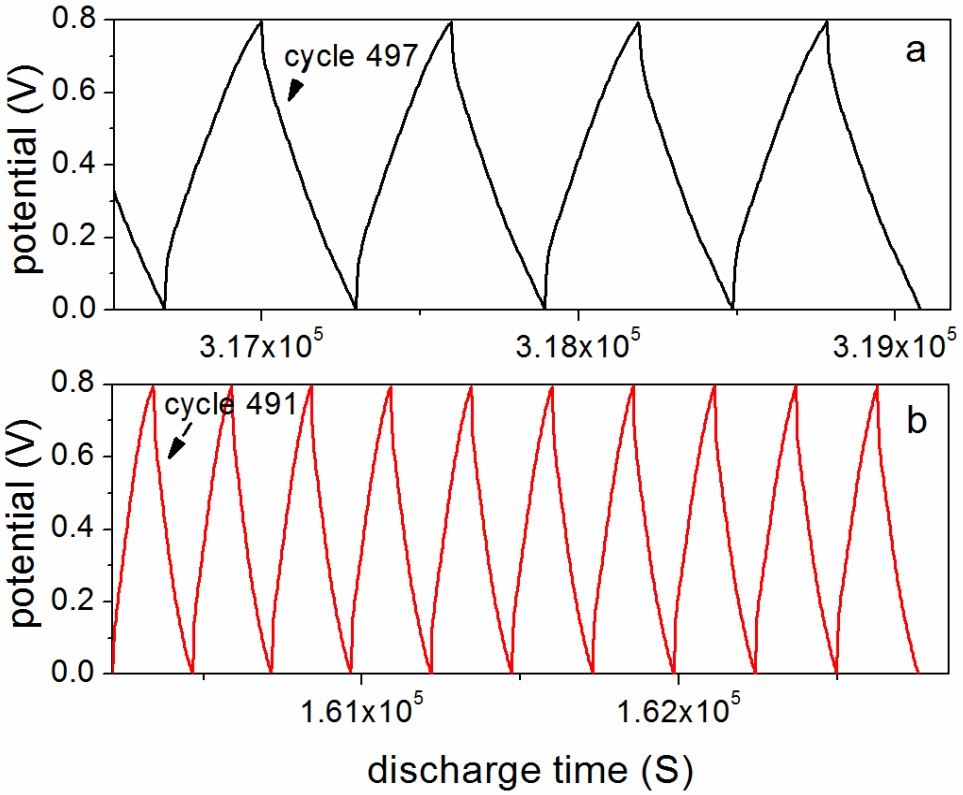

Figure 6.10 The galvanostatic charge–discharge curves under the current density of 1A g^{-1} snapped from the last few cycles of supercapacitors with (a) PPy fibre RGO film (b) Pure RGO film

Fig 6.10 showed the last few cycles of galvanostatic charge–discharge curves of both the flexible supercapacitors. The IR drops of both the devices are not enlarged which indicating the resistances of the whole devices are not significantly increased after long cycling period.

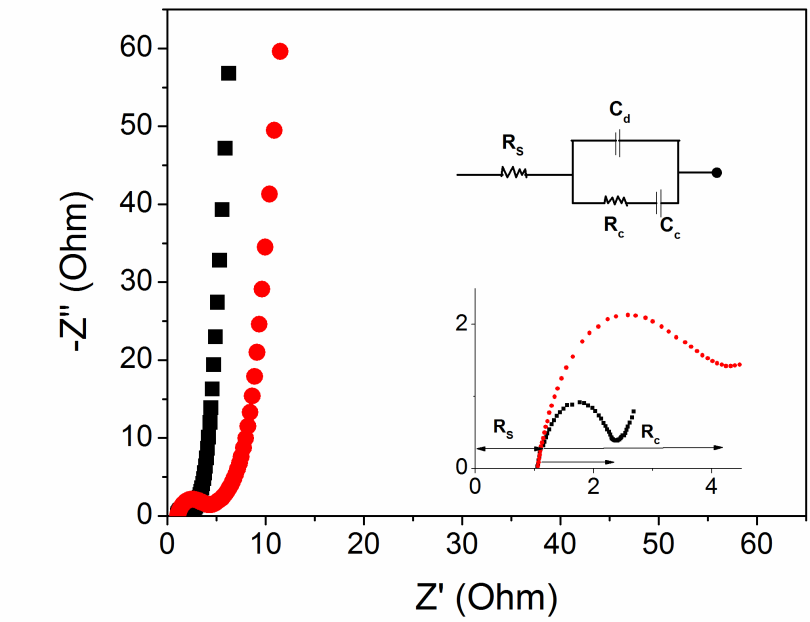

Figure 6.11 Nyquist plot of flexible supercapacitors constructed by pure RGO film electrode (black square) and PPy fibre/RGO film electrode (Red dot)

To prove this, Nyquist plots of electrochemical impedance spectroscopy for both the supercapacitors after 500 cycles are showed in Fig 6.11. The equivalent circuit of the impedance spectra is presented with several elements, including the resistance generated by the gel electrolyte Rs, the total charge transfer resistance Rc, the EDLs capacitance Cd and the pseudo-capacitive element Cp. The charge transfer resistance of pure RGO film is slightly smaller than the PPy fibre/RGO film since its charge transfer process occurs purely along the graphene basal plane. However, it is notable that the additional PPy fibres did not induce the large increase in charge transfer resistance despite that the charge transfer channels were interrupted by the porous PPy fibre layers.

6.4 Conclusion

The multi-layered flexible polypyrrole fibres/reduced graphene oxide films were prepared by a simple vacuum filtration method featured with excellent mechanical properties, high conductivity and excellent capacitive performances. After reduced by HI acid, the film maintained high flexibility and good elasticity. The supercapacitors constructed by the PPy/RGO film performed much better than the pure RGO film and GO film with a galvanostatic discharge capacitance up to 345 F g^{-1}. The enhanced capacitance can be explained by two contribute factors. Firstly, the polypyrrole fibre brings in the pseudo-capacitance by its revisable redox reaction. Second, the polypyrrole fibre helps to create the porous structures between graphene layers and thus enlarge the specific area of the electrodes. Meanwhile, they cycling performance of both the flexible supercapacitor with PPy fibre/RGO electrodes and pure RGO electrodes are all very stable however, the former one performed better than the latter with less than 3.4% capacitance drop after 500 cycles. This can be explained by the excellent charge transfer accessibility of the graphene nano sheets and its protective effects on the polypyrrole fibres.

Chapter 7

Conclusions and research suggestions

7.1 Conclusions

This thesis is focused on developing high performance bio-compatible materials for implantable energy devices. The Zinc/bio-fluids/CPs (CP composites) system and solid state supercapacitors are selected as the main research targets. The working principles, cell performance, the effect of electrolyte on the electrochemical performance of different electrode materials have been elucidated based on the solid and systematic experimental data.

In chapter one, the electrodeposited polypyrrole was applied as cathode material for the Zinc/bio-fluids/CPs battery system using a series of non-toxic aqueous electrolyte including 0.1 M NaCl, PBS solution and simulated body fluid. The battery with NaCl solution as electrolyte gained the highest capacity of up to 5600 mAh g^{-1}. The differences in discharge performances of the other two types of batteries are less distinctive. The Zn/PBS/PPy battery shows slightly higher discharge plateau and larger specific capacity than that of the Zn/SBF/PPy battery. Such phenomena are explained by the difference in ion exchange behaviours in the electrolytes based on the various electrochemical studies. The role of polypyrrole film in the battery is concluded as both an oxygen consumer which can catalyse the oxygen dissolution, and an electron

acceptor which helps to maintain the Zn dissolution rate. The high discharge capacity indicates that such battery system is capable of powering many bio-medical devices such as implantable endoscope, telemetric reading devices and even micro sized drug delivery pumps.

In the following work, the 3D nano structured polypyrrole/multi walled carbon nano tubes were synthesised using chemical polymerization method. Three different composites were produced from varied amounts of pyrrole monomer and constant contents of CNT. The PPy/CNT composite synthesised from 0.1M pyrrole and 0.4 mg mL^{-1} CNT suspension was tested as the best cathode material. The battery constructed by such cathode and SBF electrolyte is capable of being discharged up to 24.5 hours at a current density of 60 mA cm^{-2} in the protein free SBF. The batteries have also been tested in vitro using SBFs containing bovine serum albumin (BSA) with different concentrations. Such a battery can be charged up to 35.1 hours (1.26 W h) in the electrolyte containing 8 g L^{-1} BSA, which is 10% of the genuine protein concentration of blood plasma. The effects of adding protein (BSA) to the electrolyte on both the anodic reactions and the redox capabilities of the PPy–CNT cathodes was investigated. It was found that a small amount of BSA protein can stabilize the discharge potential and prolong the discharge plateau. However, as the protein concentration increases, the ionic charge transfer process can be retarded by the large protein molecules, inducing the decrease of discharge plateau and discharge capacity.

To further improve the bio-compatibility and electrochemical performances of the cathode material, in the following chapter, reduced graphene oxide was utilized as the

substrate for incorporating with polypyrrole fibres. The RGO/PPy composite was synthesised via a simple one step method from GO/pyrrole monomer mixtures precursor and treated with L-ascorbic acid at a relatively low temperature. The chemical characterization results suggested that the GO was successfully reduced by the L-ascorbic acid which has no obvious reducing effect on the oxidised PPy component. The resulting PPy/RGO composite shows large specific surface area (561 m^2 g^{-1}) and high electric conductivity (141 S cm^{-1}). Such material revealed excellent electrochemical performance as cathode material for battery with zinc as anode and SBF as electrolyte. Battery with such cathode showed distinctive higher discharge plateaus and higher energy density than the one with pure PPy fibre cathode. The synergism between the reduced graphene nano sheets and the polypyrrole fibres are significant since both the redox capability and electric conductivity of the material are improved. The RGO nano sheets are generally considered to be bio-compatible without any contradiction according to the research work published to date. Therefore, such material can be considered as an even better choice for the Zn/Bio-fluids/CPs battery system.

At last, the flexible solid state supercapacitors are constructed with the mechanical strong and highly conductive PPy fibre/RGO films. The solid state supercapacitors have been considered as the possible power sources for implantable wireless sensors or neuron stimulators. In this part, the PPy fibres/GO films were assembled through vacuum filtration, which is a simple but effective technique. The films are of a layered structure with polypyrrole fibres sandwiched between the GO nano sheets. After being reduced by the hydriodic acid, the mechanical properties of the films were retained well

without obvious damage. The supercapacitors constructed by the PPy/RGO film performed much better than the pure RGO film and GO film with a galvanostatic discharge capacitance up to 345 F g^{-1}. Meanwhile, it had only 3.4% capacitance drop within 500 cycles, revealing its excellent cycling stability.

In summary, this research project has achieved some preliminary success showing the promising prospects of conductive polymers and their composites as electrode material for bio-compatible power sources. The battery constructed with such materials as cathodes and zinc anodes generally displayed stable and long service lives at medium discharge potential range (0.9-0.7 V). Compared with other types of energy storage devices, such kind of systems has unique properties as for an implantable device, such as bio-compatibility, high energy density and controllable cell volume. However, there are still many technical challenges such as sealing techniques and materials, in-vivo testing and most importantly adapting the battery into a well-designed bio-medical device. In the following part, the author will gives out some sincere suggestions about the future research directions that could possibly produce breakthroughs in this field.

7.2 Suggestions about future work

- About the cathode materials

As it has been discussed throughout the thesis, an effective cathode material for the zinc/bio fluids/CPs battery system should basically possess three key factors, which are, high specific surface area, high electric conductivity and high redox activity. The

high specific surface area can produce large platform for interface reactions between the electrolyte and the cathode. The high electric conductivity can reduce the interface charge transfer resistance and the high redox activity is the main contributor for oxygen reduction reaction. In this work, we mainly focused on the polypyrrole as cathode materials. However, at the same time, there are some other CPs that are worth trying, such as Poly(3,4-ethylenedioxythiophene) (PEDOT).

As for polypyrrole based cathodes, there are still upgrading possibilities by novel synthesis method or by effective doping. For example, well aligned core shell structure with polypyrrole arrays coated by highly conductive carbon materials or aligned carbon nano tubes coated by polypyrrole should be a promising candidate. On the other hand, polypyrrole can be modified with redox active dopants which could enhance its reaction activity with oxygen.

- About battery configuration

The electrolyte applied for a Zinc/bio-fluids/CPs battery is usually the body fluids such as blood, silvia, urine, gastric fluids or even sweat. Some of these fluids need to be harvested by an absorbent layer to amass the adequate amount for powering the battery properly. In this case, bio-compatible absorbent materials can be used as the separator, for example, the hydrogel.

On the other side, the sealing technique of such battery is critical since the battery is targeted for in vivo implantation. The sealing material should be water permeable and bio-compatible, which can allow the water, small anions and cations transfer freely and prevent the leakage of reaction waste at the same time.

REFERENCES

1. D. C. Bock, A. C. Marschilok, K. J. Takeuchi and E. S. Takeuchi, *Electrochimica acta*, 2012, **84**, 155-164.
2. O. Soykan, *Medical Device Manufacturing & Technology*, 2002, 76-79.
3. A. P. Chandrakasan, N. Verma and D. C. Daly, *Annu. Rev. Biomed. Eng.*, 2008, **10**, 247-274.
4. S. Calabrese Barton, J. Gallaway and P. Atanassov, *Chemical Reviews*, 2004, **104**, 4867-4886.
5. K. Cook-Chennault, N. Thambi and A. Sastry, *Smart Materials and Structures*, 2008, **17**, 043001.
6. D. S. Weiss, R. Kirsner and W. H. Eaglstein, *Archives of dermatology*, 1990, **126**, 222.
7. L. Snyder-Mackler, A. Delitto, S. W. Stralka and S. L. Bailey, *Physical Therapy*, 1994, **74**, 901-907.
8. R. Dell, J. Gord and J. Schulman, Google Patents, 2003.
9. B. Burns, L. Watkins and P. J. Goadsby, *The Lancet*, 2007, **369**, 1099-1106.
10. P. C. Allen and R. Fetterer, *Clinical microbiology reviews*, 2002, **15**, 58-65.
11. D. A. Lavan, T. McGuire and R. Langer, *Nature biotechnology*, 2003, **21**, 1184-1191.
12. M. Rasouli and L. S. J. Phee, *Expert review of medical devices*, 2010, **7**, 693-709.
13. J. Y. Kang, *Encyclopedia of Medical Devices and Instrumentation*, 2006.
14. V. S. Mallela, V. Ilankumaran and N. S. Rao, *Indian pacing and electrophysiology journal*, 2004, **4**, 201.
15. X. Wei and J. Liu, *Frontiers of Energy and Power Engineering in China*, 2008, **2**, 1-13.
16. R. A. Powers, *Proceedings of the IEEE*, 1995, **83**, 687-693.
17. J. Rao and G. Richter, *Naturwissenschaften*, 1974, **61**, 200-206.
18. H. Jimbo and N. Miki, *Sensors and Actuators B: Chemical*, 2008, **134**, 219-224.
19. H. Liu and R. M. Crooks, *Analytical chemistry*, 2012, **84**, 2528-2532.
20. A. Baptista, J. Martins, E. Fortunato, R. Martins, J. Borges and I. Ferreira, *Biosensors and Bioelectronics*, 2011, **26**, 2742-2745.
21. C. F. Holmes, *Journal of power sources*, 2001, **97**, 739-741.
22. G. D. Nelson, *Texas Heart Institute Journal*, 1993, **20**, 12.
23. W. GREATBATCH and C. F. HOLMES, *Pacing and Clinical Electrophysiology*, 1992, **15**, 2034-2036.
24. E. S. Takeuchi and R. A. Leising, *MRS bulletin*, 2002, **27**, 624-627.
25. W. Greatbatch, C. Holmes, E. Takeuchi and S. Ebel, *Pacing and clinical electrophysiology*, 1996, **19**, 1836-1840.
26. J. Drews, G. Fehrmann, R. Staub and R. Wolf, *Journal of power sources*, 2001, **97**, 747-749.
27. A. Crespi, C. Schmidt, J. Norton, K. Chen and P. Skarstad, *Journal of The Electrochemical Society*, 2001, **148**, A30-A37.

28. C. L. Schmidt and P. M. Skarstad, *Journal of power sources*, 2001, **97**, 742-746.
29. J.-M. Tarascon and M. Armand, *Nature*, 2001, **414**, 359-367.
30. M. M. Archuleta, *Journal of power sources*, 1995, **54**, 138-142.
31. S. Fruitsmaak, An artificial pacemaker from St. Jude Medical, with electrode.
32. K. Chen, D. R. Merritt, W. G. Howard, C. L. Schmidt and P. M. Skarstad, *Journal of power sources*, 2006, **162**, 837-840.
33. M. Biffi, M. Ziacchi, M. Bertini, D. Sangiorgi, D. Corsini, C. Martignani, I. Diemberger and G. Boriani, *Europace*, 2008, **10**, 1288-1295.
34. R. A. Bullen, T. Arnot, J. Lakeman and F. Walsh, *Biosensors and Bioelectronics*, 2006, **21**, 2015-2045.
35. S. D. Minteer, B. Y. Liaw and M. J. Cooney, *Current opinion in biotechnology*, 2007, **18**, 228-234.
36. D. Leech, P. Kavanagh and W. Schuhmann, *Electrochimica Acta*, 2012, **84**, 223-234.
37. S. Kerzenmacher, J. Ducrée, R. Zengerle and F. Von Stetten, *Journal of Power Sources*, 2008, **182**, 1-17.
38. B. E. Logan, *Microbial fuel cells*, John Wiley & Sons, 2008.
39. B. E. Logan, B. Hamelers, R. Rozendal, U. Schröder, J. Keller, S. Freguia, P. Aelterman, W. Verstraete and K. Rabaey, *Environmental science & technology*, 2006, **40**, 5181-5192.
40. A. Rinaldi, B. Mecheri, V. Garavaglia, S. Licoccia, P. Di Nardo and E. Traversa, *Energy & Environmental Science*, 2008, **1**, 417-429.
41. A. E. Franks and K. Nevin, *Energies*, 2010, **3**, 899-919.
42. K. Rabaey and W. Verstraete, *TRENDS in Biotechnology*, 2005, **23**, 291-298.
43. D. Pant, G. Van Bogaert, L. Diels and K. Vanbroekhoven, *Bioresource technology*, 2010, **101**, 1533-1543.
44. J. R. Kim, B. Min and B. E. Logan, *Applied microbiology and biotechnology*, 2005, **68**, 23-30.
45. B. E. Logan and J. M. Regan, *Environmental science & technology*, 2006, **40**, 5172-5180.
46. B. H. Kim, I. S. Chang and G. M. Gadd, *Applied microbiology and biotechnology*, 2007, **76**, 485-494.
47. A. Heller, *Physical Chemistry Chemical Physics*, 2004, **6**, 209-216.
48. I. Willner, Y. M. Yan, B. Willner and R. Tel ‐ Vered, *Fuel Cells*, 2009, **9**, 7-24.
49. H. J. Kim, H. S. Park, M. S. Hyun, I. S. Chang, M. Kim and B. H. Kim, *Enzyme and Microbial Technology*, 2002, **30**, 145-152.
50. V. Coman, R. Ludwig, W. Harreither, D. Haltrich, L. Gorton, T. Ruzgas and S. Shleev, *Fuel Cells*, 2010, **10**, 9-16.
51. J. Kim, H. Jia and P. Wang, *Biotechnology advances*, 2006, **24**, 296-308.
52. I. Ivanov, T. Vidaković-Koch and K. Sundmacher, *Energies*, 2010, **3**, 803-846.
53. J. Kim, J. W. Grate and P. Wang, *Trends in biotechnology*, 2008, **26**, 639-646.
54. Y. Qiao and C. M. Li, *Journal of Materials Chemistry*, 2011, **21**, 4027-4036.
55. D. H. Park and J. G. Zeikus, *Biotechnology and bioengineering*, 2003, **81**, 348-355.

56. A. Kannan, V. Renugopalakrishnan, S. Filipek, P. Li, G. Audette and L. Munukutla, *Journal of nanoscience and nanotechnology*, 2009, **9**, 1665-1678.
57. S. Corporate, in *SONY Global Website*, 2007 Aug 23.
58. A. Tseung, W. King and B. Wan, *Medical and biological engineering*, 1971, **9**, 175-184.
59. S. Hejian and H. Shizhong, *Chinese Journal of Oceanology and Limnology*, 1990, **8**, 354-362.
60. O. Roy, R. Wehnert, H. Heggtveit and W. Waddell, *Annals of the New York Academy of Sciences*, 1969, **167**, 645-660.
61. B. Wan and A. Tseung, *Medical and biological engineering*, 1974, **12**, 14-28.
62. L. Geddes and R. Roeder, *Annals of biomedical engineering*, 2003, **31**, 879-890.
63. K. B. Lee, *Journal of Micromechanics and Microengineering*, 2006, **16**, 2312.
64. K. B. Lee, *Journal of Micromechanics and Microengineering*, 2005, **15**, S210.
65. F. Cheng and J. Chen, *Chemical Society Reviews*, 2012, **41**, 2172-2192.
66. K. Harting, U. Kunz and T. Turek, *Zeitschrift fur Physikalische Chemie*, 2012, **226**, 151.
67. Q. Li and N. J. Bjerrum, *Journal of Power Sources*, 2002, **110**, 1-10.
68. D. D. Macdonald and C. English, *Journal of Applied Electrochemistry*, 1990, **20**, 405-417.
69. M. Armand and J.-M. Tarascon, *Nature*, 2008, **451**, 652-657.
70. A. Heller, *Analytical and bioanalytical chemistry*, 2006, **385**, 469-473.
71. T. Khoo, P. C. Howlett, M. Tsagouria, D. R. MacFarlane and M. Forsyth, *Electrochimica acta*, 2011, **58**, 583-588.
72. B. Winther-Jensen, M. Gaadingwe, D. Macfarlane and M. Forsyth, *Electrochimica Acta*, 2008, **53**, 5881-5884.
73. M. Amaral, F. do Vale, J. Silva, F. Caramelo and G. Veiga, *Journal of Medical Devices*, 2014, **8**, 014509.
74. G. Pistoia, *Batteries for portable devices*, Elsevier, 2005.
75. J. S. Lee, S. Tai Kim, R. Cao, N. S. Choi, M. Liu, K. T. Lee and J. Cho, *Advanced Energy Materials*, 2011, **1**, 34-50.
76. C. Chakkaravarthy, A. Waheed and H. Udupa, *Journal of Power Sources*, 1981, **6**, 203-228.
77. P. Sapkota and H. Kim, *Journal of Industrial and Engineering Chemistry*, 2009, **15**, 445-450.
78. S. Müller, F. Holzer and O. Haas, *Journal of applied electrochemistry*, 1998, **28**, 895-898.
79. X. G. Zhang, *Corrosion and electrochemistry of zinc*, Springer, 1996.
80. M. McKubre and D. Macdonald, *Journal of the Electrochemical Society*, 1981, **128**, 524-530.
81. V. Neburchilov, H. Wang, J. J. Martin and W. Qu, *Journal of power sources*, 2010, **195**, 1271-1291.
82. X. Wang, P. Sebastian, M. A. Smit, H. Yang and S. Gamboa, *Journal of power sources*, 2003, **124**, 278-284.
83. W. Zhu, B. Poole, D. Cahela and B. Tatarchuk, *Journal of applied electrochemistry*, 2003, **33**, 29-36.
84. D. Linden, *New York*, 1984.

85. B. Kim, 2013.
86. B. Wang, *Journal of Power Sources*, 2005, **152**, 1-15.
87. S.-W. Eom, S.-Y. Ahn, I.-J. Kim, Y.-K. Sun and H.-S. Kim, *Journal of electroceramics*, 2009, **23**, 382-386.
88. A. Weidenkaff, *Advanced engineering materials*, 2004, **6**, 709-714.
89. G. Du, X. Liu, Y. Zong, T. A. Hor, A. Yu and Z. Liu, *Nanoscale*, 2013, **5**, 4657-4661.
90. Y. Sun, C. Li and G. Shi, *Journal of Materials Chemistry*, 2012, **22**, 12810-12816.
91. T. Zhang, Z. Tao and J. Chen, *Materials Horizons*, 2014.
92. G. Girishkumar, B. McCloskey, A. Luntz, S. Swanson and W. Wilcke, *The Journal of Physical Chemistry Letters*, 2010, **1**, 2193-2203.
93. Z. Lu, A. Schechter, M. Moshkovich and D. Aurbach, *Journal of Electroanalytical Chemistry*, 1999, **466**, 203-217.
94. G. Song, A. Atrens, D. Stjohn, J. Nairn and Y. Li, *Corrosion Science*, 1997, **39**, 855-875.
95. M. Straumanis and B. Bhatia, *Journal of the Electrochemical Society*, 1963, **110**, 357-360.
96. Y. Ma, N. Li, D. Li, M. Zhang and X. Huang, *Journal of Power Sources*, 2011, **196**, 2346-2350.
97. G. Huang, Y. Zhao, Y. Wang, H. Zhang and F. Pan, *Materials Letters*, 2013, **113**, 46-49.
98. Y. Milusheva, R. Boukoureshtlieva, S. Hristov and A. Kaisheva, 2011.
99. A. Kaisheva and I. Iliev, in *New Carbon Based Materials for Electrochemical Energy Storage Systems: Batteries, Supercapacitors and Fuel Cells*, Springer, 2006, pp. 105-116.
100. S. Sathyanarayana and N. Munichandraiah, *Journal of Applied Electrochemistry*, 1981, **11**, 33-39.
101. D. Hauk, S. Lang and A. Murso, *Organic process research & development*, 2006, **10**, 733-738.
102. Y. Kong, C. Wang, Y. Yang, C. O. Too and G. G. Wallace, *Synthetic Metals*, 2012, **162**, 584-589.
103. G. Nyström, A. Razaq, M. Strømme, L. Nyholm and A. Mihranyan, *Nano letters*, 2009, **9**, 3635-3639.
104. B. Scrosati, *Nature nanotechnology*, 2007, **2**, 598-599.
105. V. L. Pushparaj, M. M. Shaijumon, A. Kumar, S. Murugesan, L. Ci, R. Vajtai, R. J. Linhardt, O. Nalamasu and P. M. Ajayan, *Proceedings of the National Academy of Sciences*, 2007, **104**, 13574-13577.
106. M. Winter and R. J. Brodd, *Chemical reviews*, 2004, **104**, 4245-4270.
107. B. E. Conway, 1999.
108. Cap-xx, 2007.
109. F. J. Barreras, Google Patents, 1998.
110. E. Feldman, M. I. Haller and J. Parramon, Google Patents, 2012.
111. A. Pandey, F. Allos, A. P. Hu and D. Budgett, in *Industrial Electronics and Applications (ICIEA), 2011 6th IEEE Conference on*, IEEE, 2011, pp. 56-61.
112. C. Meng, C. Liu, L. Chen, C. Hu and S. Fan, *Nano letters*, 2010, **10**, 4025-4031.

113. C. Meng, O. Z. Gall and P. P. Irazoqui, *Biomedical microdevices*, 2013, **15**, 973-983.
114. J. Drews, R. Wolf, G. Fehrmann and R. Staub, *Journal of power sources*, 1999, **80**, 107-111.
115. C. Chan, *Proceedings of the IEEE*, 2007, **95**, 704-718.
116. H. Shirakawa, E. J. Louis, A. G. MacDiarmid, C. K. Chiang and A. J. Heeger, *Journal of the Chemical Society, Chemical Communications*, 1977, 578-580.
117. D. E. Tallman, G. Spinks, A. Dominis and G. G. Wallace, *Journal of Solid State Electrochemistry*, 2002, **6**, 73-84.
118. M. Gerard, A. Chaubey and B. Malhotra, *Biosensors and Bioelectronics*, 2002, **17**, 345-359.
119. A. Rudge, J. Davey, I. Raistrick, S. Gottesfeld and J. P. Ferraris, *Journal of Power Sources*, 1994, **47**, 89-107.
120. E. Smela, *Advanced Materials*, 2003, **15**, 481-494.
121. J.-L. Brédas and R. Silbey, *Conjugated polymers: the novel science and technology of highly conducting and nonlinear optically active materials*, Springer, 1991.
122. F. Jonas and G. Heywang, *Electrochimica acta*, 1994, **39**, 1345-1347.
123. T. A. Skotheim, *Handbook of conducting polymers*, CRC press, 1997.
124. P. Chandrasekhar, *Conducting polymers, fundamentals and applications: a practical approach*, Springer, 1999.
125. N. K. Guimard, N. Gomez and C. E. Schmidt, *Progress in Polymer Science*, 2007, **32**, 876-921.
126. V. Khomenko, V. Barsukov and A. Katashinskii, *Electrochimica Acta*, 2005, **50**, 1675-1683.
127. B. Winther-Jensen, O. Winther-Jensen, M. Forsyth and D. R. MacFarlane, *Science*, 2008, **321**, 671-674.
128. P. M. Carrasco, H. J. Grande, M. Cortazar, J. M. Alberdi, J. Areizaga and J. A. Pomposo, *Synthetic metals*, 2006, **156**, 420-425.
129. R. Ansari, *Journal of Chemistry*, 2006, **3**, 186-201.
130. X. Zhang and S. K. Manohar, *Journal of the American Chemical Society*, 2005, **127**, 14156-14157.
131. J. Jang and H. Yoon, *Chem. Commun.*, 2003, 720-721.
132. J. Wu, Q. Li, L. Fan, Z. Lan, P. Li, J. Lin and S. Hao, *Journal of Power Sources*, 2008, **181**, 172-176.
133. A. Baba and W. Knoll, *Advanced Materials*, 2003, **15**, 1015-1019.
134. L.-X. Wang, X.-G. Li and Y.-L. Yang, *Reactive and Functional Polymers*, 2001, **47**, 125-139.
135. M. Aldissi and S. Armes, *Progress in organic coatings*, 1991, **19**, 21-58.
136. M. Wan, *Advanced Materials*, 2008, **20**, 2926-2932.
137. L. Pan, H. Qiu, C. Dou, Y. Li, L. Pu, J. Xu and Y. Shi, *International journal of molecular sciences*, 2010, **11**, 2636-2657.
138. T. Dai, X. Yang and Y. Lu, *Nanotechnology*, 2006, **17**, 3028.
139. C. R. Martin, DTIC Document, 1994.
140. C. R. Martin, *Accounts of chemical research*, 1995, **28**, 61-68.
141. Y. Berdichevsky and Y. H. Lo, *Advanced Materials*, 2006, **18**, 122-125.

142. A. Thomas, F. Goettmann and M. Antonietti, *Chemistry of Materials*, 2008, **20**, 738-755.
143. A. Diaz, K. K. Kanazawa and G. P. Gardini, *Journal of the Chemical Society, Chemical Communications*, 1979, 635-636.
144. J. M. Pringle, J. Efthimiadis, P. C. Howlett, J. Efthimiadis, D. R. MacFarlane, A. B. Chaplin, S. B. Hall, D. L. Officer, G. G. Wallace and M. Forsyth, *Polymer*, 2004, **45**, 1447-1453.
145. M. Satoh, K. Kaneto and K. Yoshino, *Synthetic metals*, 1986, **14**, 289-296.
146. S. Sadki, P. Schottland, N. Brodie and G. Sabouraud, *Chemical Society Reviews*, 2000, **29**, 283-293.
147. E. Kupila and J. Kankare, *Synthetic metals*, 1993, **55**, 1402-1405.
148. W. Liang, J. Lei and C. R. Martin, *Synthetic metals*, 1992, **52**, 227-239.
149. K. Cheung, D. Bloor and G. Stevens, *Polymer*, 1988, **29**, 1709-1717.
150. D. Ateh, H. Navsaria and P. Vadgama, *Journal of the royal society interface*, 2006, **3**, 741-752.
151. M. Nechtschein, F. Devreux, F. Genoud, E. Vieil, J. Pernaut and E. Genies, *Synthetic metals*, 1986, **15**, 59-78.
152. J. Kaufman, N. Colaneri, J. Scott and G. Street, *Physical review letters*, 1984, **53**, 1005-1008.
153. G. Street, T. Clarke, M. Krounbi, K. Kanazawa, V. Lee, P. Pfluger, J. Scott and G. Weiser, *Molecular Crystals and Liquid Crystals*, 1982, **83**, 253-264.
154. J. Bredas, B. Themans and J. Andre, *Physical Review B*, 1983, **27**, 7827.
155. R. C. Peres, M.-A. De Paoli and R. M. Torresi, *Synthetic metals*, 1992, **48**, 259-270.
156. L.-Z. Fan and J. Maier, *Electrochemistry communications*, 2006, **8**, 937-940.
157. G. G. Wallace, P. R. Teasdale, G. M. Spinks and L. A. Kane-Maguire, *Conductive electroactive polymers: intelligent polymer systems*, CRC press, 2008.
158. H. Ge and G. Wallace, *Reactive polymers*, 1992, **18**, 133-140.
159. X. Wang, X. Gu, C. Yuan, S. Chen, P. Zhang, T. Zhang, J. Yao, F. Chen and G. Chen, *Journal of Biomedical Materials Research Part A*, 2004, **68**, 411-422.
160. A. K. Geim and K. S. Novoselov, *Nature materials*, 2007, **6**, 183-191.
161. J. Wang, S. Yang, D. Guo, P. Yu, D. Li, J. Ye and L. Mao, *Electrochemistry Communications*, 2009, **11**, 1892-1895.
162. K. I. Bolotin, K. Sikes, Z. Jiang, M. Klima, G. Fudenberg, J. Hone, P. Kim and H. Stormer, *Solid State Communications*, 2008, **146**, 351-355.
163. M. Pumera, *Energy & Environmental Science*, 2011, **4**, 668-674.
164. A. K. Geim, *Science*, 2009, **324**, 1530-1534.
165. Z. Chen, Y.-M. Lin, M. J. Rooks and P. Avouris, *Physica E: Low-dimensional Systems and Nanostructures*, 2007, **40**, 228-232.
166. K. Subrahmanyam, L. Panchakarla, A. Govindaraj and C. Rao, *The Journal of Physical Chemistry C*, 2009, **113**, 4257-4259.
167. Z. Chen, W. Ren, L. Gao, B. Liu, S. Pei and H.-M. Cheng, *Nature materials*, 2011, **10**, 424-428.
168. W. Zhao, M. Fang, F. Wu, H. Wu, L. Wang and G. Chen, *J. Mater. Chem.*, 2010, **20**, 5817-5819.

169. W. S. Hummers Jr and R. E. Offeman, *Journal of the American Chemical Society*, 1958, **80**, 1339-1339.
170. D. R. Dreyer, S. Park, C. W. Bielawski and R. S. Ruoff, *Chemical Society Reviews*, 2010, **39**, 228-240.
171. H. J. Shin, K. K. Kim, A. Benayad, S. M. Yoon, H. K. Park, I. S. Jung, M. H. Jin, H. K. Jeong, J. M. Kim and J. Y. Choi, *Advanced Functional Materials*, 2009, **19**, 1987-1992.
172. S. Stankovich, D. A. Dikin, R. D. Piner, K. A. Kohlhaas, A. Kleinhammes, Y. Jia, Y. Wu, S. T. Nguyen and R. S. Ruoff, *Carbon*, 2007, **45**, 1558-1565.
173. J. Zhang, H. Yang, G. Shen, P. Cheng, J. Zhang and S. Guo, *Chemical Communications*, 2010, **46**, 1112-1114.
174. P. Song, X. Zhang, M. Sun, X. Cui and Y. Lin, *Rsc Advances*, 2012, **2**, 1168-1173.
175. S. Pei, J. Zhao, J. Du, W. Ren and H.-M. Cheng, *Carbon*, 2010, **48**, 4466-4474.
176. X. Mei and J. Ouyang, *Carbon*, 2011, **49**, 5389-5397.
177. Y. Zhou, Q. Bao, L. A. L. Tang, Y. Zhong and K. P. Loh, *Chemistry of Materials*, 2009, **21**, 2950-2956.
178. X. Liu, L. Pan, Q. Zhao, T. Lv, G. Zhu, T. Chen, T. Lu, Z. Sun and C. Sun, *Chemical Engineering Journal*, 2012, **183**, 238-243.
179. K. Wang, J. Ruan, H. Song, J. Zhang, Y. Wo, S. Guo and D. Cui, *Nanoscale Res Lett*, 2011, **6**.
180. X. Zhang, J. Yin, C. Peng, W. Hu, Z. Zhu, W. Li, C. Fan and Q. Huang, *Carbon*, 2011, **49**, 986-995.
181. H. Chen, M. B. Müller, K. J. Gilmore, G. G. Wallace and D. Li, *Advanced Materials*, 2008, **20**, 3557-3561.
182. J. Shen, Y. Zhu, X. Yang and C. Li, *Chemical Communications*, 2012, **48**, 3686-3699.
183. Y. Shao, J. Wang, H. Wu, J. Liu, I. A. Aksay and Y. Lin, *Electroanalysis*, 2010, **22**, 1027-1036.
184. Y. Wang, Z. Li, J. Wang, J. Li and Y. Lin, *Trends in biotechnology*, 2011, **29**, 205-212.
185. J. T. Robinson, S. M. Tabakman, Y. Liang, H. Wang, H. Sanchez Casalongue, D. Vinh and H. Dai, *Journal of the American Chemical Society*, 2011, **133**, 6825-6831.
186. O. Akhavan, E. Ghaderi, S. Aghayee, Y. Fereydooni and A. Talebi, *Journal of Materials Chemistry*, 2012, **22**, 13773-13781.
187. K. Yang, J. Wan, S. Zhang, B. Tian, Y. Zhang and Z. Liu, *Biomaterials*, 2012, **33**, 2206-2214.
188. W. Hu, C. Peng, W. Luo, M. Lv, X. Li, D. Li, Q. Huang and C. Fan, *Acs Nano*, 2010, **4**, 4317-4323.
189. O. Akhavan and E. Ghaderi, *Acs Nano*, 2010, **4**, 5731-5736.
190. S. Liu, T. H. Zeng, M. Hofmann, E. Burcombe, J. Wei, R. Jiang, J. Kong and Y. Chen, *Acs Nano*, 2011, **5**, 6971-6980.
191. S. Iijima and T. Ichihashi, 1993.
192. J. W. Wilder, L. C. Venema, A. G. Rinzler, R. E. Smalley and C. Dekker, *Nature*, 1998, **391**, 59-62.

193. X. Wang, Q. Li, J. Xie, Z. Jin, J. Wang, Y. Li, K. Jiang and S. Fan, *Nano letters*, 2009, **9**, 3137-3141.
194. D. Tasis, N. Tagmatarchis, A. Bianco and M. Prato, *Chemical reviews*, 2006, **106**, 1105-1136.
195. S. Iijima, *Physica B: Condensed Matter*, 2002, **323**, 1-5.
196. R. H. Baughman, A. A. Zakhidov and W. A. de Heer, *Science*, 2002, **297**, 787-792.
197. J. Carrero-Sanchez, A. Elias, R. Mancilla, G. Arrellin, H. Terrones, J. Laclette and M. Terrones, *Nano Letters*, 2006, **6**, 1609-1616.
198. D. A. Nayagam, R. A. Williams, J. Chen, K. A. Magee, J. Irwin, J. Tan, P. Innis, R. T. Leung, S. Finch and C. E. Williams, *Small*, 2011, **7**, 1035-1042.
199. M. A. Correa-Duarte, N. Wagner, J. Rojas-Chapana, C. Morsczeck, M. Thie and M. Giersig, *Nano Letters*, 2004, **4**, 2233-2236.
200. M. Shim, N. W. Shi Kam, R. J. Chen, Y. Li and H. Dai, *Nano Letters*, 2002, **2**, 285-288.
201. A. S. Aricò, P. Bruce, B. Scrosati, J.-M. Tarascon and W. Van Schalkwijk, *Nature materials*, 2005, **4**, 366-377.
202. W. Greatbatch, J. H. Lee, W. Mathias, M. Eldridge, J. R. Moser and A. A. Schneider, *Biomedical Engineering, IEEE Transactions on*, 1971, 317-324.
203. A. M. Crespi, S. K. Somdahl, C. L. Schmidt and P. M. Skarstad, *Journal of power sources*, 2001, **96**, 33-38.
204. K. Goto, T. Nakagawa, O. Nakamura and S. Kawata, *Biomedical Engineering, IEEE Transactions on*, 2001, **48**, 830-833.
205. J. H. Schulman, A. A. Maltan and T. A. Santogrossi, Google Patents, 2005.
206. A. Darwish and A. E. Hassanien, *Sensors*, 2011, **11**, 5561-5595.
207. G. J. Fosmire, *The American journal of clinical nutrition*, 1990, **51**, 225-227.
208. X. Gu, Y. Zheng, Y. Cheng, S. Zhong and T. Xi, *Biomaterials*, 2009, **30**, 484-498.
209. T. Kokubo and H. Takadama, *Biomaterials*, 2006, **27**, 2907-2915.
210. P. M. George, A. W. Lyckman, D. A. LaVan, A. Hegde, Y. Leung, R. Avasare, C. Testa, P. M. Alexander, R. Langer and M. Sur, *Biomaterials*, 2005, **26**, 3511-3519.
211. M. Omastova, M. Trchova, J. Kovářová and J. Stejskal, *Synthetic Metals*, 2003, **138**, 447-455.
212. L. Yongfang and Q. Renyuan, *Journal of Electroanalytical Chemistry*, 1993, **362**, 267-272.
213. R. J. Mammone and A. G. MacDiarmid, *Synthetic metals*, 1984, **9**, 143-154.
214. R. J. Mammone and A. G. MacDiarmid, *Journal of the Chemical Society, Faraday Transactions 1: Physical Chemistry in Condensed Phases*, 1985, **81**, 105-112.
215. P. Dyreklev, M. Granström, O. Inganäs, L. Gunaratne, G. Senadeera, S. Skaarup and K. West, *Polymer*, 1996, **37**, 2609-2613.
216. P. Christensen and A. Hamnett, *Electrochimica acta*, 1991, **36**, 1263-1286.
217. X. Ren and P. G. Pickup, *Journal of Electroanalytical chemistry*, 1997, **420**, 251-257.
218. L. Baugh, *Electrochimica Acta*, 1979, **24**, 657-667.
219. C. Hsueh and A. Brajter-Toth, *Analytical Chemistry*, 1994, **66**, 2458-2464.

220. D. Ofer, R. M. Crooks and M. S. Wrighton, *Journal of the American Chemical Society*, 1990, **112**, 7869-7879.
221. T. Osaka, T. Momma, S.-i. Komaba, H. Kanagawa and S. Nakamura, *Journal of Electroanalytical Chemistry*, 1994, **372**, 201-207.
222. C. Weidlich, K.-M. Mangold and K. Jüttner, *Electrochimica Acta*, 2005, **50**, 1547-1552.
223. R. Ansari Khalkhali, W. Price and G. G. Wallace, *Reactive and Functional polymers*, 2003, **56**, 141-146.
224. J. R. Scully, D. C. Silverman and M. W. Kendig, *Electrochemical impedance: analysis and interpretation*, ASTM International, 1993.
225. Y.-C. Liu, B.-J. Hwang, W.-J. Jian and R. Santhanam, *Thin Solid Films*, 2000, **374**, 85-91.
226. M. Santos, A. Brolo and E. Girotto, *Electrochimica acta*, 2007, **52**, 6141-6145.
227. Y.-C. Liu and B.-J. Hwang, *Synthetic Metals*, 2000, **113**, 203-207.
228. C. Zhong, Z. Tian and Z. Tian, *Journal of Physical Chemistry*, 1990, **94**, 2171-2175.
229. S. V. Dorozhkin and E. I. Dorozhkina, *Colloids and Surfaces A: Physicochemical and Engineering Aspects*, 2003, **215**, 191-199.
230. T. M. Wu and S. H. Lin, *Journal of Polymer Science Part B: Polymer Physics*, 2006, **44**, 1413-1418.
231. E. T. Thostenson, Z. Ren and T.-W. Chou, *Composites science and technology*, 2001, **61**, 1899-1912.
232. A. Lasia, in *Modern aspects of electrochemistry*, Springer, 2002, pp. 143-248.
233. A. Tenno, R. Tenno and T. Suntio, in *Telecommunications Energy Conference, 2002. INTELEC. 24th Annual International*, IEEE, 2002, pp. 176-183.
234. D. Linden and T. B. Reddy, *New York*, 2002.
235. J. Dobryszycki and S. Biallozor, *Corrosion Science*, 2001, **43**, 1309-1319.
236. M. Zhou, Y. Zhai and S. Dong, *Analytical Chemistry*, 2009, **81**, 5603-5613.
237. Y.-K. Kim, M.-H. Kim and D.-H. Min, *Chemical Communications*, 2011, **47**, 3195-3197.
238. S.-L. Chou, J.-Z. Wang, M. Choucair, H.-K. Liu, J. A. Stride and S.-X. Dou, *Electrochemistry Communications*, 2010, **12**, 303-306.
239. S. Chen, J. Zhu, X. Wu, Q. Han and X. Wang, *ACS nano*, 2010, **4**, 2822-2830.
240. X.-Y. Zhang, H.-P. Li, X.-L. Cui and Y. Lin, *Journal of Materials Chemistry*, 2010, **20**, 2801-2806.
241. L. L. Zhang, S. Zhao, X. N. Tian and X. Zhao, *Langmuir*, 2010, **26**, 17624-17628.
242. X. Zhang, J. Zhang, W. Song and Z. Liu, *The Journal of Physical Chemistry B*, 2006, **110**, 1158-1165.
243. Y. Xu, H. Bai, G. Lu, C. Li and G. Shi, *Journal of the American Chemical Society*, 2008, **130**, 5856-5857.
244. T. Kokubo, H. Kushitani, S. Sakka, T. Kitsugi and T. Yamamuro, *Journal of biomedical materials research*, 1990, **24**, 721-734.
245. C. Xu, J. Sun and L. Gao, *Journal of Materials Chemistry*, 2011, **21**, 11253-11258.
246. M. S. Dresselhaus, A. Jorio, M. Hofmann, G. Dresselhaus and R. Saito, *Nano letters*, 2010, **10**, 751-758.

247. Y. Zhu, M. D. Stoller, W. Cai, A. Velamakanni, R. D. Piner, D. Chen and R. S. Ruoff, *Acs Nano*, 2010, **4**, 1227-1233.
248. J. Gao, F. Liu, Y. Liu, N. Ma, Z. Wang and X. Zhang, *Chemistry of Materials*, 2010, **22**, 2213-2218.
249. C. Malitesta, I. Losito, L. Sabbatini and P. G. Zambonin, *Journal of Electron Spectroscopy and Related Phenomena*, 1995, **76**, 629-634.
250. E. Kang, K. Neoh and K. Tan, *Surface and interface analysis*, 1992, **19**, 33-37.
251. C. Jin, F. Yang and W. Yang, *Journal of applied polymer science*, 2006, **101**, 2518-2522.
252. D. L. Miller and J. O. M. Bockris, *Journal of the Electrochemical Society*, 1992, **139**, 967-976.
253. J. R. Macdonald and E. Barsoukov, *History*, 2005, **1**, 8.
254. C. Liu, Q. Bi, A. Leyland and A. Matthews, *Corrosion Science*, 2003, **45**, 1257-1273.
255. M. Conte, P. Prosini and S. Passerini, *Materials Science and Engineering: B*, 2004, **108**, 2-8.
256. A. Burke, *Journal of power sources*, 2000, **91**, 37-50.
257. B. Conway, *Electrochemical supercapacitors: scientific fundamentals and technological applications (POD)*, Kluwer Academic/Plenum: New York, 1999.
258. E. Hwang, S. Adam and S. D. Sarma, *Physical review letters*, 2007, **98**, 186806.
259. Y. Si and E. T. Samulski, *Nano Letters*, 2008, **8**, 1679-1682.
260. M. D. Stoller, S. Park, Y. Zhu, J. An and R. S. Ruoff, *Nano Letters*, 2008, **8**, 3498-3502.
261. L. L. Zhang, R. Zhou and X. Zhao, *Journal of Materials Chemistry*, 2010, **20**, 5983-5992.
262. L. L. Zhang and X. Zhao, *Chemical Society Reviews*, 2009, **38**, 2520-2531.
263. Y. Wang, Z. Shi, Y. Huang, Y. Ma, C. Wang, M. Chen and Y. Chen, *The Journal of Physical Chemistry C*, 2009, **113**, 13103-13107.
264. C. Liu, Z. Yu, D. Neff, A. Zhamu and B. Z. Jang, *Nano letters*, 2010, **10**, 4863-4868.
265. D. A. Dikin, S. Stankovich, E. J. Zimney, R. D. Piner, G. H. Dommett, G. Evmenenko, S. T. Nguyen and R. S. Ruoff, *Nature*, 2007, **448**, 457-460.
266. H. Gwon, H.-S. Kim, K. U. Lee, D.-H. Seo, Y. C. Park, Y.-S. Lee, B. T. Ahn and K. Kang, *Energy & Environmental Science*, 2011, **4**, 1277-1283.
267. C. Wang, D. Li, C. O. Too and G. G. Wallace, *Chemistry of Materials*, 2009, **21**, 2604-2606.
268. F. Belhachemi, S. Rael and B. Davat, in *Industry Applications Conference, 2000. Conference Record of the 2000 IEEE*, IEEE, 2000, pp. 3069-3076.
269. C. Arbizzani, M. Mastragostino and L. Meneghello, *Electrochimica Acta*, 1996, **41**, 21-26.
270. M. Mastragostino, C. Arbizzani and F. Soavi, *Solid state ionics*, 2002, **148**, 493-498.
271. D. Zhang, X. Zhang, Y. Chen, P. Yu, C. Wang and Y. Ma, *Journal of Power Sources*, 2011, **196**, 5990-5996.
272. S. Bose, N. H. Kim, T. Kuila, K.-t. Lau and J. H. Lee, *Nanotechnology*, 2011, **22**, 295202.

273. A. Davies, P. Audette, B. Farrow, F. Hassan, Z. Chen, J.-Y. Choi and A. Yu, *The Journal of Physical Chemistry C*, 2011, **115**, 17612-17620.
274. P. Si, S. Ding, X.-W. D. Lou and D.-H. Kim, *RSC Advances*, 2011, **1**, 1271-1278.
275. W. Zhong, S. Liu, X. Chen, Y. Wang and W. Yang, *Macromolecules*, 2006, **39**, 3224-3230.
276. C. Zhao, C. Wang, Z. Yue, K. Shu and G. G. Wallace, *ACS applied materials & interfaces*, 2013, **5**, 9008-9014.
277. Z. Ni, H. Wang, J. Kasim, H. Fan, T. Yu, Y. Wu, Y. Feng and Z. Shen, *Nano Letters*, 2007, **7**, 2758-2763.
278. K. S. Kim, Y. Zhao, H. Jang, S. Y. Lee, J. M. Kim, K. S. Kim, J.-H. Ahn, P. Kim, J.-Y. Choi and B. H. Hong, *Nature*, 2009, **457**, 706-710.
279. C. Gómez-Navarro, R. T. Weitz, A. M. Bittner, M. Scolari, A. Mews, M. Burghard and K. Kern, *Nano Letters*, 2007, **7**, 3499-3503.
280. D. Yang, A. Velamakanni, G. Bozoklu, S. Park, M. Stoller, R. D. Piner, S. Stankovich, I. Jung, D. A. Field and C. A. Ventrice Jr, *Carbon*, 2009, **47**, 145-152.
281. S. Bose, T. Kuila, M. E. Uddin, N. H. Kim, A. K. Lau and J. H. Lee, *Polymer*, 2010, **51**, 5921-5928.
282. A. Ferrari, J. Meyer, V. Scardaci, C. Casiraghi, M. Lazzeri, F. Mauri, S. Piscanec, D. Jiang, K. Novoselov and S. Roth, *Physical review letters*, 2006, **97**, 187401.
283. K. N. Kudin, B. Ozbas, H. C. Schniepp, R. K. Prud'Homme, I. A. Aksay and R. Car, *Nano Letters*, 2008, **8**, 36-41.
284. L. Malard, M. Pimenta, G. Dresselhaus and M. Dresselhaus, *Physics Reports*, 2009, **473**, 51-87.
285. V. Subramanian, H. Zhu and B. Wei, *Electrochemistry Communications*, 2006, **8**, 827-832.
286. S. Biswas and L. T. Drzal, *Chemistry of Materials*, 2010, **22**, 5667-5671.